

Inverse Design of Metamaterials via Topology Optimization

Von der Fakultät für Mathematik und Physik
der Gottfried Wilhelm Leibniz Universität Hannover

zur Erlangung des akademischen Grades
Doktor der Naturwissenschaften
Dr. rer. nat.

genehmigte Dissertation von

M. Sc. Chuong Thanh Nguyen

2022

Referentin: Prof. Dr. Xiaoying Zhuang
Leibniz Universität Hannover

Korreferenten: Prof. Dr. Ludovic Chamoin
Université Paris-Saclay

Prof. Dr. Peter Wriggers
Leibniz Universität Hannover

Vorsitz der Promotionskommission: Prof. Dr. Thomas Wick
Leibniz Universität Hannover

Tag der Disputation: 20.06.2022

Zusammenfassung

Metamaterialien sind künstliche Verbundwerkstoffe mit Mikrostrukturen, die systematisch so gestaltet sind, dass das makroskopische Verhalten besondere Funktionen oder außergewöhnliche Eigenschaften aufweist, die in natürlichen Materialien nicht üblich sind. Topologie und Geometrie der Mikrostrukturen spielen eine wichtige Rolle bei der Charakterisierung der Eigenschaften der Metamaterialien. Das inverse Design von Metamaterialien mittels Topologie-Optimierungsmethoden bietet neue topologische Eigenschaften und hilft bei der Erreichung neuartiger physikalischer Mechanismen oder Hochleistungsfunktionen.

Inverses Design ist ein iterativer Prozess, der numerische Analysen beinhaltet und viel Rechenleistung erfordert. In dieser Dissertation wird eine Methodik für den Entwurf von Metamaterialien unter Verwendung von Topologieoptimierung mit Level-Set-Funktionen und Methoden zur Reduzierung der Modellordnung vorgeschlagen. Die Level-Set-Methode ermöglicht ein Design mit glatten Grenzen, während der Rechenaufwand, der für die Lösung großer linearer Gleichungssysteme erforderlich ist, durch reduzierte Basisapproximationen entfällt. Ein Beispiel für die inverse Entwurfsmethode aus der Dissertation ist die Suche nach einer Einheitszellenstruktur, die zu makroskopischen Eigenschaften mit beabsichtigtem Elastizitätsmodul führt, beispielsweise mit negativer Poissonzahl. Ein anderes Beispiel ist die Verbesserung der Leistung von Hydrophonen in 1-3 piezoelektrischen Verbundwerkstoffen. Numerische Beispiele zeigen, dass die Methodik für die Entwicklung von Metamaterialien rechnerisch effizient und robust ist.

Die Vorteile des inversen Designs als leistungsfähiges Werkzeug bei der Entwicklung von Metamaterialien werden in dieser Dissertation für die Entwicklung von Wellenleitern genutzt. Der zweite Teil dieser Arbeit zielt darauf ab, phononische Kristalle zu entwerfen, die einen robusten Transport von mechanischen Wellen an den Grenzflächen ermöglichen. Die sich ausbreitenden Wellenmoden in plattenförmigen Strukturen sind topologisch geschützte Randzustände und entsprechen dem Quanten-Tal-Hall-Effekt und dem Quanten-Spin-Hall-Effekt in elektronischen Systemen. Die angewandte rechnerische inverse Entwurfsmethodik besteht in der Topologieoptimierung mit Hilfe eines genetischen Algorithmus, um optimierte Einheitszellengeometrien zu finden, die sich aus Zielfunktionen auf der Grundlage von Bandstrukturen und Wellenmoden ergeben. Die optimierten phononischen Kristalle unterstützen die Wellenausbreitung trotz des Vorhandenseins von Defekten gegen Rückstreuung.

Schlagworte: Metamaterialien, Topologieoptimierung, Modellordnungsreduktion, phononische Kristalle, topologisch geschützte Kantenmoden

Abstract

Metamaterials are artificial composites with micro-structures that are systematically designed such that the macroscopic behavior can accommodate particular functionalities or exhibit extraordinary properties, which are not commonly found in natural materials. Topology and geometry of micro-structures play an important role in characterizing the properties of the metamaterials. Inverse design of metamaterials via topology optimization methods offer new topological features and helps in achieving novel physical mechanism or high-performance functionalities.

Inverse design is an iterative process, that involves numerical analysis and requires much computational resources. This dissertation proposes the methodology for designing metamaterials using topology optimization with level set functions and model order reduction methods. Level set method enables design with smooth boundaries, while the computational effort required in solving large linear system of equations is eliminated with reduced basis approximations. An example of the inverse design method from the dissertation is to find a unit cell structure that results in macroscopic properties with intended elastic modulus for instance, with negative Poisson's ratio. The other example is to enhance hydrophone performance in 1-3 piezoelectric composites. Numerical examples demonstrate that the methodology is computationally efficient and robust for designing metamaterials.

Taking advantage of inverse design as a powerful tool in designing metamaterials, it is adopted in this dissertation for the waveguides design. The second part of this thesis aims to design phononic crystals that offer robust transport of mechanical waves on the interfaces. The propagating wave modes in plate-like structures are topologically protected edge states and are analogous to quantum valley hall effect and quantum spin hall effect in the electronic systems. The computational inverse design methodology adopted is through topology optimization using genetic algorithm to find optimized unit cell geometries resulting from objective functions based on band structures and wave modes. The optimized phononic crystals support wave propagation against backscattering inspite of the presence of defects.

Keywords: Metamaterials, topology optimization, model order reduction, phononic crystals, topologically protected edge modes

Acknowledgements

This dissertation is the result of my research work during the past six years at the Leibniz Universität Hannover under the guidance of Prof. Xiaoying Zhuang. The project was supported by the ERC project (802205). I would like to express my sincere gratitude to my advisor, Prof. Xiaoying Zhuang, for giving me the opportunity to study in Germany, for her professional suggestions on my project. My deep thanks go to Prof. Ludovic Chamoin, for his valuable guidance throughout my studies. He provided me with the tools that I needed to choose the right direction and successfully complete my dissertation. I am also grateful to Prof. Hung Nguyen-Xuan, he provided me knowledge of computational mechanics during my master courses and PhD period. I would like to acknowledge my colleagues: Dr. Nanthakumar Srivilliputtur Subbiah for helpful discussion in research work. I thank to Ms. Bettina Dischinger for handling the documents and all background works in preparing the promotion. I also thank to Ms. Dorit Schulte, supported me much in life aspects at the time I arrived in Germany. Last but not least, my office mates, Dr.-Ing. Philipp Hartmann and Dr.-Ing. Dengpeng Huang for the strong support and the pleasant working atmosphere in our office. My important, I am grateful to my parents for their constant support all the time.

Chapter 2 is a reprint of the content published in: *C. Nguyen, X. Zhuang, L. Chamoin, X. Zhao, H. Nguyen-Xuan, and T. Rabczuk, "Three-dimensional topology optimization of auxetic metamaterial using isogeometric analysis and model order reduction," Comput. Methods Appl. Mech. Eng., vol. 371, p. 113306, 2020, doi: <https://doi.org/10.1016/j.cma.2020.113306>.*

Chapter 3 is a reprint of the content published in: *C. Nguyen, X. Zhuang, and L. Chamoin, "Topology Optimization of 1-3 Piezoelectric Composites," in Lecture Notes in Applied and Computational Mechanics, vol. 93, P. Wriggers, O. Allix, and C. Weißenfels, Eds. Cham: Springer International Publishing, 2020, pp. 185–198, doi: https://doi.org/10.1007/978-3-030-38156-1_10.*

Chapter 5 is a reprint of the content published in: *X. Zhuang, C. Nguyen, S. S. Nanthakumar, L. Chamoin, Y. Jin, and T. Rabczuk, "Inverse design of reconfigurable piezoelectric topological phononic plates," Mater. Des., p. 110760, 2022, doi: <https://doi.org/10.1016/j.matdes.2022.110760>.*

Hannover, 20.06.2022

Chuong T. Nguyen

Contents

Nomenclature	v
List of Figures	x
List of Tables	1
1 Introduction	3
1.1 Elastic Metamaterials	3
1.2 Analysis Methods of Metamaterials	4
1.3 Selected Problems for Inverse Design of Metamaterials	5
1.4 Summary of Chapters and Contributions	6
2 Three-dimensional Topology Optimization of Auxetic Metamaterial Using Isogeometric Analysis and Model Order Reduction	9
2.1 Introduction	9
2.2 Homogenization Method	11
2.3 Level Set Function	12
2.4 Isogeometric Analysis with Bézier Extraction	14
2.5 Reduced Order Modelling	16
2.6 Sensitivity Analysis	18
2.7 Objective Function of Topology Optimization for Metamaterials	20
2.8 Numerical Examples	21
2.9 Discussion and Conclusion	28
3 Topology Optimization of 1-3 Piezoelectric Composites	31
3.1 Introduction	31
3.2 Constitutive Relation of The 1-3 Piezocomposite	33
3.3 Materials Microstructure Topology Optimization by The Level Set Method	34
3.4 Optimization Algorithm	38
3.5 Results	39
3.6 Conclusion	42
4 Inverse Design of Topological Phononic Plates	43
4.1 Introduction	43
4.2 Lattice Symmetry, Brillouin Zones and Band Structures	45
4.3 Topological Phononics	49
4.3.1 Adiabatic evolution	50
4.3.2 Berry phase and Chern number	51

4.4	Designing C^6 Unit Cell Exhibiting Dipole (p_x, p_y) and Quadrupole ($d_{x^2-y^2}, d_{xy}$) Modes	52
4.4.1	I. Dispersion equation approach	53
4.4.2	II. Equilibrium equations approach	54
4.4.3	Fine tuning the topologies based on Supercell band structure	56
4.5	Numerical Results	57
4.5.1	Elastic Pseudospin Wave Propagation at TI Interface	59
4.5.2	Waveguide to circumvent damages	62
4.6	Discussion	63
	Appendix 4.A Genetic Algorithm Based Topology Optimization method	64
5	Inverse Design of Reconfigurable Piezoelectric Topological Phononic Plates	67
5.1	Introduction	67
5.2	Inverse Design Methodology	68
5.2.1	The first objective function: Forming two-fold degeneracy in piezoelectric phononic plates	69
5.2.2	The second objective function: Maximize the topological band gap by breaking inversion-symmetry	70
5.3	Inverse Design Example	71
5.4	Topological Edge States in Piezoelectric Phononic Plates	73
5.5	Conclusions	76
	Appendix 5.A Finite Element Method for Piezoelectric plates	77
	Appendix 5.B Berry Curvature and Chern Number	81
	Appendix 5.C Parameter Setting for The Genetic Algorithm	82
6	Discussion and Outlook	85
	Bibliography	85
	Curriculum Vitae	96

Nomenclature

Scalars

ϕ	Level set function value
V_n	Normal velocity component
ρ	Density
t, τ	Time
ξ, ϵ	Positive small number
v_f	Volume fraction
ν	Poisson's ratio
κ	Bulk modulus
μ	Shear modulus
d_h	Effective hydrostatic charge coefficient
ω	Frequency
k	Wave number
Ψ	Solutions of Schrödinger equation
B	Berry curvature
C	Chern number

Vectors

- \mathbf{x}, \mathbf{y} Position
- \mathbf{u} Displacement
- \mathbf{k} Wave vector
- \mathbf{a} Primitive vectors of lattice in the real space
- \mathbf{b} Primitive vectors of lattice in the reciprocal space
- \mathbf{P} Poynting vector
- χ Characteristic displacement
- $\bar{\mathbf{t}}$ Traction
- α Design variable
- \mathbf{E} Electric field
- \mathbf{D} Electric displacement

Second order tensors

- σ Cauchy stress tensor
- ε Strain tensor
- \mathbf{C} Elastic modulus tensor
- \mathbf{e} Piezoelectric coupling tensor
- ϵ Permittivity tensor
- \mathbf{A} Berry connection

Mathematical operators

- \mathcal{H} Heaviside function
- δ Dirac delta function
- ∇ Divergence
- $(\dot{\circ})$ First order time derivative
- $(\ddot{\circ})$ Second order time derivative

Abbreviations

- H-J Hamilton-Jacobi
- CFL Courant-Friedrichs-Lewy condition
- PLSM Parameterized level set method
- IGA Isogeometric analysis
- NURBS Nonuniform rational basis function
- PCs Phononic crystals
- QSHE Quantum Spin Hall effect
- QHE Quantum Hall effect
- QVHE Quantum valey Hall effect

List of Figures

1.1	Metamaterial structure composed from hexagonal unit cells and its primitive vectors.	3
1.2	Operating wavelengths and corresponding homogenization methods in metamaterials. Adapted from [1].	4
2.1	Unit cell geometry represented by a level set function (a) and fixed mesh on a square domain (b).	13
2.2	B-spline basis functions (left) and their corresponding Bernstein-Bézier representation (right).	15
2.3	Microstructure topology optimization algorithm with and without reduced basis model.	17
2.4	Influence of initial configurations and volume fraction to final designs.	23
2.5	Convergence of the objective function.	24
2.6	Convergence of the objective function by using the algorithm with reduced order model in Fig. 2.3 (right). Blue squares indicate the reduced solutions are used.	25
2.7	Influence of initial configurations and volume fractions to final designs in three-dimensional metamaterials design.	27
2.8	Convergence of the objective function (of the unit cell in Fig. 2.7b) by using the algorithm with reduced order modeling. Blue squares indicate the reduced solutions are used.	28
3.1	Class of the 1-3 piezoelectric composite.	32
3.2	Level set function.	35
3.3	Effective hydrostatic charge coefficient of the 1-3 piezocomposite (a). Enhancement of d_h due to Poisson's ratio (b).	40
3.4	Effective hydrostatic charge and electrical voltage coefficients of the 1-3 piezocomposite. Top and bottom with the designs (a) and (b) in Table 3.2, respectively.	42
4.1	Illustration of spin dependent edge states in a quantum spin Hall system.	44
4.2	Hexagonal primitive unit cell (a) and its Brillouin zone (b). Examples of unit cell with C_{6v} -symmetry (c) and C_6 -rotational symmetry (d).	47
4.3	Periodic of momentum vectors in two-dimensional lattice.	52
4.4	Illustration of target band structure for (a) Topology A, (b) Topology B. (c) Nature of dipole (p_x, p_y) and quadrupole ($d_{x^2-y^2}, d_{xy}$) modes.	53
4.5	Force profiles.	56
4.6	Optimization problem on supercell. Illustration of edge bands intersecting at Γ point (left). Schematic of the interface comprising unit cell A and B (right).	57

4.7	(a) Optimized unit cell topology A_I . (b) Band structure without mode separation. (c) Inset from (b), where red solid lines denote asymmetric modes and black dashed lines denote symmetric modes. (d) Deformation modes p and d at two-fold degenerate points, the color indicates magnitude of u_z displacement component.	58
4.8	(a) Optimized unit cell topology B_I . (b) Band structure without mode separation. (c) Inset from (b), where red solid lines denote asymmetric modes and black dashed lines denote symmetric modes. (d) Deformation modes p and d at two-fold degeneracy points, the color indicates magnitude of u_z displacement component.	58
4.9	(a) Optimized unit cell type A_{II} . (b) Band structure without mode separation. (c) Inset from (b), where red solid lines denote asymmetric modes and black dashed lines denote symmetric modes. (d) Deformation modes p and d at two-fold degeneracy points, the colors indicate magnitude of u_z displacement component.	59
4.10	(a) Optimized unit cell type B_{II} . (b) Band structure without mode separation. (c) Inset from (b), where red solid lines denote asymmetric modes and black dashed lines denote symmetric modes. (d) Deformation modes p and d at twofold degeneracy points, the color indicate magnitude of u_z displacement component.	59
4.11	Band structure of supercell constructed from two unit cells A_I and B_I (left). Plot of eigenmodes at the points S1 & S2 in the band structure (right). . . .	60
4.12	Elastic wave propagating in full plate model with plus interface constructed from two unit cell A_I and B_I	61
4.13	Band structures of supercell constructed from two unit cells A_{II} and B_{II} (left). Plot of eigenmodes at the points S1 & S2 in the band structure (right). . . .	61
4.14	Elastic wave propagating in full plate model with plus interface constructed from two unit cell A_{II} and B_{II}	62
4.15	(a) and (b) Damaged domain with and without designed periodic phononic plate respectively. Top row: magnitude displacement plot. Bottom row: von Mises stress. Frequency domain simulation at $f = 57.5$ kHz. (c) Geometry of the elliptical void.	63
4.A.1	The crude initial topology from the randomly generated binary string is refined to obtain a meaningful topology.	64
4.A.2	Mapping square topologies onto quadrilateral building blocks of C_{6v} symmetry hexagonal unit cell.	64
1	(a) First Brillouin zone in the reciprocal space of parallelogram. (b) Randomly generated binary string is rearranged and improved by Morphological Image Processing (MIP) to obtain a well connected unit cell topology.	69
2	(a-c) Phononic composite plates comprising a piezoelectric patch (blue) attached to a substrate plate (green). Two electrodes (red and magenta denoting ON and OFF state, respectively) are connected to the upper surface of the piezoelectric patch. (d-f) Band structures of the optimized unit cell, when the two switches are open (open-circuit condition, a) and one of the switches is closed (shunted-circuit condition, e & f) and the other is open.	72
3	Eigenmodes of unit cells A and B at the K -point.	72

4	Mechanical energy flux at the K -point represented by Poynting vectors. Red and magenta arrow indicate vortex patterns of the energy flux.	73
5	(a) Schematic and band structure of the supercell. (b) Selected eigenmodes at blue and green points show that the deformation is antisymmetric at DW1 and symmetric at DW2. Colorbar indicates the magnitude of out-of-plane displacement.	74
6	Illustration of the conversion of incident wave p_i to Bloch wave p_t in the phononic plate. Converted Bloch wave is antisymmetric with respect to the interface DW1.	74
7	Wave propagation due to the topological edge state. Schematic of the Z -interface and magnitude of displacement showing elastic flexural wave propagation along DW1 (bottom) and DW2 (top) for two different sources $\{s^0, s^{-a}\}$ and $\{s^0, s^{+a}\}$	76
8	Simulation of transient wave propagating along Z -interface with and without defects. Snapshots of the displacement magnitude at $t = 0.0049$ s and $t = 0.010$ s.	76
5.B.1	Berry curvature over the first Brillouin zone.	82
5.C.1	Pareto front of two normalized objective functions J_1^{OC} and J_2^{ZC} at the 89 th generation.	83

List of Tables

2.1	Computation time of the 3D examples with and without using reduced order modelling.	28
3.1	Material parameters.	40
3.2	Designs of microstructures of the polymer matrix.	41
1	Material properties of substrate (aluminum) and piezoelectric patch (PZT-5A).	71

Chapter 1

Introduction

1.1 Elastic Metamaterials

Metamaterials are artificial composites exhibiting extraordinary mechanical behaviors that cannot be found in nature. The structure made of metamaterials is constructed by arranging unit cells in a periodic or non-periodic manner, while the unit cell may constitute one or multiple materials. [Figure 1.1](#) shows an example of a two-dimensional periodic structure, in which the unit cells are identical hexagons and the position of a primitive cell is described by:

$$\mathbf{r} = n_1 \mathbf{a}_1 + n_2 \mathbf{a}_2 + n_3 \mathbf{a}_3, \quad n_i \in \mathbb{Z}, \quad (1.1)$$

where \mathbf{a}_i are primitive vectors. An infinite number of unit cells extending in the spatial dimensions and macroscopic behavior of the metamaterials are comprehensively understood by studying the unit cell alone under periodic conditions. This assumption is reasonable if operating wavelengths are much smaller than the macroscopic length L_0 . The metamaterials

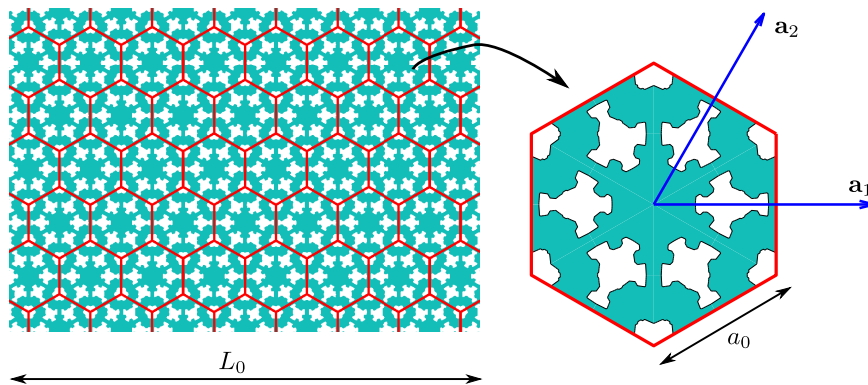


Figure 1.1: Metamaterial structure composed from hexagonal unit cells and its primitive vectors.

are rationally designed such that its effective properties can be better or special than those of the constituent materials of the unit cell. For example, negative thermal expansion, or negative Poisson's ratio from materials have positive properties can be achieved. In waveguide applications, negative refraction of elastic waves can be achieved by appropriately designing unit cells with negative effective modulus and mass. The metamaterials offer exciting possibilities and warrants new studies on means to fabricate such complex 3D

geometries, advancements in numerical methods to handle complex topologies for solving forward problems, progress in modelling and computer-aided design.

Practical applications seek metamaterials with exceptional material properties that can improve performance of the related devices. The major step in research on metamaterials is to inverse design such artificial composites through shape and topology optimization methods.

1.2 Analysis Methods of Metamaterials

Solving boundary value problems in heterogeneous domains generally require large computational resources, while in case of periodic structures the behaviour of the finite structure can be understood by studying the unit cells. Analysing the unit cell, behavior of the periodic structure can be predicted from the effective parameters or dispersion relations.

The static or dynamic properties of metamaterials need to be determined depending on the operating wavelengths of the incoming elastic wave. Figure 1.2 shows three groups of wavelengths (λ) and indicates homogenization methods to determine effective medium parameters. In the region (A), where wavelengths are sufficiently large compared to the

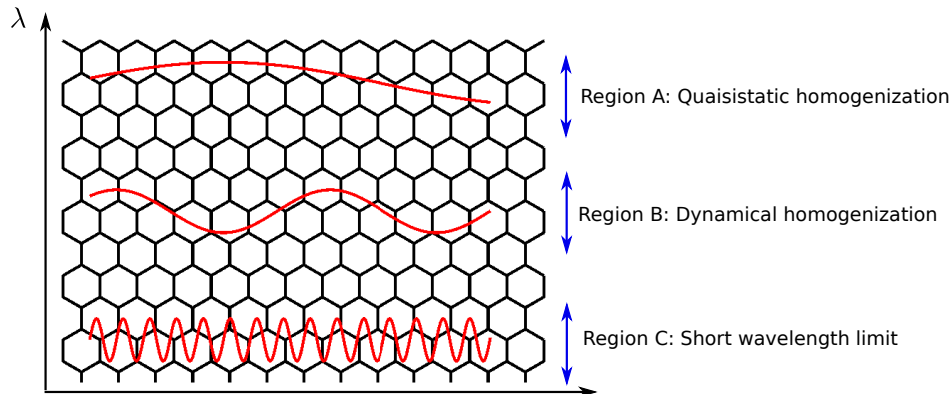


Figure 1.2: Operating wavelengths and corresponding homogenization methods in metamaterials. Adapted from [1].

lattice constant a_0 , i.e., low-frequency regime (due to $f \propto \lambda^{-1}$), the dispersion effect is trivial. Homogenization approaches, mathematically developed by Bensoussan et al. [2] and Sánchez-Palencia [3], are able to determine the effective coefficients. For example, density $\rho^{\text{eff}}(\mathbf{x})$ and modulus tensor $\mathbb{C}^{\text{eff}}(\mathbf{x})$ of elastic metamaterials are frequency-independent in this regime.

In case of wavelengths comparable to lattice constant (region B), homogenization must consider dispersion of wave propagation. Indeed, periodic metamaterials are still homogenized by effective medium theory, but the macroscopic parameters are frequency-dependent. In these operating wavelengths, intriguing phenomena in wave mechanics such as negative dispersion band or negative refraction are observed due to the occurrence of resonances in the unit cells. This local resonances result in negative effective density and elastic moduli within a certain frequency range. Thereby offering interesting applications such as elastic superlensing, wave imaging and wave confinement.

In the region (C), wavelengths are on the same order or even smaller than the lattice length and wave propagating in phononic metamaterials dominantly undergo scattering by heterogeneity, reflecting and refracting at the material interfaces. Homogenization theory could not determine effective medium parameters in this short wavelength (high-frequency) limit. Wave behaviors in phononic crystals is succinctly represented by the band structure. Internal interface boundaries can reflect waves causing destructive or constructive interference, which prohibit or allow wave propagation in space. The destructive interference can lead to occurrence of gaps in the band structure. Manipulating the band structure of unit cells indeed can control wave propagation characteristics.

1.3 Selected Problems for Inverse Design of Metamaterials

Since the physical properties of metamaterials rely on microstructures, searching for new functional materials turn out to inversely designing topology of unit cells such that they exhibit desirable band structures. In contrast to empirical design methods, inverse design via topology optimization, that use mathematical optimization schemes to obtain the best design, can freely provide new topological features due to lesser constraints on the number of geometric parameters.

In the work by Bendsøe and Sigmund [4], topology optimization was employed to design structures with high-performance functionalities under material volume constraint and the approach is extended to all engineering fields. Design variables are local density of the finite elements in the modelled structure and it ranges from 0 to 1 to represent void and solid materials. The smoothness of material boundaries are dependent on mesh density, hence, influence the accuracy of numerical solutions.

Alternatively, the level set method [5, 6] provides a flexible approach in representing geometries without external geometric parameterization and performing numerical simulation with a fixed mesh. The level-set method allows change in shape or topology of the unit cell simultaneously and results in diverse topological features in the designed unit cell structure. Structural optimization via a level set method was later proposed by Allaire et al. [7], in which design variables are the level set functions. The work have illustrated the ability of the method in designing complex structures and obtaining smooth boundaries in the structure. The additive manufacturing of metamaterials to fabricate prototypes require description of smooth structure boundaries to improve the quality of fabrications. Therefore, inverse design methods using level set functions for geometry description are preferable due to its possibility ease in production.

In this research, we aim to use the level set approach for topology optimization of microstructures possessing negative Poisson's ratio (NPR) i.e. auxetic effect. Typically the class of auxetic metamaterials have shown potential applications from biomedical to defense problems [8, 9]. Modifying the effective Poisson's ratio, which affects kinematic deformations, can enhance the performance of embedded structures. The polymer matrix that possesses negative Poisson's ratio enhances hydrostatic parameters of the 1-3 piezoelectric composites [10].

In waveguide applications, topological phononic crystals exhibit unique protection from not only backscattering, but also to structural defects like cavities, disorder and sharp bends.

The stable surface or boundary modes of mechanical waves in phononic topological insulators (TIs) are analogous to electronic TIs, which are electrically insulating in its interior, but their surface is conductive [11–13]. The TI phenomenon is used in various applications such as vibration isolation and wave guiding. Researchers have developed several mechanical analogies to the topological quantum systems, for example, the works by Süsstrunk and Huber [14], Nash et al. [15] and [16] have provided basic requirements to be satisfied by phononic metamaterials to host topological surface waves. In line with these works, we propose inverse design approach by topology optimization to obtain phononic metamaterials that exhibit topologically protected states of elastic waves.

1.4 Summary of Chapters and Contributions

In [Chapter 2](#), we present an approach for designing material micro-structures by using isogeometric analysis and parameterized level set method. Design variables, which are level set values associated with control points, are updated from the optimizer and represent the geometry of the unit cell. The computational efficiency is further improved in each iteration by employing reduced order modeling when solving linear systems of the equilibrium equations. We construct a reduced basis by reusing computed solutions from previous optimization steps, and a much smaller linear system of equations is solved on the reduced basis. Two- and three-dimensional numerical results show the effectiveness of the topology optimization algorithm coupled with the reduced basis approach in designing metamaterials.

In [Chapter 3](#), optimal hydrophone performance for 1-3 piezoelectric composites is achieved from the design of material properties. The piezocomposite consists of piezoceramic rods immersed in a polymer matrix. We obtain the effective moduli of the piezocomposite by the differential effective medium theory and the results are explicitly dependent on volume fractions of the piezoceramic rods and elastic properties of the matrix. Topology optimization with level set method is used to optimize the elastic properties of the matrix phase. Numerical examples propose three-dimensional microstructures with negative Poisson's ratio for the polymer matrix that can enhance hydrostatic charge coefficients of the piezocomposite.

In [Chapter 4](#), we focus on inverse design of flexural phononic plate TIs with C^6 symmetry. We utilise two different inverse design approaches, one of them based on solving the dispersion equation and the other on solving elastic equilibrium equation for the hexagonal unit cell. The analogue designed is based on Quantum Spin Hall effect (QSHE) and the success of the design procedures adopted lie in the realisation of spin dependent propagation in a periodic structure. The numerical examples presented show the designed plate unit cell topologies and the one way topologically protected interface propagation along a plus interface proving that the proposed inverse design methods are promising.

In [Chapter 5](#), we present a methodology to perform inverse design of reconfigurable topological insulators for flexural waves in plate-like structures. A genetic algorithm based topology optimization method is developed and a C^{6v} plate unit cell topology that offers two-fold degeneracy in the band structure is designed. Piezoelectric patches, that are connected to an external circuit, are bonded to the substrate plate and are altered appropriately to break space inversion symmetry. The space inversion symmetry breaking opens a topological band gap mimicking quantum valley Hall effect. Numerical simulations demonstrate that the

topologically protected edge state exhibits wave propagation without backscattering and is immune to disorders. The present work achieves real-time reconfigurability of the topological interfaces for waveguide applications.

Finally, [Chapter 6](#) briefly discusses about existing problems that need to be addressed and explores directions for future works.

Chapter 2

Three-dimensional Topology Optimization of Auxetic Metamaterial Using Isogeometric Analysis and Model Order Reduction

2.1 Introduction

Metamaterials are classified as artificial composites possessing extraordinary mechanical behaviors that are not available in nature. They have received attention in scientific applications and engineering over the last decades. Typically the class of auxetic metamaterials having properties of negative Poisson's ratio (NPR) have shown potential applications from biomedical to defense problems [8, 9]. Modifying the effective Poisson's ratio, which affects kinematic deformations, can enhance the performance of embedded structures. The material functionalities are attained by rationally designing their microstructure layouts. Among material design methods, shape and topology optimization for primitive cells has been considered as a prominent method for materials functionality design.

Topology optimization generally involves iterative searching for material distribution within design domains. In the density-based topology optimization, the void and solid regions of material are represented by density values, which are also considered as design variables. Among the density approaches, the evolutionary structural optimization (ESO) [17, 18] and solid isotropic material with penalization (SIMP) method [19] are frequently used in structural and material optimization [20, 21] due to their efficiency and easy implementation. Alternatively, the level set method represents structural boundaries by a zero level set function, which enables flexible changes in shape and topology with distinct material interfaces. Various optimization problems have been successfully implemented with the level set approach, e.g., structure compliance minimization [7, 22], frequency response problem [23], or design of metamaterials with negative Poisson's ratio [24, 25].

In microstructure topology optimization, the effective properties of unit cells are determined

by a numerical homogenization procedure. This involves solving linear systems of equilibrium equations and requires high computational cost. In order to circumvent this issue, reduced order modeling using Krylov subspaces [26, 27] has been proposed to enhance the efficiency. Large linear systems are solved by an iterative solver and using a search space from the previous linear system. The approach assumes that numerical stiffnesses from two consecutive iterations are slightly different due to minor changes in shapes or topology of structures. Alternatively, the reduced-basis approaches approximate high-dimensional solutions by the projection of the original model into a lower-dimensional subspace which is spanned by global basis functions or truncated modes. This surrogate model was employed in nonlinear structural optimization [28], or multiscale homogenization [29]. Similarly, Gogu [30] proposed a reduced basis constructed from displacements which are calculated from a set of similar configurations. The original linear system is then projected on the reduced basis with a smaller size. The method has shown much improvement in structural topology optimization.

The motivation for using isogeometric analysis [31, 32] so far is due to higher-order approximation with the B-Spline or NURBS basis functions which are compatible with CAD tools. It enables to model the geometry in computer-aided design exactly, and the basis functions used to represent the geometry can directly approximate solution fields in numerical computation. Recently, this framework has also been used in various optimization problems, i.e., by Wang and Benson [33] with level set functions, Costa et al. [34] using the SIMP approach in structural optimization and Gao et al. [35] for auxetic metamaterials. Several works [36, 37] introduced IGA coupled with reduced order models (ROM) to alleviate the computational cost for parameterized geometry model, and have shown an improvement in both accuracy and efficiency compared to the finite element method. We also mention the shape optimization problems in which the geometry parameters assigned as design variables are efficiently optimized with the combination of reduced order approaches. For example in Ammar et al. [38], the proper generalized decomposition (PGD) was introduced to compute in an offline phase the parametric solutions for selected parameters which involve the sensitivity information provided. A similar strategy for parameter optimization may be applied with the isogeometric framework, such as in Chamoin and Thai [39], where model reduction based on PGD provides parametric solutions with much lower computation cost.

In this work, we exploit advantages of the parameterized level set method using the isogeometric setting for metamaterials design. This approach possibly allows using basis functions with higher orders to approximate the displacement field and the level set function. We further integrate reduced order modeling to improve the efficiency of the topology optimization algorithm. The proper coupling of reduced order techniques in an isogeometric framework is attractive and feasible due to the fact that the reduced basis is constructed from a smoother manifold of the isogeometric solution, and the optimized geometry is subsequently generated from the reduced solutions with saving computational time. We provide sensitivity analysis involving the reduced solutions in the level set framework. Metamaterial structures are designed in two and three dimensions to show the efficiency and reliability of the approach.

The paper is organized as follows: in Section 2.2, we briefly discuss numerical homogenization methods and formulation for the effective elasticity tensor. Section 2.3 introduces the parameterized version of the level set function. In Section 2.4, the discretized formulation with the isogeometric analysis using Bézier extraction for the numerical analysis is given.

Afterward, the construction of the reduced basis is reviewed in [Section 2.5](#), and in [Section 2.6](#) the sensitivity analysis involving reduced solutions of effective coefficients is described. A general setting for design of metamaterials is introduced in [Section 2.7](#). Numerical examples are presented in [Section 2.8](#) and followed by the conclusion in [Section 2.9](#).

2.2 Homogenization Method

Heterogeneity of composite materials by nature requires fine scale discretization to capture the geometric details; this leads to large finite element models and increased computational burden. An alternative material modeling is to replace heterogeneity with an effective homogeneous model by considering a representative volume that can describe the equivalent properties at the macroscopic scale. The classical approach is based on the assumption of periodic arrangement of the micro-structures, and it also considers that the length scale of the periodic structures is small when compared to dimensions of the macroscopic structure. The study of macroscopic properties is conventionally replaced by considering a single unit cell alone.

Several analytical approaches are available to evaluate the effective properties of composites. For example, considering the volume fraction of a single inclusion embedded into an infinite matrix material, the effective properties were derived by Eshelby and Peierls [40]. Further developments from this approach and widely employed in modeling homogenized material can be found in the work by Mori and Tanaka [41], or self-consistent scheme by Hill [42]. These analysis methods mainly deal with simple geometries of inclusions, i.e., circles or ellipses. In the context of topology optimization, complex geometries of the unit cell frequently occur and the analytical models are not able to predict effective properties of composites.

Numerical approaches have been developed to address the problem. From macroscopic strains, stresses and strain energy density, the effective elasticity of inhomogeneous materials was derived using a direct average method [43–45]. Similarly, Zhang et al. [46] used the strain energy-based methods to predict effective properties in microstructure topology optimization. The work of Guedes and Kikuchi [47], or Sanchez-Palencia [45] introduced a rigorous mathematical theory for deriving effective elasticity coefficients by using weak-form of equilibrium equation and limits theory, namely asymptotic homogenization method. Another mathematical derivation for homogenized elasticity which is based on the governing equations with strong formulation can be found in the work by Zhuang et al. [48], and a similar framework for multi-field problems was recently investigated by Fantoni et al. [49].

The design of metamaterials in this work relies on the asymptotic homogenization method. Effective properties across a unit cell are obtained from a homogenization procedure with assumptions of periodicity and scale separation over the unit cell with overall macroscopic dimensions. A brief explanation of the asymptotic homogenization method used in this paper is given in the following and details of derivation can be found in Guedes and Kikuchi [47], Hassani and Hinton [50].

Due to local changes of material properties, the displacement expression is dependent on the

small parameter ϵ and written as an asymptotic expansion:

$$\mathbf{u}^\epsilon(\mathbf{x}, \mathbf{y}, \epsilon) = \mathbf{u}^0(\mathbf{x}) + \epsilon \mathbf{u}^1(\mathbf{x}, \mathbf{y}) + \epsilon^2 \mathbf{u}^2(\mathbf{x}, \mathbf{y}) + \dots \quad \text{with} \quad \mathbf{y} = \mathbf{x}/\epsilon, \quad (2.1)$$

\mathbf{x} and \mathbf{y} are macroscopic and microscopic (unit cell) coordinates respectively. The displacement \mathbf{u}^ϵ of the composite body is solution to the variational problem

$$\int_{\Omega} \boldsymbol{\varepsilon}(\mathbf{u}^\epsilon) : \mathbb{C} : \boldsymbol{\varepsilon}(\mathbf{v}) \, d\Omega = \int_{\Omega} \mathbf{b} \cdot \mathbf{v} \, d\Omega + \int_{\Gamma} \tilde{\mathbf{t}} \cdot \mathbf{v} \, d\Gamma, \quad (2.2)$$

where \mathbf{v} is the test function and $\boldsymbol{\varepsilon}$ is the mechanical strain. Body forces \mathbf{b} and surface tractions $\tilde{\mathbf{t}}$ are assumed not to vary over the microscopic domain. In the following procedure only the first and second variation terms of the displacement expansion (2.1) are employed to derive the effective elasticity tensor, and due to the linearity of the problem the second term can be written as

$$\mathbf{u}^1(\mathbf{x}, \mathbf{y}) = \boldsymbol{\chi}(\mathbf{x}, \mathbf{y}) \boldsymbol{\varepsilon}(\mathbf{u}^0(\mathbf{x})), \quad (2.3)$$

where $\boldsymbol{\chi}(\mathbf{x}, \mathbf{y})$ is the characteristic displacement. By substituting the asymptotic expansion (2.1) into (2.2) and applying the asymptotic analysis of the periodic functions in a unit cell [47], the following equilibrium equation is obtained

$$\int_Y \varepsilon_{pq}(\boldsymbol{\chi}^{ij}) C_{pqrs}(\mathbf{y}) \varepsilon_{rs}(\mathbf{v}) \, dY = \int_Y \varepsilon_{pq}^{0,ij} C_{pqrs}(\mathbf{y}) \varepsilon_{rs}(\mathbf{v}) \, dY \quad \forall \mathbf{v} \in V_0 \subset H^1, \quad (2.4)$$

where $\varepsilon^{0,ij}$ is the unit strain. The superior index ij indicates the test cases. For a two-dimensional problem, there are three independent unit strains $\boldsymbol{\varepsilon}^{0,11} = [1, 0, 0]$, $\boldsymbol{\varepsilon}^{0,22} = [0, 1, 0]$ and $\boldsymbol{\varepsilon}^{0,12} = [0, 0, 1]$. The characteristic displacements $\boldsymbol{\chi}^{ij}$ are obtained numerically under periodic condition in the unit cell Y . Having these local solutions, the effective elasticity tensor \mathbb{C}^H of the unit cell is calculated by

$$C_{ijkl}^H = \frac{1}{|Y|} \int_Y (\varepsilon_{pq}^{0,ij} - \varepsilon_{pq}(\boldsymbol{\chi}^{ij})) C_{pqrs}(\mathbf{y}) (\varepsilon_{rs}^{0,kl} - \varepsilon_{rs}(\boldsymbol{\chi}^{kl})) \, d\Omega, \quad (2.5)$$

which essentially corresponds to the average of strain energy in the unit cell.

2.3 Level Set Function

In this section we briefly discuss the fundamentals of the level set method in structural optimization. The material distribution in the unit cell is represented via an implicit level set function defined in a reference domain Y as shown in Fig. 2.1(a) with

$$\begin{cases} \phi(\mathbf{x}) > 0, & \mathbf{x} \in \Omega \text{ (solid)} \\ \phi(\mathbf{x}) < 0, & \mathbf{x} \in Y/\Omega \text{ (void)} \\ \phi(\mathbf{x}) = 0, & \mathbf{x} \in \partial\Omega \text{ (boundary)}. \end{cases} \quad (2.6)$$

The interfaces between void and solid parts are considered as design boundaries. The evolution of the design boundaries in the optimization process is handled by the dynamic moving of the

zero level set $\phi(\mathbf{x}(\tau), \tau) = 0$. The dynamic change in time is governed by the Hamilton–Jacobi (H-J) equation

$$\frac{\partial \phi}{\partial t} - V_n |\nabla \phi| = 0, \quad V_n = \frac{d\mathbf{x}}{dt} \cdot \frac{\nabla \phi}{|\nabla \phi|}, \quad (2.7)$$

where V_n is the normal velocity component. In the steepest descend method, V_n is chosen such that the gradient of the objective function is negative to ensure the objective function is minimized. Conventionally, the level set function is updated by solving the Hamilton–Jacobi equation with a finite difference scheme [51, 52], and consequently a new design boundary is obtained and used to proceed with a next optimization iteration. It is noted that a restriction of step sizes is necessary to ensure numerical stability when solving the H-J equation with finite difference schemes, i.e., Courant–Friedrichs–Lewy (CFL) condition. Furthermore, the signed distance characteristic of the level set function should be maintained during the optimization procedure to avoid the flatness or steepness; therefore, additional re-initialization steps are provided periodically after several iterations [6, 52].

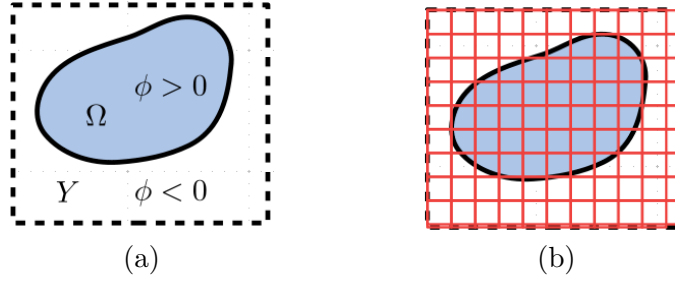


Figure 2.1: Unit cell geometry represented by a level set function (a) and fixed mesh on a square domain (b).

In this present work, the parameterized level set method (PLSM) [25, 53] is used. The level set function is approximated by

$$\phi(\mathbf{x}, \tau) = \sum_I^{ncp} R_I(\mathbf{x}) \alpha_I(\tau) = \mathbf{R}(\mathbf{x}) \cdot \boldsymbol{\alpha}(\tau), \quad (2.8)$$

and the H-J PDE equation reduces to an ordinary differential equation

$$\mathbf{R}^T \frac{d\boldsymbol{\alpha}}{d\tau} - V_n |(\nabla \mathbf{R})^T \boldsymbol{\alpha}| = 0 \quad \text{or} \quad V_n = \frac{\mathbf{R}^T \dot{\boldsymbol{\alpha}}}{|(\nabla \mathbf{R})^T \boldsymbol{\alpha}|} \quad (2.9)$$

where $R_I(\mathbf{x})$ are B-spline basis functions in the isogeometric concept. These functions will be discussed in Section 2.4. Herein, the expansion coefficients α_I are considered as design variables. The level set function is updated by changing values of the coefficients α_I during the optimization procedure. A gradient-based mathematical programming optimizer is used to optimize the design variables. Solving the H-J equation is avoided and the limit of step sizes to ensure numerical stability is unnecessary, so that the efficiency is improved. Furthermore, there is no re-initialization step to keep the level set function to be a signed distance function.

For a unit cell with two material phases, solid and void, as shown in Fig. 2.1(a), we can express spatial dependence in the elasticity tensor with a Heaviside function $\mathcal{H}(\phi)$ of the level set value. Equations (2.4) and (2.5) are written as

$$\int_Y \varepsilon_{pq}(\boldsymbol{\chi}^{ij}) C_{pqrs} \mathcal{H}(\phi(\mathbf{y})) \varepsilon_{rs}(\mathbf{v}) d\Omega = \int_Y \varepsilon_{pq}^{0,ij} C_{pqrs} \mathcal{H}(\phi(\mathbf{y})) \varepsilon_{rs}(\mathbf{v}) d\Omega, \quad (2.10)$$

$$C_{ijkl}^H = \frac{1}{|Y|} \int_Y \left(\varepsilon_{pq}^{0,ij} - \varepsilon_{pq}(\boldsymbol{\chi}^{ij}) \right) C_{pqrs} \mathcal{H}(\phi(\mathbf{y})) \left(\varepsilon_{rs}^{0,kl} - \varepsilon_{rs}(\boldsymbol{\chi}^{kl}) \right) d\Omega, \quad (2.11)$$

and for the volume of solid part

$$V = \int_Y \mathcal{H}(\phi(\mathbf{y})) d\Omega. \quad (2.12)$$

To obtain the derivative of the Heaviside function numerically, we use a regularized Heaviside function of the form

$$\mathcal{H}(\phi) = \begin{cases} \rho_{\min} & \phi < \xi \\ \frac{3}{4} \left(\frac{\phi}{\xi} - \frac{\phi^3}{3\xi^3} \right) + \frac{1}{2} & -\xi \leq \phi \leq \xi \\ 1 & \phi > \xi \end{cases} \quad (2.13)$$

where ξ is the smoothing length of the numerical Heaviside function, and $\rho_{\min} = 10^{-6}$ is chosen to avoid singularity in the numerical stiffness.

2.4 Isogeometric Analysis with Bézier Extraction

This section gives a brief description of the isogeometric analysis (IGA) concept [32] and the Bernstein-Bézier representation [54] to non-uniform rational basis functions (NURBS). Similar to the finite element approach, the actual geometry in the physical space is represented in a parameter space by using a mapping

$$\mathbf{T}(\boldsymbol{\xi}) = \sum_{I=1}^{ncp} R_I(\boldsymbol{\xi}) \mathbf{P}_I, \quad (2.14)$$

with a mesh of ncp control points \mathbf{P}_I and associated weights w_I . The NURBS basis functions $R_I(\boldsymbol{\xi})$ are defined as

$$R_I(\boldsymbol{\xi}) = \frac{w_I N_I(\boldsymbol{\xi})}{W} = \frac{w_I N_I(\boldsymbol{\xi})}{\sum_{J=1}^N N_J(\boldsymbol{\xi}) w_J}, \quad (2.15)$$

where the B-spline functions $N_I(\boldsymbol{\xi})$ of degree p are defined by the knot-vectors on a parameter domain $\Omega_{\boldsymbol{\xi}} = [0, 1]^d$:

$$\Xi^i := \{\xi_1^i, \dots, \xi_{n_i+p+1}^i\}, \quad 0 = \xi_1^i \leq \xi_2^i \leq \xi_{n_i+p+1}^i = 1 \quad \text{and} \quad i = 1, \dots, d, \quad (2.16)$$

and n_i is the number of B-spline functions in each spatial direction.

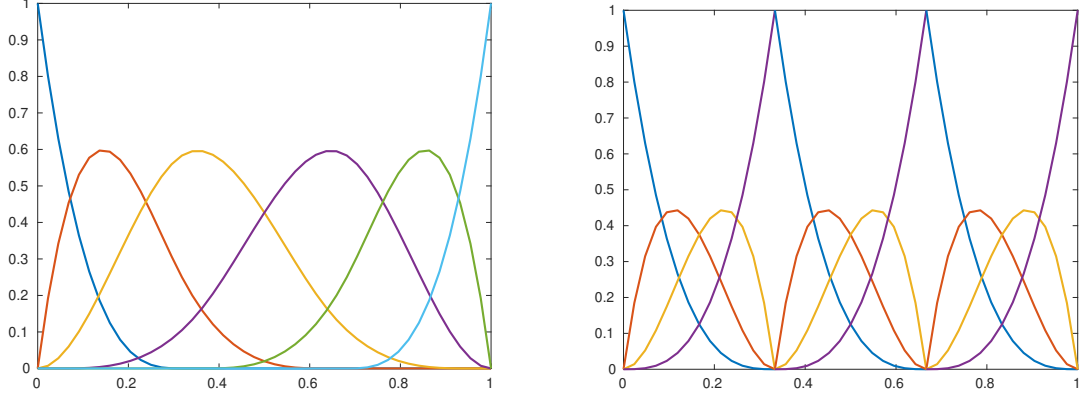


Figure 2.2: B-spline basis functions (left) and their corresponding Bernstein-Bézier representation (right).

B-spline basis functions in the parameter space span in several elements (knot spans), which makes numerical implementation more difficult. In order to use element-wise structures similar to the standard finite element method, B-spline basis functions are rewritten as a linear combination of the Bernstein polynomials $\mathbf{B}(\boldsymbol{\xi})$ defined on a parent element domain $[-1, 1]^d$, generating Bézier elements which have C^0 -continuity (see Fig. 2.2)

$$\mathbf{N}^e = \mathbf{C}^e \mathbf{B}(\boldsymbol{\xi}). \quad (2.17)$$

\mathbf{N}^e is a set of n B-spline basis functions associated to the Bézier element, i.e., $\mathbf{N}^e = [N_1^e, \dots, N_n^e]$. The localized extraction operator \mathbf{C}^e is constructed from the knot vector and is independent of control points as well as the B-spline basis functions. Similarly, NURBS basis functions within a Bézier element have the form:

$$\mathbf{R}^e(\boldsymbol{\xi}) = \frac{\mathbf{W}^e \mathbf{C}^e \mathbf{B}(\boldsymbol{\xi})}{\sum_{J=1}^n w_J N_J^e(\boldsymbol{\xi})} = \frac{\mathbf{W}^e \mathbf{N}^e(\boldsymbol{\xi})}{W(\boldsymbol{\xi})}, \quad (2.18)$$

where \mathbf{W}^e is a diagonal matrix of weights. The implementation of IGA using the Bézier extraction allows the possibility of using existing routines in the finite element codes, i.e, assembly and post-processing.

For a unit cell discretized by nel Bézier elements as shown in Fig. 2.1(b), the equilibrium equation (2.4) has the following expression in matrix form

$$\mathbf{K} \boldsymbol{\chi}^{ij} = \mathbf{F}^{ij}, \quad (2.19)$$

where the global stiffness matrix \mathbf{K} and force vector \mathbf{F}^{ij} are assembled from corresponding element matrix and vector

$$\mathbf{k}^e = \int_{\Omega^e} \mathbf{B}^T \mathbf{C} \mathbf{B} d\Omega^e, \quad \mathbf{f}^{e,ij} = \int_{\Omega^e} \mathbf{B}^T \mathbf{C} \boldsymbol{\varepsilon}^{0,ij} d\Omega^e. \quad (2.20)$$

Herein, \mathbf{B} is the standard matrix of elastic strain operator in solid mechanics [55], and \mathbf{C} is the matrix of elasticity coefficients. The effective elasticity tensor is calculated from characteristic

displacements:

$$C_{ijkl}^H = \frac{1}{|Y|} \sum_e^{nel} \int_{\Omega^e} [\boldsymbol{\varepsilon}^{0,ij} - \mathbf{B}\boldsymbol{\chi}^{ij}]^T \mathbf{C} [\boldsymbol{\varepsilon}^{0,kl} - \mathbf{B}\boldsymbol{\chi}^{kl}]. \quad (2.21)$$

2.5 Reduced Order Modelling

At each optimization iteration, the characteristic displacements $\boldsymbol{\chi}^{ij}$ are obtained by solving the system of equations (2.19) and the computational cost involved in the inversion of stiffness matrix \mathbf{K} is expensive in large scale problems. We aim at reducing the finite dimensional space $V_0^h \subset H^1$ by projecting the balance equation to subspace $\tilde{V}_0^h \subset V_0^h$ with lower dimension

$$\dim(\tilde{V}_0^h) = nb \ll \dim(V_0^h). \quad (2.22)$$

The task is to construct global ansatz functions $\theta_m(\mathbf{y})$ such that the subspace $\tilde{V}_0^h = \text{span}\{\theta_1, \dots, \theta_{nb}\}$, and solution fields in the reduced space are defined by

$$\boldsymbol{\chi}^h(\mathbf{y}) \simeq \tilde{\boldsymbol{\chi}}^h(\mathbf{y}) = \sum_m^{nb} \varphi_m \theta_m(\mathbf{y}). \quad (2.23)$$

The functions θ_m define the linear space \tilde{V}_0^h and are associated to the matrix of coefficients $\boldsymbol{\Phi} \in \mathbb{R}^{N \times nb}$ by

$$\theta_m(\mathbf{y}) = \sum_n^N \Phi_{nm} R_n(\mathbf{y}), \quad (2.24)$$

where R_n are basis functions defined in (2.14). The balance equations (2.19) have the size of $nb \ll N$ in the subspace and are formed as

$$\tilde{\mathbf{K}}\tilde{\boldsymbol{\chi}} = \tilde{\mathbf{F}}, \quad (2.25)$$

where $\boldsymbol{\chi} = \boldsymbol{\Phi}\tilde{\boldsymbol{\chi}}$, $\tilde{\mathbf{K}} = \boldsymbol{\Phi}^T \mathbf{K} \boldsymbol{\Phi}$ and $\tilde{\mathbf{F}} = \boldsymbol{\Phi}^T \mathbf{F}$. The superior indices ij in the characteristic displacements, constructed basis and force terms, are eliminated to avoid cumbersome.

The construction of the reduced basis follows the work by Gogu [30]. The key idea is to predict a new displacement solution and consequently a new topology by a set of solutions obtained from the previous optimization steps. We initialize the matrix $\boldsymbol{\Phi}$ with vectors of coefficients $\boldsymbol{\phi}_m$ calculated from the corresponding solutions $\boldsymbol{\chi}_m$ (i.e., displacements associated to control points) in the first nb iterations ($m = 1$). The first basis vector is given as

$$\boldsymbol{\phi}_1 = \frac{\boldsymbol{\chi}_1}{\|\boldsymbol{\chi}_1\|}. \quad (2.26)$$

The next basis vector is computed by the Gram-Schmidt orthogonalization and normalization:

$$\tilde{\boldsymbol{\phi}}_{m+1} = \boldsymbol{\chi}_{m+1} - \sum_j^m \langle \boldsymbol{\chi}_{m+1}, \boldsymbol{\phi}_j \rangle \boldsymbol{\phi}_j \quad (2.27)$$

$$\boldsymbol{\phi}_{m+1} = \frac{\tilde{\boldsymbol{\phi}}_{m+1}}{\|\tilde{\boldsymbol{\phi}}_{m+1}\|}, \quad m = 1, \dots, (nb - 1).$$

Once the reduced basis is formed, a solution in the next iteration is obtained in the subspace of dimension nb and then transformed back to full space by using (2.25). In order to assess the accuracy of the solution obtained from the reduced basis, the following error measurement is suggested (see also Gogu [30])

$$error = \frac{\|\mathbf{K}\Phi\tilde{\chi} - \mathbf{F}\|}{\|\mathbf{F}\|} < tol. \quad (2.28)$$

If the error is acceptable, the optimization algorithm is conducted using the reduced solution. Otherwise, a full solution is calculated and used for the computations at the subsequent steps. After each successful iteration, the reduced basis is enriched by adding the new accepted solution. The comparison of conventional optimization algorithms and those with reduced basis model is shown in Fig. 2.3. The two flowcharts have similar procedures except for the decision of using reduced solutions in subsequent steps (red box).

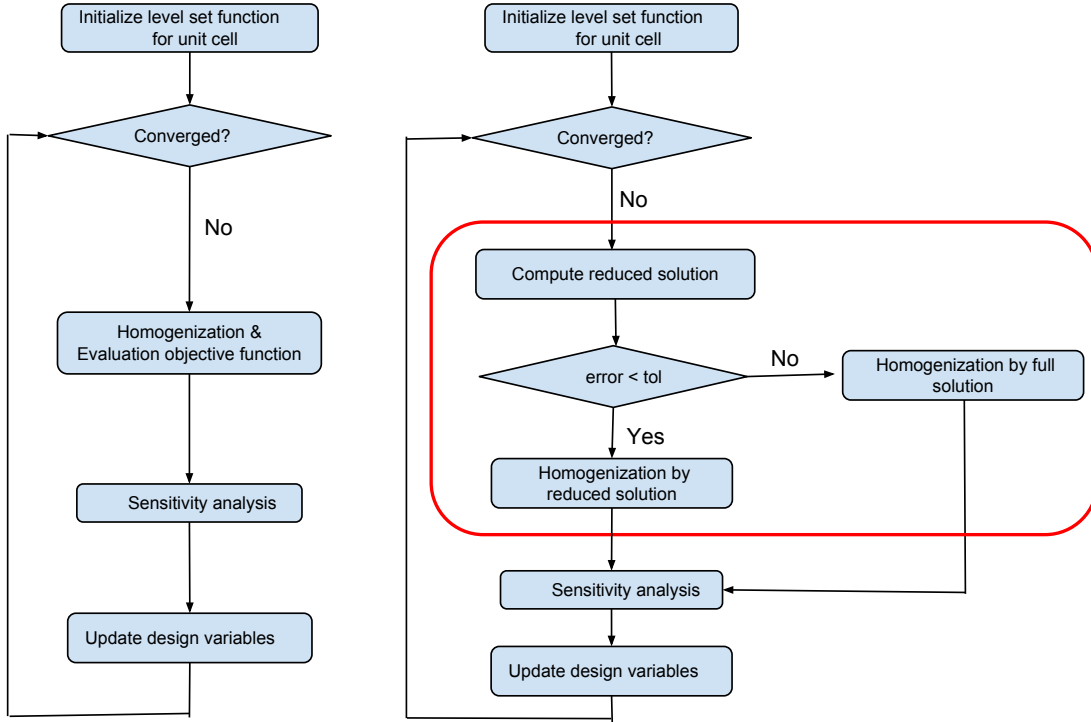


Figure 2.3: Microstructure topology optimization algorithm with and without reduced basis model.

This approach is similar to alternative projection-based methods, i.e., mode superposition, Ritz vectors method [56], or the proper orthogonal decomposition [57]. The original problem is solved for different values of the considered parameters in an offline stage and the pre-calculated solutions are then collected in order to construct a subspace. However, it is difficult to construct such parameter spaces in a topological shape optimization problem. The number of parameters needs to be large enough to represent all possibilities of shape or topology changes, which makes the reduced solutions inaccurate or difficult to obtain. Instead of using the offline strategy, the stored displacements from consecutive iterations during the optimization process are used here to construct the subspace, and a reduced solution ob-

tained without solving the full system in the subsequent iteration is expected to satisfy the equilibrium equation.

2.6 Sensitivity Analysis

Due to the gradient-based optimization algorithm which is used, it is necessary to find the derivatives of the objective function and constraints with respect to the design variables α_I . We follow the shape design sensitivity analysis by Choi and Kim [58]. The shape boundary of the physical domain is considered as the design variable, and shape sensitivity analyzes the relation of shape boundary perturbations to the objective function or constraints. By representing the shape boundary by a zero level set function, the perturbations of the shape boundary become a dynamic evolution of the level set function in time. The derivative of a domain functional with respect to shape can be replaced by the time derivative [51, 52]. In order to include the reduced solutions to the optimization algorithm, we define a general objective function for each component of the homogenized elastic tensor as follows

$$J(\tilde{\chi}, \chi, \mathbf{v}, \boldsymbol{\lambda}, \phi) = f(\tilde{\chi}, \phi) + (a(\tilde{\chi}, \mathbf{v}, \phi) - l(\mathbf{v}, \phi)) + \sum_m^{nb} (a(\chi_m, \boldsymbol{\lambda}_m, \phi) - l(\boldsymbol{\lambda}_m, \phi)), \quad (2.29)$$

where

$$f(\tilde{\chi}, \phi) = \int_Y (\varepsilon_{pq}^{0,ij} - \varepsilon_{pq}(\tilde{\chi}^{ij})) C_{pqrs} (\varepsilon_{rs}^{0,kl} - \varepsilon_{rs}(\tilde{\chi}^{kl})) \mathcal{H}(\phi) d\Omega, \quad (2.30)$$

and variational problems in the reduced sub-space \tilde{V}_0^h and in the finite dimensional space V_0^h are defined respectively as

$$\begin{aligned} a(\tilde{\chi}, \mathbf{v}, \phi) &= \int_Y \varepsilon_{pq}(\tilde{\chi}^{ij}) C_{pqrs} \mathcal{H}(\phi) \varepsilon_{rs}(\mathbf{v}) d\Omega \\ l(\mathbf{v}, \phi) &= \int_Y \varepsilon_{pq}^{0,ij} C_{pqrs} \mathcal{H}(\phi) \varepsilon_{rs}(\mathbf{v}) d\Omega \\ a(\chi_m, \boldsymbol{\lambda}_m, \phi) &= \int_Y \varepsilon_{pq}(\chi_m^{ij}) C_{pqrs} \mathcal{H}(\phi) \varepsilon_{rs}(\boldsymbol{\lambda}_m) d\Omega \\ l(\boldsymbol{\lambda}_m, \phi) &= \int_Y \varepsilon_{pq}^{0,ij} C_{pqrs} \mathcal{H}(\phi) \varepsilon_{rs}(\boldsymbol{\lambda}_m) d\Omega. \end{aligned} \quad (2.31)$$

The subscript m indicates the full solutions χ_m were used to construct reduced basis ϕ_m . Shape derivatives of the objective function are given as

$$\begin{aligned} \dot{J} &= f(\dot{\tilde{\chi}}, \phi) + f(\tilde{\chi}, \dot{\phi}) + a(\dot{\tilde{\chi}}, \mathbf{v}, \phi) + a(\tilde{\chi}, \dot{\mathbf{v}}, \phi) + a(\tilde{\chi}, \mathbf{v}, \dot{\phi}) - l(\dot{\mathbf{v}}, \phi) - l(\mathbf{v}, \dot{\phi}) \\ &+ \sum_m^{nb} \left(a(\dot{\chi}_m, \boldsymbol{\lambda}_m, \phi) + a(\chi_m, \dot{\boldsymbol{\lambda}}_m, \phi) + a(\chi_m, \boldsymbol{\lambda}_m, \dot{\phi}) - l(\dot{\boldsymbol{\lambda}}_m, \phi) - l(\boldsymbol{\lambda}_m, \dot{\phi}) \right), \end{aligned} \quad (2.32)$$

where the terms containing time derivatives, for example of the homogenized elastic tensor, have forms as

$$\begin{aligned} f(\tilde{\boldsymbol{\chi}}, \phi) &= \int_Y (\varepsilon_{pq}^{0,ij} - \varepsilon_{pq}(\tilde{\boldsymbol{\chi}}^{ij})) C_{pqrs} (\varepsilon_{rs}^{0,kl} - \varepsilon_{rs}(\tilde{\boldsymbol{\chi}}^{kl})) \delta(\phi) |\nabla\phi| V_n d\Omega, \\ f(\dot{\tilde{\boldsymbol{\chi}}}, \phi) &= \int_Y -2\varepsilon_{pq}(\dot{\tilde{\boldsymbol{\chi}}}^{ij}) C_{pqrs} (\varepsilon_{rs}^{0,kl} - \varepsilon_{rs}(\tilde{\boldsymbol{\chi}}^{kl})) \mathcal{H}(\phi) d\Omega, \end{aligned} \quad (2.33)$$

$\delta(\circ) = \mathcal{H}'(\circ)$ being the Dirac delta function. To avoid calculating the time derivative of the characteristic displacement $\tilde{\boldsymbol{\chi}}$ in (2.32), the following adjoint equation is established and solved for \mathbf{v} in general.

$$f(\dot{\tilde{\boldsymbol{\chi}}}, \phi) + a(\dot{\tilde{\boldsymbol{\chi}}}, \mathbf{v}, \phi) = 0. \quad (2.34)$$

In fact (2.34) is a self-adjoint problem and is satisfied if the test function \mathbf{v} is properly selected such that

$$\varepsilon_{rs}(\mathbf{v}) = 2 \left(\varepsilon_{rs}^{0,kl} - \varepsilon_{rs}(\tilde{\boldsymbol{\chi}}^{kl}) \right). \quad (2.35)$$

All the terms containing $\dot{\boldsymbol{\lambda}}_m$ can be eliminated since the following relations hold true

$$a(\boldsymbol{\chi}_m, \dot{\boldsymbol{\lambda}}_m, \phi) = l(\dot{\boldsymbol{\lambda}}_m, \phi) \quad \forall \dot{\boldsymbol{\lambda}}_m \in V_0^h, \quad m = 1, \dots, nb. \quad (2.36)$$

If the standard solution is used instead of reduced solutions, i.e., $\tilde{\boldsymbol{\chi}} \rightarrow \boldsymbol{\chi}$, the residual is defined by

$$r(\tilde{\boldsymbol{\chi}}, \dot{\mathbf{v}}, \phi) = a(\tilde{\boldsymbol{\chi}}, \dot{\mathbf{v}}, \phi) - l(\dot{\mathbf{v}}, \phi) = 0, \quad \forall \dot{\mathbf{v}} \in V_0^h. \quad (2.37)$$

In this case, shape derivatives of the homogenized elastic tensor are

$$\frac{\partial J}{\partial \tau} = \frac{\partial C_{ijkl}^H}{\partial \tau} = - \int_Y (\varepsilon_{pq}^{0,ij} - \varepsilon_{pq}(\boldsymbol{\chi}^{ij})) C_{pqrs} (\varepsilon_{rs}^{0,kl} - \varepsilon_{rs}(\boldsymbol{\chi}^{kl})) \delta(\phi) |\nabla\phi| V_n d\Omega. \quad (2.38)$$

If a reduced solution $\tilde{\boldsymbol{\chi}}$ is used, the residual is non-zero and written as

$$r(\tilde{\boldsymbol{\chi}}, \dot{\mathbf{v}}, \phi) = r(\tilde{\boldsymbol{\chi}}, \sum_m^{nb} \varphi_m \dot{\boldsymbol{\theta}}_m, \phi) = \sum_m^{nb} \varphi_m r(\tilde{\boldsymbol{\chi}}, \dot{\boldsymbol{\theta}}_m, \phi). \quad (2.39)$$

To eliminate the quantity $\dot{\boldsymbol{\chi}}_m$ in (2.32), the following adjoint equations are formed for each set of the balance equations

$$a(\dot{\boldsymbol{\chi}}_m, \boldsymbol{\lambda}_m, \phi) + \varphi_m r(\tilde{\boldsymbol{\chi}}, \dot{\boldsymbol{\theta}}_m, \phi) = 0, \quad m = 1, \dots, nb. \quad (2.40)$$

As the global ansatz function θ_m is constructed from the standard solutions χ in the finite-dimensional space V_0^h (see Eq. (2.24), (2.26)-(2.27)) and as the bilinear form $a(\circ, \circ)$ is symmetric in its arguments, the adjoint equation finally has the form as

$$a(\boldsymbol{\lambda}_m, \dot{\boldsymbol{\chi}}_m, \phi) + \varphi_m r(\tilde{\boldsymbol{\chi}}, \dot{\boldsymbol{\chi}}_m, \phi) = 0, \quad m = 1, \dots, nb \quad (2.41)$$

and solved for the adjoint variables λ_m . The final expression of the sensitivity is

$$\dot{J} = f(\tilde{\chi}, \dot{\phi}) + a(\tilde{\chi}, \mathbf{v}, \dot{\phi}) - l(\mathbf{v}, \dot{\phi}) + \sum_m^{nb} \left(a(\chi_m, \lambda_m, \dot{\phi}) - l(\lambda_m, \dot{\phi}) \right) \quad (2.42)$$

in which adjoint variables \mathbf{v} and λ_m are obtained from the self-adjoint problem (2.35) and (2.41) respectively. If the Hamilton-Jacobi equation is replaced by an original differential equation (2.9), any integral function involving the normal velocity component

$$\dot{j} = \frac{\partial J(\circ, \phi)}{\partial \tau} = g(\circ, \dot{\phi}) = \int_Y (\circ) \delta(\phi) |\nabla \phi| V_n d\Omega \quad (2.43)$$

can be written as

$$\frac{\partial J(\circ, \phi)}{\partial \tau} = \sum_{I=1}^{ncp} \left(\int_Y (\circ) \delta(\phi) R_I(\mathbf{x}) d\Omega \right) \cdot \dot{\alpha}_I. \quad (2.44)$$

Additionally, the time derivative of the objective function J can be obtained by applying the chain rule

$$\frac{\partial J(\circ, \phi)}{\partial \tau} = \sum_{I=1}^{ncp} \frac{\partial J(\circ, \phi)}{\partial \alpha_I} \frac{\partial \alpha_I}{\partial \tau}. \quad (2.45)$$

By comparing (2.45) and (2.44), the sensitivity analysis of the objective function with respect to the design variable α_I is

$$\frac{\partial J(\circ, \phi)}{\partial \alpha_I} = \int_Y (\circ) \delta(\phi) R_I(\mathbf{x}) d\Omega. \quad (2.46)$$

The sensitivity analysis of volume constraint is given as

$$\frac{\partial V}{\partial \alpha_I} = \int_Y \delta(\phi) R_I(\mathbf{x}) d\Omega. \quad (2.47)$$

2.7 Objective Function of Topology Optimization for Meta-materials

The homogenization method detailed in Section 2.2 allows to predict the macroscopic properties of composites from a unit cell geometry. Designing the behavior of composite material is replaced by designing a unit cell such that the effective properties meet requirements. Seeking for auxetic materials turns into designing the effective elasticity tensor having negative Poisson's ratio. Therefore, we can assume that the target properties of material are given, and the optimization process is to search for the unit cell geometries such that the difference

between effective properties and target properties is minimized.

$$\begin{aligned} \min \quad & J_1 = \frac{1}{2} \sum_{i,j,k,l=1}^d \omega_{ijkl} \times (C_{ijkl} - C_{ijkl}^*)^2 \\ \text{s.t.} \quad & \begin{cases} a(\boldsymbol{\chi}, \mathbf{v}, \phi) = l(\mathbf{v}, \phi) & (\text{equilibrium equation}) \\ V(\phi) = \int_Y \mathcal{H}(\phi) d\Omega \leq v_f & (\text{volume constraint}) \\ \alpha_{\min} \leq \alpha_i \leq \alpha_{\max} \quad (i = 1, 2, \dots, N) & (\text{design variable constraint}) \end{cases} \end{aligned} \quad (2.48)$$

where C_{ijkl}^* are the components of the target elasticity matrix which has the following form in the two-dimensional setting

$$\mathbf{C}^* = \begin{bmatrix} C_{1111}^* & C_{1122}^* & 0 \\ C_{1122}^* & C_{2222}^* & 0 \\ 0 & 0 & C_{1212}^* \end{bmatrix}, \quad (2.49)$$

and ω_{ijkl} are weighting factors used in the least-square function. The bilinear energy form $a(\boldsymbol{\chi}, \mathbf{v}, \phi)$ and linear load form $l(\mathbf{v}, \phi)$ are defined in (2.10).

2.8 Numerical Examples

We first consider 2D unit cells subjected to plane stress conditions and discretized with an IGA mesh with 60×60 order $p = 2$ polynomial Bézier elements. The solid part in the unit cell is constituted by an isotropic material having Young's modulus $E = 1.0$ GPa and Poisson's ratio $\nu = 0.3$. The target elasticity components are set to $C_{1111}^* = C_{2222}^* = 0.1$, $C_{1122}^* = -0.05$ which ensures that the final configuration has negative Poisson's ratio. We set the weighting factors $\omega_{1111} = \omega_{2222} = 0.01$, $\omega_{1122} = 0.5$. For a level set function initialized with expansion coefficients, the upper bound $\alpha_{\max} = \max\{\alpha_I^0\}$ and lower bound $\alpha_{\min} = \min\{\alpha_I^0\}$ are chosen in the subsequent iterations. We use the method of moving asymptotic (MMA) [59] to update the design variables. Orthotropic materials are obtained by considering the geometry symmetry of square unit cells, the expansion coefficients α_I in one quarter of the unit cell are updated and the remaining configurations are obtained from the reflectional symmetry.

Optimal solutions corresponding to different initial configurations and target volumes are given in Fig. 2.4. Despite the initial configurations consist of simple circles, the complex shapes with sharp boundaries and thin ribs occur in the designs. There is no gray area or blur boundaries, the solid and void interfaces are clear. The verification or fabrication procedure can be directly performed for those final designs. These advantages of features of level set methods are highly preferable. Final shapes of unit cells are different due to the fact that the optimization algorithm (MMA) is a local optimizer. To summarize, the generated unit cells with negative Poisson ratios are obtained and similar to well-known auxetic structures: anti-tetra-chiral structures [60] (see Fig. 2.4(c)), re-entrant structures [61] (see Fig. 2.4(b, d)), or auxetic microstructures obtained with SIMP [62] (see Fig. 2.4(a, e)).

The volume fraction constraints significantly affect the final designs. In fact, negative Poisson's ratio in materials is created by a mechanism with trusses or beams connected

through hinges. These structures induce perpendicular motions among components by bending or rotating at the hinges. As much material is removed, a higher possibility of thin layers is produced. The amount of material removed also drives elastic stiffness of unit cells, this is a trade-off between the effective Young modulus and negative Poisson ratios in auxetic microstructure optimization. Softer materials have higher auxetic effects and vice-versa.

Geometries of the unit cell are plotted at selected iterations shown in [Fig. 2.5](#) illustrating topology change during the optimization process. At the beginning, material is removed to satisfy the volume constraint and the objective function oscillates significantly within the first 20 iterations. Topology changes mainly take place in this material removal process. Dynamic moving of boundaries with merging and splitting allows to remove existing holes or create new holes, increasing the design flexibility of shape and topology. Solid domains link together and meaningless features like islands are eliminated while the objective function values are reducing gradually. After 125 iterations, the objective function is kept unchanged and Poisson ratios are minimized.

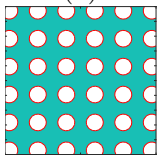
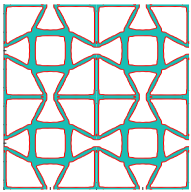
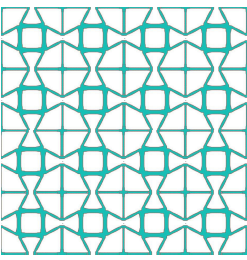
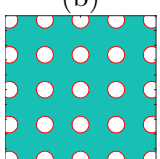
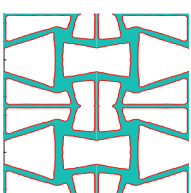
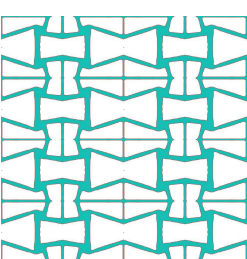
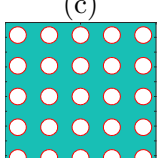
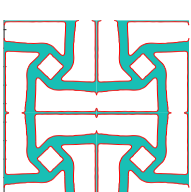
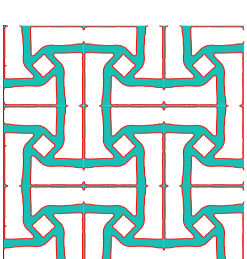
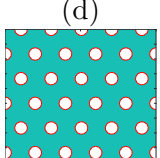
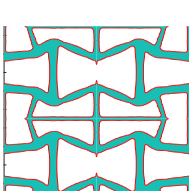
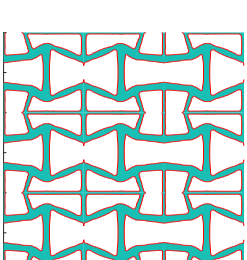
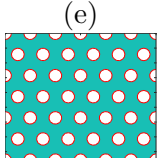
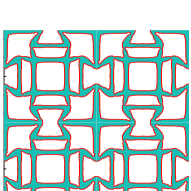
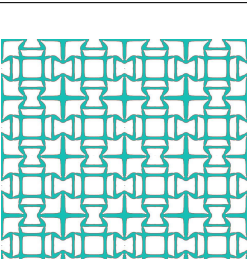
Initial design	Optimized unit cell	2×2 repeated unit cells	Effective property & volume fraction
(a) 			$\mathbf{C}^H = \begin{bmatrix} 0.0658 & -0.0372 & 0 \\ -0.0372 & 0.0658 & 0 \\ 0 & 0 & 0.0020 \end{bmatrix}$ $V_f = 0.275$ $\nu_{xy} = \nu_{yx} = -0.565$
(b) 			$\mathbf{C}^H = \begin{bmatrix} 0.0921 & -0.0430 & 0 \\ -0.0430 & 0.05 & 0 \\ 0 & 0 & 0.0014 \end{bmatrix}$ $V_f = 0.275$ $\nu_{xy} = -0.466, \nu_{yx} = -0.860$
(c) 			$\mathbf{C}^H = \begin{bmatrix} 0.046 & -0.039 & 0 \\ -0.039 & 0.046 & 0 \\ 0 & 0 & 0.0012 \end{bmatrix}$ $V_f = 0.3$ $\nu_{xy} = \nu_{yx} = -0.830$
(d) 			$\mathbf{C}^H = \begin{bmatrix} 0.1094 & -0.0419 & 0 \\ -0.0419 & 0.052 & 0 \\ 0 & 0 & 0.0018 \end{bmatrix}$ $V_f = 0.3$ $\nu_{xy} = -0.383, \nu_{yx} = -0.805$
(e) 			$\mathbf{C}^H = \begin{bmatrix} 0.0840 & -0.0507 & 0 \\ -0.0507 & 0.0840 & 0 \\ 0 & 0 & 0.004 \end{bmatrix}$ $V_f = 0.35$ $\nu_{xy} = \nu_{yx} = -0.603$

Figure 2.4: Influence of initial configurations and volume fraction to final designs.

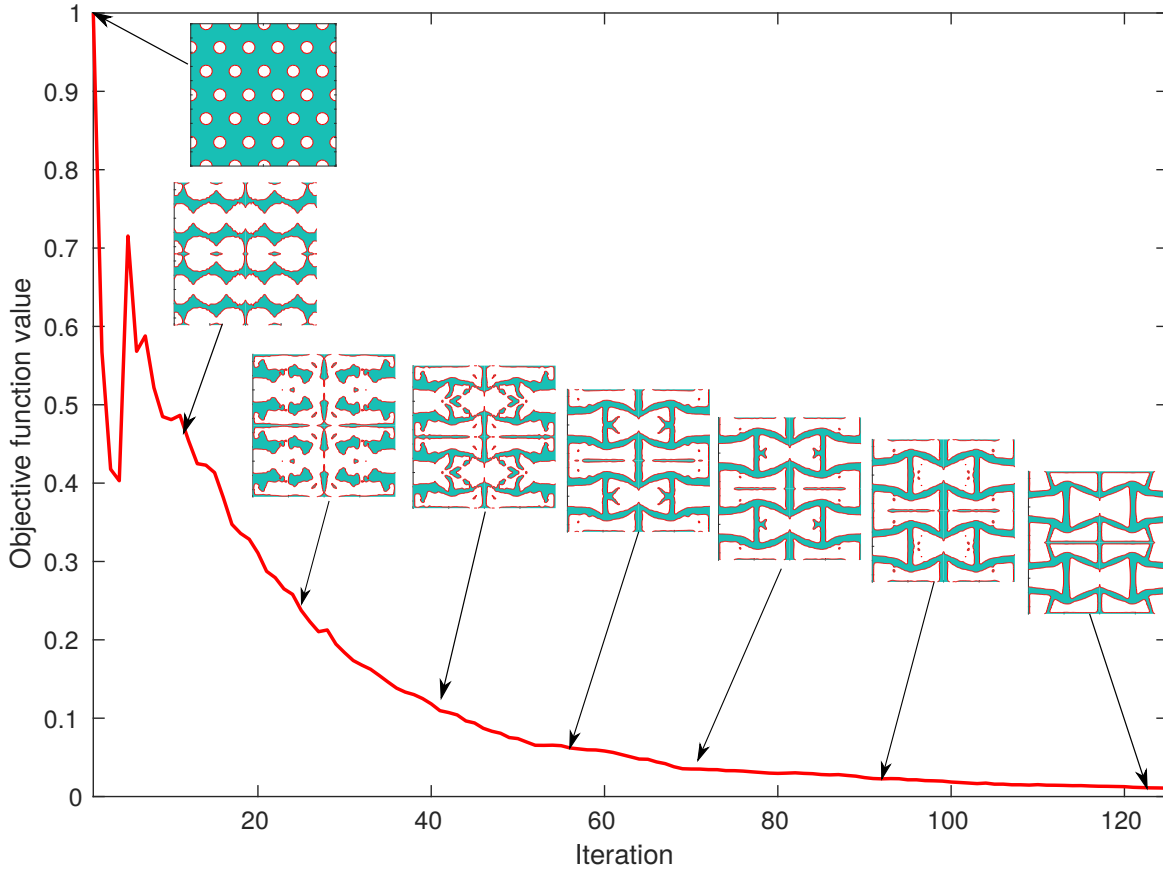


Figure 2.5: Convergence of the objective function.

We next investigate the influence of the reduced basis approach to the convergence rate and final design. The same initial configuration is considered but the algorithm with reduced order model (as shown in Fig. 2.3) is used in this example. A reduced basis with size $nb = 12$ is constructed and enriched during the optimization process. Reduced solutions are accepted and used in further calculation steps if the residual error is smaller than a threshold $tol = 0.01$ for all test cases ($mn = 11, 22, 12$) simultaneously. As shown in Fig. 2.6, the objective function varies dramatically in the first few iterations along with the large change in shape and topology due to material removal. These imply that the reduced solutions, generated by a set of different configurations, will not satisfy the condition (2.28), and full solutions are required to be computed. When the objective function values are gradually decreasing, a set of similar geometries and corresponding basis vectors enrich the reduced basis sufficiently; this subspace enables to produce reduced solutions which are accurate enough to proceed with the next calculation steps. The blue squares indicate that the optimization algorithm applies the reduced model order successfully and computational burden of solving the original system is eliminated by inverting the systems with small size, i.e., $nb = 12$.

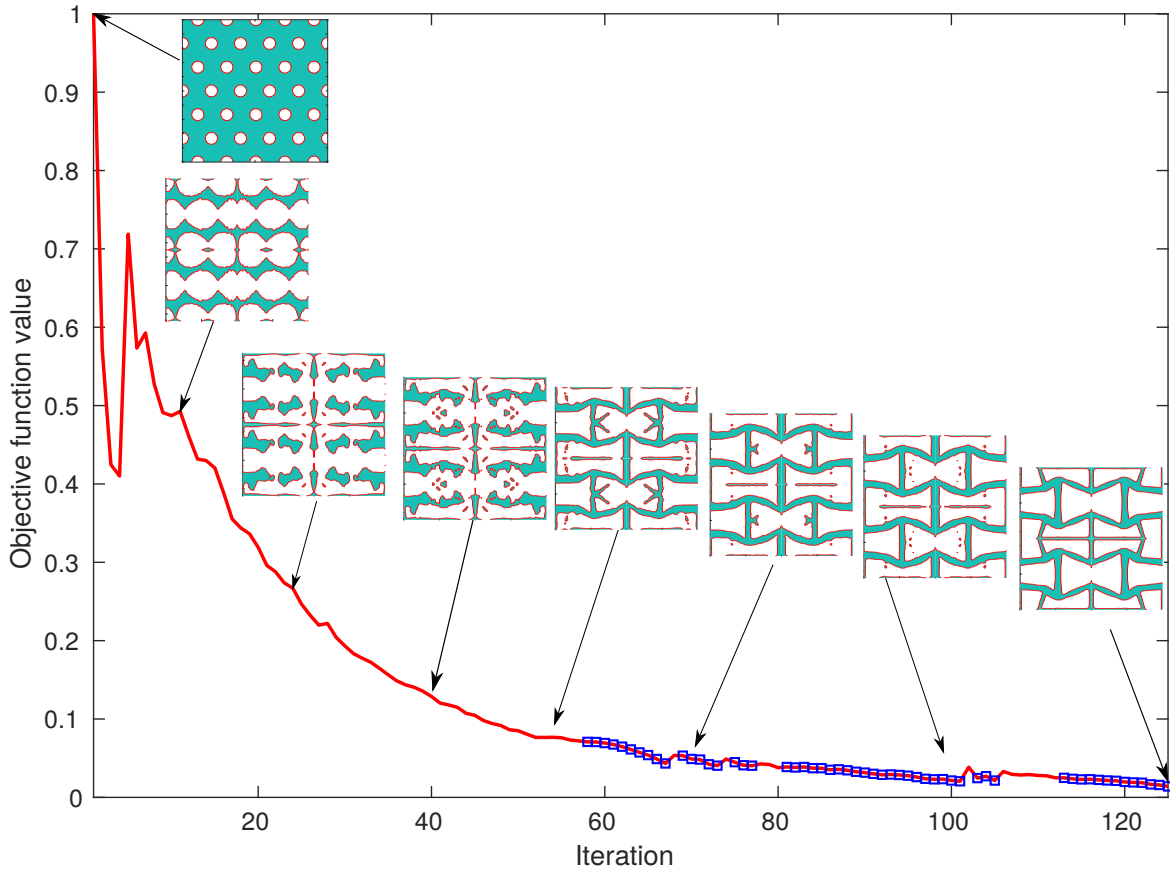


Figure 2.6: Convergence of the objective function by using the algorithm with reduced order model in Fig. 2.3 (right). Blue squares indicate the reduced solutions are used.

We further design three-dimensional metamaterials with negative Poisson’s ratio by considering a cubic unit cell and investigate the efficiency of using reduced modeling when the size of problems is increased. Design domains are discretized with 40^3 quadratic Bézier elements thus leading to moderately large models which are time consuming if balance equations are solved in the finite dimensional space V_0^h . We use a reduced basis with $nb = 12$ and errors smaller than $tol = 0.01$ to decide whether the reduced solutions are accurate and subsequently employed to advance a new topology. Figure 2.7 provides optimized structures and corresponding homogenized elastic tensors which are results of optimization algorithm with reduced modeling. Designed geometries exhibit auxetic effect if the structures are under compression or tension. Due to the nature of gradient-based algorithms which accept local optimums, final results can be different although the same target elastic tensor is set for the objective functions.

The plot of convergence in Fig. 2.8 indicates iterations in which reduced modeling applied successfully. A similar behavior of the algorithm as shown in the two-dimensional problem (cf. Fig. 2.6) is also observed in this 3D example. Significant changes in topology and shapes lead a reduced basis at the initial stage can not produce accurate solutions. Afterwards, the shapes and topology advance gradually resulting on similar geometries produced and the reduced basis constructed from full solutions are able to reproduce accurate solutions used in next consecutive steps.

The feasibility of using reduced solutions in shape and topology optimization can trace back to reduced order models using the offline strategy. In these approaches, a set of parameters can represent the geometry adjustment, and pre-calculated solutions of the model are obtained by evaluating at selected parameter values. It is noted that when the variation of parameters does not result in a very large change of geometry shape or topology, this allows the reduced basis to generate accurate solutions. In this current work, a similar idea for constructing the reduced basis is employed. Indeed, the stored solutions obtained from geometries are used to construct the reduced subspace. The amount of difference in geometries decides the enrichment level of the reduced basis and the accuracy of reduced solutions. The method is practical since minor changes in geometries always appear after several iterations (see Fig. 2.6 and Fig. 2.8).

The computation time and number of iterations required in the 3D examples are summarized in Tab. 2.1. We simulate examples in similar settings but with and without using the reduced order model. We purposely eliminate all possible instabilities and keep the optimizer conservative by using small moving stepsizes [63], hence, the number of iterations is relatively large in all numerical examples. In this way, we can have adequate comparisons between the two algorithms and can emphasize the outperformance of the reduced order technique. The total CPU time required in full model is larger although fewer number of iterations are used. In such large scale problems, the time for stiffness matrix assembly is negligible and the computational cost of solving the system of equation is dominant. If reduced solutions are accurate enough to advance new topology in the consecutive step, the computational cost of solving original large equations is eliminated by determining solutions of system with small size of $nb \times nb$ and a speed-up of factor 6.0 in solving the equation is achieved.

In three dimensional examples, the computational efficiency is much improved in terms of CPU times when compared to the algorithm without reduced order model. Nevertheless, the simulations required large numbers of iterations to reach convergence. We adopted different reduced basis sizes $nb = [10 - 50]$, and considered the efficiency in each case with regard to numbers of iterations and fluctuation of the objective functions. If the simulation uses a larger size of reduced basis, the convergence rates seem to be monotonic and the fluctuation is eliminated, but these improvements do not happen for all larger nb . It is challenging to systematize such data and contrive a pattern for this phenomenon, hence we simply employ a minimum proper number $nb = 12$ such that the algorithms can perform and have adequate comparison among simulations.

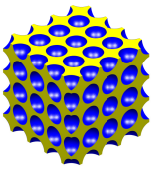
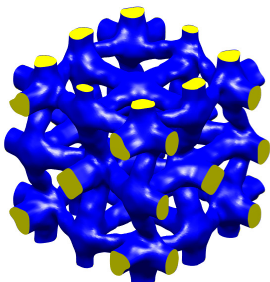
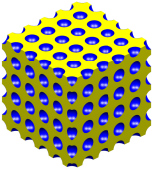
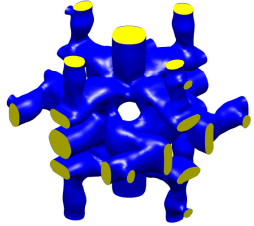
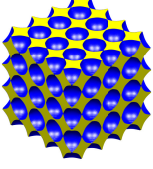
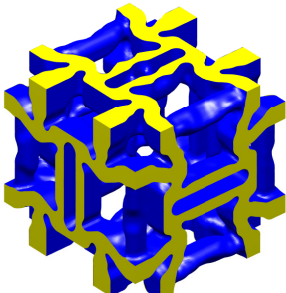
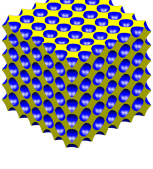
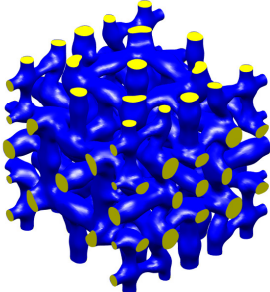
Initial design	Optimized unit cell	Effective property \mathbf{C}^H & volume fraction
(a) 		$0.1 \times \begin{bmatrix} 0.29 & -0.11 & -0.095 & 0 & 0 & 0 \\ -0.11 & 0.38 & -0.063 & 0 & 0 & 0 \\ -0.095 & -0.063 & 0.50 & 0 & 0 & 0 \\ 0 & 0 & 0 & 0.04 & 0 & 0 \\ 0 & 0 & 0 & 0 & 0.03 & 0 \\ 0 & 0 & 0 & 0 & 0 & 0.03 \end{bmatrix}$ $V_f = 0.225$
(b) 		$0.1 \times \begin{bmatrix} 0.34 & -0.077 & -0.048 & 0 & 0 & 0 \\ -0.077 & 0.4 & -0.053 & 0 & 0 & 0 \\ -0.048 & -0.053 & 0.27 & 0 & 0 & 0 \\ 0 & 0 & 0 & 0.016 & 0 & 0 \\ 0 & 0 & 0 & 0 & 0.013 & 0 \\ 0 & 0 & 0 & 0 & 0 & 0.017 \end{bmatrix}$ $V_f = 0.25$
(c) 		$0.1 \times \begin{bmatrix} 0.5 & -0.086 & -0.083 & 0 & 0 & 0 \\ -0.086 & 0.65 & -0.09 & 0 & 0 & 0 \\ -0.083 & -0.09 & 0.61 & 0 & 0 & 0 \\ 0 & 0 & 0 & 0.046 & 0 & 0 \\ 0 & 0 & 0 & 0 & 0.047 & 0 \\ 0 & 0 & 0 & 0 & 0 & 0.052 \end{bmatrix}$ $V_f = 0.3$
(d) 		$0.1 \times \begin{bmatrix} 0.44 & -0.069 & -0.092 & 0 & 0 & 0 \\ -0.069 & 0.51 & -0.012 & 0 & 0 & 0 \\ -0.092 & -0.012 & 0.61 & 0 & 0 & 0 \\ 0 & 0 & 0 & 0.038 & 0 & 0 \\ 0 & 0 & 0 & 0 & 0.042 & 0 \\ 0 & 0 & 0 & 0 & 0 & 0.05 \end{bmatrix}$ $V_f = 0.3$

Figure 2.7: Influence of initial configurations and volume fractions to final designs in three-dimensional metamaterials design.

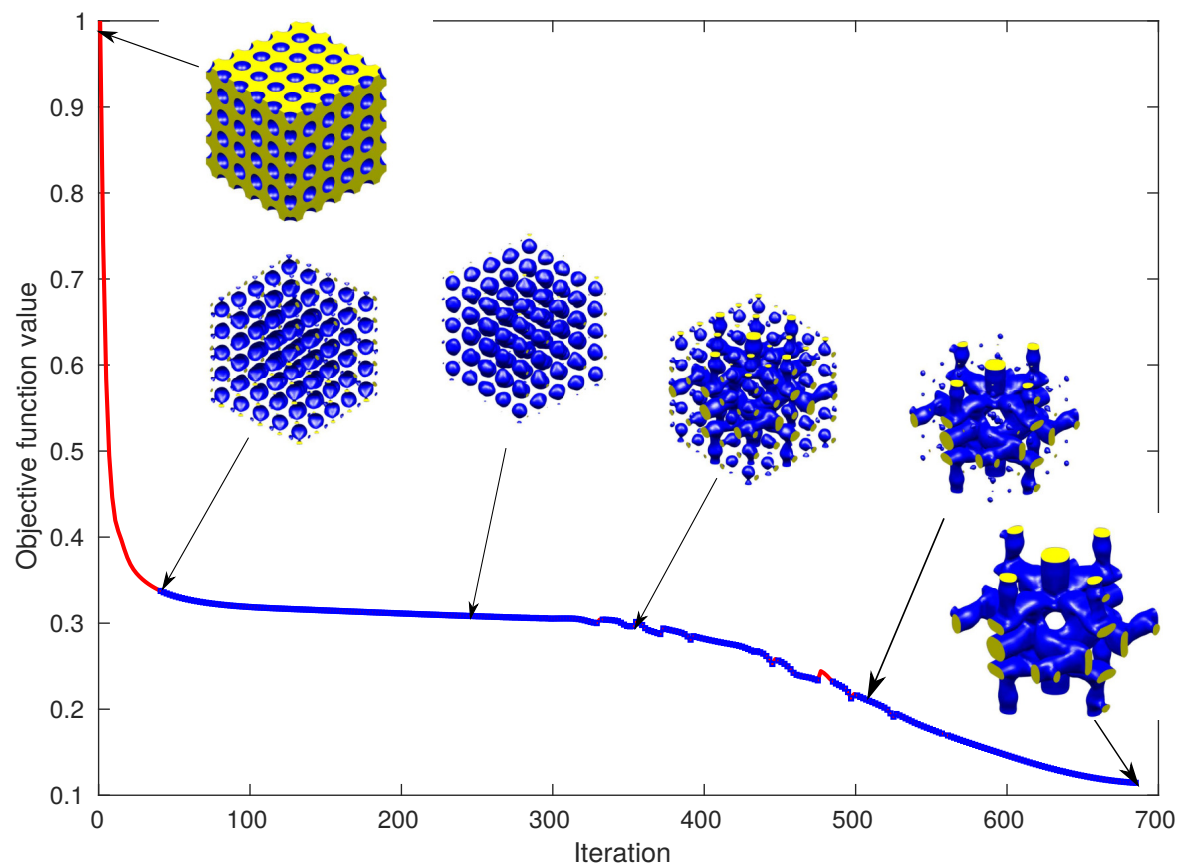


Figure 2.8: Convergence of the objective function (of the unit cell in Fig. 2.7b) by using the algorithm with reduced order modeling. Blue squares indicate the reduced solutions are used.

Unit cells	Full model		Reduced order model		
	Number of iterations	CPU time (in hour)	Number of iterations	Number of iterations using reduced solution	CPU time (in hour)
a	420	12.25	624	532	10.25
b	672	19.3	685	628	10.9
c	525	16.6	578	503	11.4
d	480	15.2	472	403	8.9

Table 2.1: Computation time of the 3D examples with and without using reduced order modelling.

2.9 Discussion and Conclusion

Material microstructures with negative effective Poisson’s ratio have been designed by topology optimization. Asymptotic homogenization method and sensitivity analysis of the effective elasticity tensor were revised and numerically implemented by isogeometric analysis with Bézier extraction. Geometries of the unit cell were represented by a parameterized level set function which allows flexible changes in shape and topology designs, and optimized structures having clear boundaries in order to be able to make prototypes with 3D printers directly.

A reduced order modeling combined with topology optimization was introduced to improve

the computational efficiency in solving the linear system of equations. The numerical results showed that such a combination is beneficial in topology optimization and could be extended to other physical problems such as improving electrical coefficients, or negative thermal expansion materials. Beside feasibility of the approach, more studies on the influences of reduced bases to solution accuracy with an appropriate error indicator, and implementation of the reduced order model with adaptive sizes of the bases, should be elaborated in future works in order to control the convergence rates.

Chapter 3

Topology Optimization of 1-3 Piezoelectric Composites

3.1 Introduction

This work presents a design procedure for piezoelectric composite materials used in hydrophone applications which typically operate in low frequencies with a wavelength being much larger than the lateral dimensions of the composite plate. The considered class is 1-3 piezocomposites which are constructed by embedding piezoceramic rods in a polymer matrix (see Fig. 3.1). The combination of a polymer matrix and piezoelectric ceramic rods enhances the flexibility of overall structures and allows the possibility of working under high pressure conditions, since the polymer is low-density and flexible in contrast to piezoelectric ceramics which are high-density and brittle.

By assuming the piezocomposite behaves as a homogeneous medium, many studies have proposed analytical solutions for calculating the effective moduli of 1-3 piezoelectric composite with the simple geometry. The initial work was by Haun et al. [64] and Haun and Newnham [65] where the effective piezoelectric coefficients d_{33}^h , d_{31}^h were determined from the stress along axes x_1 and x_3 , respectively. Smith [10, 66] studied the hydrostatic response by assuming constant strain along the rods and constant stress in the x_1 - x_2 plane, and concluded the possibility to maximize electrical coupling in 1-3 piezocomposites if the Poisson ratio of the polymer passive phase is negative.

The polymer matrix facilitates transmitting of the external forces to act on ceramic rods when the composite plate is submitted to an incident hydrostatic pressure field. Therefore, in order to improve the performance of such piezocomposites, one way is to design microstructures of the matrix such that the stress arising from the external forces will produce an optimal piezoelectric response.

Sigmund et al. [67] integrated topology optimization to design the unit cells of the matrix, and the homogenized elastic tensors of optimized unit cells were used to calculate the effective piezoelectric properties. The homogenization approach for the 1-3 piezocomposite was developed by Gibiansky and Torquato [68]. In the works by Silva et al. [69, 70], a general homogenization framework for piezoelectric materials was developed using the finite element method and an optimal distribution of material and void phases in the unit cell was

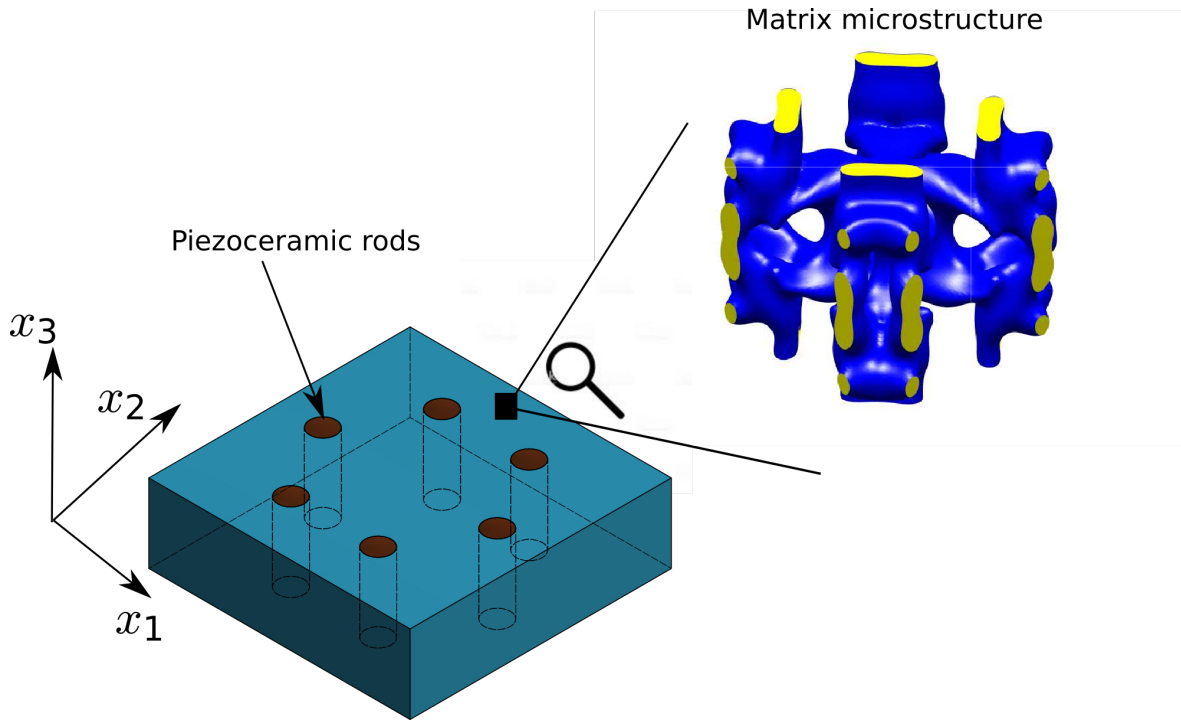


Figure 3.1: Class of the 1-3 piezoelectric composite.

found, that enhances performance of the piezocomposites. The two approaches were using the SIMP (solid isotropic material with penalization) method which is widely accepted in material and structural design [20, 71].

Recently, structural topology optimization with the level set function [6, 7, 51] was considered as an alternative approach to the SIMP method due to the flexible change in topology and shapes. In this approach, the boundaries between solid and void domains are represented by a zero level set of the level set function and the optimized geometry does not have the checker board problem and can be directly used for 3D printing.

We also aim to improve performance of the 1-3 piezoelectric by designing microstructures of the matrix phase. This approach is similar to the work in Sigmund et al. [67], even though we use topology optimization with the level set method instead of using SIMP, so that the optimized geometries are smooth and more suited to manufacturing. The effective piezoelectric coefficients and optimal volume fractions of piezoceramics are calculated by the DEM (differential effective medium) method [72]. This work is organized as follows: in Section 3.2, the calculation of effective moduli of the 1-3 piezocomposites is reviewed. The parameterized version of the level set method in topology optimization and sensitivity calculation are provided in Section 3.3. Next, Section 3.4 describes workflow for optimization process. Finally, Section 3.5 shows optimized results of 3D microstructures.

3.2 Constitutive Relation of The 1-3 Piezocomposite

The constitutive laws of piezoelectric media which describe the linear electromechanical interaction between the mechanical stress σ_{ij} , strain ε_{ij} , electric field E_i , and electric displacement D_i are given (in stress-charge form) by Mason and Baerwald [73] and Lerch [74]

$$\begin{aligned}\sigma_{ij} &= c_{ijkl}^E \varepsilon_{kl} - e_{kij} E_k \\ D_i &= e_{ijk} \varepsilon_{jk} + \epsilon_{ik}^S E_k,\end{aligned}\tag{3.1}$$

where c_{ijkl}^E is the elasticity modulus under short-circuit conditions, e_{ijk} is the piezoelectric coupling tensor, and ϵ_{ik}^S is the clamped permittivity. The small mechanical deformation is assumed.

The material tensors in (3.1) are spatially varying in composite media, and can be replaced with a homogeneous medium. For the composite structure consisting of piezoelectric ceramic rods immersed in a polymer matrix material as shown in Fig. 3.1, the following conditions are assumed:

1. The length scale of microstructures of the matrix phase is much smaller than the rod size.
2. There is perfect bonding between the rods and the polymer matrix.
3. The passive phase is a transversely isotropic material with axes aligned in the x_3 direction.
4. The distribution of the rods are random or hexagonal.

Avellaneda and Swart [72] introduced the effective moduli relevant for hydrostatic performance, which are calculated by

$$\begin{aligned}c_{13}^h &= c_{13}^m + fp(c_{13}^i + c_{13}^m) \\ e_{31}^h &= e_{31}^m + fp(e_{31}^i + e_{31}^m) \\ c_{33}^h &= c_{33}^m + f \left(1 + (p-1) \frac{(c_{13}^i - c_{13}^m)^2}{(\kappa^i - \kappa^m)(c_{33}^i - c_{33}^m)} \right) (c_{33}^i - c_{33}^m) \\ e_{33}^h &= e_{33}^m + f \left(1 + (p-1) \frac{(c_{13}^i - c_{13}^m)(e_{31}^i - e_{31}^m)}{(\kappa^i - \kappa^m)(e_{33}^i - e_{33}^m)} \right) (e_{33}^i - e_{33}^m) \\ \epsilon_{33}^h &= \epsilon_{33}^m + f \left(1 + (p-1) \frac{(e_{31}^i - e_{31}^m)^2}{(\kappa^i - \kappa^m)(\epsilon_{33}^i - \epsilon_{33}^m)} \right) (\epsilon_{33}^i - \epsilon_{33}^m)\end{aligned}\tag{3.2}$$

where f is the volume fraction of the piezoceramics, and p is a microscopic parameter defined as

$$p = \frac{1}{f} \frac{\kappa^h - \kappa^m}{\kappa^i - \kappa^m}.\tag{3.3}$$

The superscripts m and i denote the material parameters of the (polymer) matrix phase and the inclusion (ceramic rods) phase respectively. The traverse bulk and shear moduli of materials are

$$\kappa = \frac{1}{2}(c_{11} + c_{12}), \quad \mu = \frac{1}{2}(c_{11} - c_{12}). \quad (3.4)$$

If the large contrast stiffness between two phases is satisfied, i.e., ceramic rods are much stiffer than the polymer matrix (see also Avellaneda and Swart [72]), the differential effective medium (DEM) scheme [75–77] can predict the effective moduli of composites. When the volume fraction of one phase (ceramic rods) is incrementally added to the current configuration, the effective bulk and shear moduli of the composite plate are solutions of a system of ordinary differential equations

$$\begin{aligned} \frac{d\kappa^h}{df} &= \frac{1}{1-f}(\kappa^i - \kappa^h) \frac{\kappa^h + \mu^h}{\kappa^i + \mu^h} \\ \frac{d\mu^h}{df} &= \frac{1}{1-f}(\mu^i - \mu^h) \frac{2\mu^h(\kappa^h + \mu^h)}{(\kappa^i + \mu^h)\kappa^h + 2\mu^h\mu^i}. \end{aligned} \quad (3.5)$$

In this present work, we will focus on the design of hydrophone devices having optimal values of effective hydrostatic charge coefficient which is calculated by

$$d_h = [1 \quad 1] \cdot (\tilde{\mathbf{C}}^h)^{-1} \tilde{\mathbf{e}}^h \quad (3.6)$$

with

$$\tilde{\mathbf{C}}^h = \begin{bmatrix} \kappa^h & c_{13}^h \\ c_{13}^h & c_{33}^h \end{bmatrix}, \quad \tilde{\mathbf{e}}^h = \begin{bmatrix} e_{31}^h \\ e_{33}^h \end{bmatrix}. \quad (3.7)$$

A piezocomposite system with high values of d_h is more efficient in the forward problem, i.e., under mechanical forces more electrical signals are produced. Another quantity that also measures the material response is the figure of merit

$$d_h g_h = \frac{(d_h)^2}{(\epsilon_{33}^h + (\tilde{\mathbf{e}}^h)^T \cdot (\tilde{\mathbf{C}}^h)^{-1} \tilde{\mathbf{e}}^h)}. \quad (3.8)$$

We use d_h and $d_h g_h$ as the criteria to analyze the performance characteristics of the piezo-composite.

3.3 Materials Microstructure Topology Optimization by The Level Set Method

The concept of representing a domain geometry by a level set function is formulated as

$$\begin{cases} \phi(\mathbf{x}, \tau) > 0, & \mathbf{x} \in \Omega \text{ (solid)} \\ \phi(\mathbf{x}, \tau) < 0, & \mathbf{x} \notin \Omega \text{ (void)} \\ \phi(\mathbf{x}, \tau) = 0, & \mathbf{x} \in \partial\Omega \text{ (boundary)}, \end{cases} \quad (3.9)$$

in which the shape boundaries of the unit cell are represented by the zero value $\phi(\mathbf{x}, \tau) = 0$ as illustrated in Fig. 3.2. The dynamic evolution of the level set function is governed by the Hamilton–Jacobi (H-J) equation

$$\frac{\partial \phi}{\partial \tau} - V_n |\nabla \phi| = 0 \quad (3.10)$$

where

$$V_n = \frac{d\mathbf{x}}{d\tau} \cdot \frac{\nabla \phi}{|\nabla \phi|} \quad (3.11)$$

is the normal velocity component.

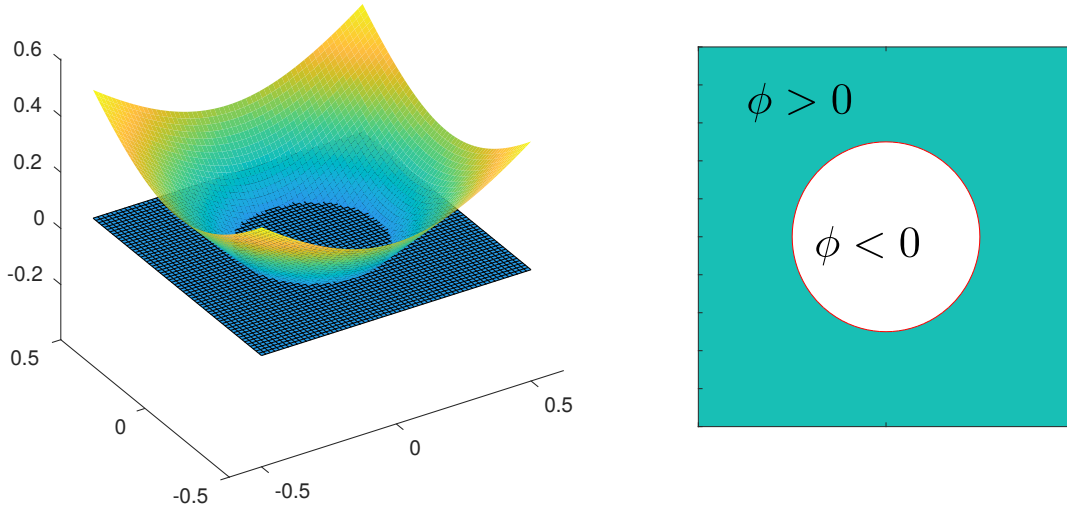


Figure 3.2: Level set function.

In optimization problems, V_n is chosen such that the gradient of the objective function is negative to ensure the objective function is minimized, e.g., using the steepest descent method, and new boundaries are obtained by solving (3.10) with a finite difference scheme [6, 52]. In this work, we utilize the parameterized version [25, 53] in which the level set function is approximated by a sum of radial basis functions $R_I(\mathbf{x})$ and associated expansion coefficients $\alpha_I(\tau)$:

$$\phi(\mathbf{x}, \tau) = \sum_I^N R_I(\mathbf{x}) \alpha_I(\tau) = \mathbf{R}(\mathbf{x}) \cdot \boldsymbol{\alpha}(\tau). \quad (3.12)$$

The H-J (3.10) is then written as a system of ordinary differential equations

$$\mathbf{R}^T \frac{d\boldsymbol{\alpha}}{d\tau} - V_n |(\nabla \mathbf{R})^T \boldsymbol{\alpha}| = 0 \quad \text{or} \quad V_n = \frac{\mathbf{R}^T \dot{\boldsymbol{\alpha}}}{|(\nabla \mathbf{R})^T \boldsymbol{\alpha}|}. \quad (3.13)$$

The radial basis functions with C^2 continuity are given by Wendland [78]

$$R_I(\mathbf{x}) = (\max\{0, (1 - r_I)\})^4 (4r_I + 1) \quad \text{and} \quad r_I = \frac{\|\mathbf{x} - \mathbf{x}_I\|}{r_0} \quad (3.14)$$

The supported radius r_0 is chosen to be 3 to 5 times of the mesh size in order to have sufficient knots in the neighborhood of any node \mathbf{x}_I . In the parameterized version, the expansion coefficients α_I are considered as design variables and are updated by a gradient-based mathematical programming optimizer, e.g., the method of moving asymptotes [59] is used in this present work.

We aim at designing the elastic properties of the matrix material such that the effective performance coefficients mentioned in Sec. (3.2) are improved. For materials which have a periodic arrangement of microstructures in some given directions, the material properties are modeled as a homogeneous medium as long as the size of the microstructures is much smaller than the operating wavelength. The elastic tensor \mathbb{C}^m is obtained according to the homogenization theory in which the two following conditions are satisfied: (1) periodic arrangement of unit cells, and (2) separated length scales between the macroscopic and unit cells. Components of the homogenized elastic tensor are average of mutual strain energy over the unit cell [20, 50]

$$C_{ijkl}^m = \int_Y \left(\varepsilon_{pq}^{0,ij} - \varepsilon_{pq}(\boldsymbol{\chi}^{ij}) \right) C_{pqrs} \left(\varepsilon_{rs}^{0,kl} - \varepsilon_{rs}(\boldsymbol{\chi}^{kl}) \right) \mathcal{H}(\phi) d\Omega \quad (3.15)$$

where the strain field $\boldsymbol{\varepsilon}(\boldsymbol{\chi}^{kl})$ is the solution to:

$$\int_Y \left(\varepsilon_{pq}^{0,ij} - \varepsilon_{pq}(\boldsymbol{\chi}^{ij}) \right) C_{pqrs} \varepsilon_{rs}(\mathbf{v}^{ij}) \mathcal{H}(\phi) d\Omega = 0, \quad \forall \mathbf{v} \in V_0^h. \quad (3.16)$$

We solve the system (3.16) on a cubic unit cell with six independent test-strain cases $\boldsymbol{\varepsilon}^{0,ij}$ ($ij = 11, 22, 33, 23, 13, 12$) and periodic boundary conditions are applied on the opposite faces.

For sensitivity calculation, a general Lagrange function for a component of the effective elastic tensor C_{ijkl}^m is formulated as

$$J(\boldsymbol{\chi}, \mathbf{v}, \phi) = g(\boldsymbol{\chi}, \phi) + a(\boldsymbol{\chi}, \mathbf{v}, \phi) - l(\mathbf{v}, \phi) \quad (3.17)$$

with

$$\begin{aligned} g(\boldsymbol{\chi}, \phi) &= \int_Y \left(\varepsilon_{pq}^{0,ij} - \varepsilon_{pq}(\boldsymbol{\chi}^{ij}) \right) C_{pqrs} \left(\varepsilon_{rs}^{0,kl} - \varepsilon_{rs}(\boldsymbol{\chi}^{kl}) \right) \mathcal{H}(\phi) d\Omega \\ a(\boldsymbol{\chi}, \mathbf{v}, \phi) &= \int_Y \varepsilon_{pq}(\boldsymbol{\chi}^{ij}) C_{pqrs} \mathcal{H}(\phi) \varepsilon_{rs}(\mathbf{v}) d\Omega \\ l(\mathbf{v}, \phi) &= \int_Y \varepsilon_{pq}^{0,ij} C_{pqrs} \mathcal{H}(\phi) \varepsilon_{rs}(\mathbf{v}) d\Omega. \end{aligned} \quad (3.18)$$

We use shape derivatives of the Lagrange function (by Choi and Kim [58]) such that

$$\dot{J} = g(\dot{\boldsymbol{\chi}}, \phi) + g(\boldsymbol{\chi}, \dot{\phi}) + a(\dot{\boldsymbol{\chi}}, \mathbf{v}, \phi) + a(\boldsymbol{\chi}, \dot{\mathbf{v}}, \phi) + a(\boldsymbol{\chi}, \mathbf{v}, \dot{\phi}) - l(\dot{\mathbf{v}}, \phi) - l(\mathbf{v}, \dot{\phi}) \quad (3.19)$$

with

$$\begin{aligned}
 g(\dot{\boldsymbol{\chi}}, \phi) &= \int_Y -2\varepsilon_{pq}(\dot{\boldsymbol{\chi}}^{ij}) C_{pqrs} \mathcal{H}(\phi(\mathbf{y})) \left(\varepsilon_{rs}^{0,kl} - \varepsilon_{rs}(\boldsymbol{\chi}^{kl}) \right) d\Omega \\
 g(\boldsymbol{\chi}, \dot{\phi}) &= \int_Y \left(\varepsilon_{pq}^{0,ij} - \varepsilon_{pq}(\boldsymbol{\chi}^{ij}) \right) C_{pqrs} \left(\varepsilon_{rs}^{0,kl} - \varepsilon_{rs}(\boldsymbol{\chi}^{kl}) \right) \delta(\phi(\mathbf{y})) |\nabla\phi| V_n d\Omega \\
 a(\boldsymbol{\chi}, \mathbf{v}, \dot{\phi}) &= \int_Y \varepsilon_{pq}(\boldsymbol{\chi}^{ij}) C_{pqrs} \varepsilon_{rs}(\mathbf{v}) \delta(\phi) |\nabla\phi| V_n d\Omega \\
 a(\dot{\boldsymbol{\chi}}, \mathbf{v}, \phi) &= \int_Y \varepsilon_{pq}(\dot{\boldsymbol{\chi}}^{ij}) C_{pqrs} \varepsilon_{rs}(\mathbf{v}) \mathcal{H}(\phi(\mathbf{y})) d\Omega \\
 a(\boldsymbol{\chi}, \dot{\mathbf{v}}, \phi) &= \int_Y \varepsilon_{pq}(\boldsymbol{\chi}^{ij}) C_{pqrs} \varepsilon_{rs}(\dot{\mathbf{v}}) \mathcal{H}(\phi(\mathbf{y})) d\Omega \\
 l(\mathbf{v}, \dot{\phi}) &= \int_Y \varepsilon_{pq}^0 C_{pqrs} \varepsilon_{rs}(\mathbf{v}) \delta(\phi) |\nabla\phi| V_n d\Omega. \\
 l(\dot{\mathbf{v}}, \phi) &= \int_Y \varepsilon_{pq}^0 C_{pqrs} \mathcal{H}(\phi(\mathbf{y})) \varepsilon_{rs}(\dot{\mathbf{v}}) d\Omega.
 \end{aligned} \tag{3.20}$$

All the terms containing $\dot{\mathbf{v}}$ can be eliminated since the following relations hold true

$$a(\boldsymbol{\chi}, \dot{\mathbf{v}}, \phi) - l(\dot{\mathbf{v}}, \phi) = 0, \quad \forall \dot{\mathbf{v}} \in V_0^h. \tag{3.21}$$

The time derivative of the characteristic displacement $\dot{\boldsymbol{\chi}}$ in (3.19) is eliminated by forming the following adjoint equation which should be solved for \mathbf{v} in general

$$g(\dot{\boldsymbol{\chi}}, \phi) + a(\dot{\boldsymbol{\chi}}, \mathbf{v}, \phi) = 0 \tag{3.22}$$

or

$$\begin{aligned}
 & \int_Y \varepsilon_{pq}(\dot{\boldsymbol{\chi}}^{ij}) C_{pqrs} \mathcal{H}(\phi(\mathbf{y})) \varepsilon_{rs}(\mathbf{v}) d\Omega \\
 &= 2 \int_Y \varepsilon_{pq}(\dot{\boldsymbol{\chi}}^{ij}) C_{pqrs} \mathcal{H}(\phi(\mathbf{y})) \left(\varepsilon_{rs}^{0,kl} - \varepsilon_{rs}(\boldsymbol{\chi}^{kl}) \right) d\Omega.
 \end{aligned} \tag{3.23}$$

In fact the Eq. (3.23) is a self-adjoint problem and by properly choosing the function space \mathbf{v} such that

$$\varepsilon_{rs}(\mathbf{v}) = 2 \left(\varepsilon_{rs}^{0,kl} - \varepsilon_{rs}(\boldsymbol{\chi}^{kl}) \right), \tag{3.24}$$

the Eq. (3.23) is satisfied. By Comparing (3.19) and (3.23), the time derivative of the effective elasticity tensor is

$$\frac{\partial C_{ijkl}^m}{\partial \tau} = - \int_Y \left(\varepsilon_{pq}^{0,ij} - \varepsilon_{pq}(\boldsymbol{\chi}^{ij}) \right) C_{pqrs} \left(\varepsilon_{rs}^{0,kl} - \varepsilon_{rs}(\boldsymbol{\chi}^{kl}) \right) \delta(\phi) |\nabla \phi| V_n d\Omega \quad (3.25)$$

It can be written in terms of parameterized level set function (3.13) as

$$\frac{\partial C_{ijkl}^m}{\partial \tau} = - \sum_{I=1}^N \left(\int_Y \left(\varepsilon_{pq}^{0,ij} - \varepsilon_{pq}(\boldsymbol{\chi}^{ij}) \right) C_{pqrs}(\phi) \left(\varepsilon_{rs}^{0,kl} - \varepsilon_{rs}(\boldsymbol{\chi}^{kl}) \right) R_I(\mathbf{x}) d\Omega \right) \cdot \dot{\alpha}_I. \quad (3.26)$$

Furthermore, the time derivative of effective the elasticity tensor can be obtained by applying the chain rule

$$\frac{\partial C_{ijkl}^m}{\partial \tau} = \sum_{I=1}^N \frac{\partial C_{ijkl}^m}{\partial \alpha_I} \frac{\partial \alpha_I}{\partial \tau}. \quad (3.27)$$

By comparing (3.27) and (3.26), the sensitivity analysis of the effective elasticity tensor with respect to the design variable α^I is

$$\frac{\partial C_{ijkl}^m}{\partial \alpha_I} = - \int_Y \left(\varepsilon_{pq}^{0,ij} - \varepsilon_{pq}(\boldsymbol{\chi}^{ij}) \right) C_{pqrs} \left(\varepsilon_{rs}^{0,kl} - \varepsilon_{rs}(\boldsymbol{\chi}^{kl}) \right) \delta(\phi) R_I(\mathbf{x}) d\Omega \quad (3.28)$$

Similarly, the sensitivity analysis of the volume constraint is given as

$$\frac{\partial V}{\partial \alpha_I} = \int_Y \delta(\phi) R_I(\mathbf{x}) d\Omega. \quad (3.29)$$

In the above, the Heaviside function is numerically regularized

$$\mathcal{H}(\phi) = \begin{cases} \xi & \phi < \Delta \\ \frac{3}{4} \left(\frac{\phi}{\Delta} - \frac{\phi^3}{3\Delta^3} \right) + \frac{1}{2} & -\Delta \leq \phi \leq \Delta \\ 1 & \phi > \Delta \end{cases} \quad (3.30)$$

in which $\delta(\phi) = \mathcal{H}'(\phi)$, Δ is the width of numerical approximation, and ξ is a small positive number chosen to avoid numerical instability problems.

3.4 Optimization Algorithm

In this section, we outline the design procedure for microstructures of the passive phase (matrix) by using topology optimization. The aim is to maximize the hydrostatic charge coefficient d_h ; the corresponding optimization problem is:

$$\begin{aligned} & \text{maximize} && d_h \\ & \text{s.t.} && \begin{cases} a(\mathbf{u}, \mathbf{v}, \phi) = l(\mathbf{v}, \phi) & \text{(equilibrium equation)} \\ V(\phi) = \int_Y \mathcal{H}(\phi) d\Omega \leq v_f & \text{(volume constraint)} \\ \alpha_{\min} \leq \alpha_i \leq \alpha_{\max} & (i = 1, 2, \dots, N) \end{cases} \end{aligned} \quad (3.31)$$

The following steps describe the optimization procedure:

1. Set the initial configuration of the unit cell generated with level set values.
2. Calculate effective moduli C_{ijkl}^m of the matrix phase by using the homogenization method (3.15). Compute effective bulk and shear moduli κ^m, μ^m .
3. Solve the ODEs in (3.5) by a numerical integration scheme with step sizes $\Delta f = 0.005$ and $f \in [0, 1]$. The initial values of bulk modulus $\kappa^h = \kappa^m$ and shear modulus $\mu^h = \mu^m$ are chosen at volume fraction $f = 0$.
4. Determine the microscopic parameter p from (3.3).
5. Find the effective moduli (3.2) and hydrostatic charge coefficient (3.6). Then, determine the maximize value of d_h^{\max} and the corresponding volume fraction f^{\max} .
6. Perform sensitivity analysis of d_h and update the design variables α_I by MMA.
7. Repeat from step 2 until convergence.

The sensitivity calculation of hydrostatic charge coefficient $\partial d_h / \partial \alpha_I$ requires the sensitivities $\partial C_{ijkl}^m / \partial \alpha_I$ which are derived in Section 3.3.

3.5 Results

Results of hydrostatic charge coefficients predicted by DEM scheme are plotted in Fig. 3.3 for the 1-3 piezocomposite consisting of PZT5A rods embedded in a Stycast matrix. The material properties are listed in Table 3.1. For the hydrostatic application, the induced dielectric displacement is given by

$$D_3 = d_h T \quad (3.32)$$

where T is the hydrostatic pressure magnitude. Therefore, a large value of d_h is desired to maximize efficiency of hydrophone devices. If the ceramic rods are poled in the x_3 -direction, the hydrostatic charge coefficient d_h is also defined as

$$d_h = 2d_{31} + d_{33}. \quad (3.33)$$

As values d_{31} have opposite signs with d_{33} , the impact on d_h is small when compared to d_{33} as shown in Fig. 3.3 (a). We next assume the polymer matrix is isotropic with Young's modulus $E = 9.22 (10^9 N/m^2)$ and we plot the evolution of d_h for different values of Poisson's ratio $\nu^m \in [-0.5, 0.4]$ in Fig. 3.3 (b). The hypothetical effects of Poisson's ratio are significant. If the polymer matrix has negative Poisson's ratio, a compressive stress in x_1 - x_2 plane is converted into a vertical compressive stress bearing on the ceramic rods, which generates the positive values of d_{31} . The enhancement of d_h by negative Poisson's ratio was predicted by Smith [10].

The optimization algorithm in Section 3.4 is applied to find material microstructures of the matrix phase. We use a cubic domain discretized with 50^3 bilinear elements. The geometries are represented by level set functions and the knots coincide with the finite element nodes. Solid parts of unit cells are constituted by Stycast, and the void domains are filled with a pseudo material which is (10^6 times) softer to avoid singularity. The calculation of effective moduli mentioned in Section 3.2 requires the polymer matrix is transversely isotropic. An

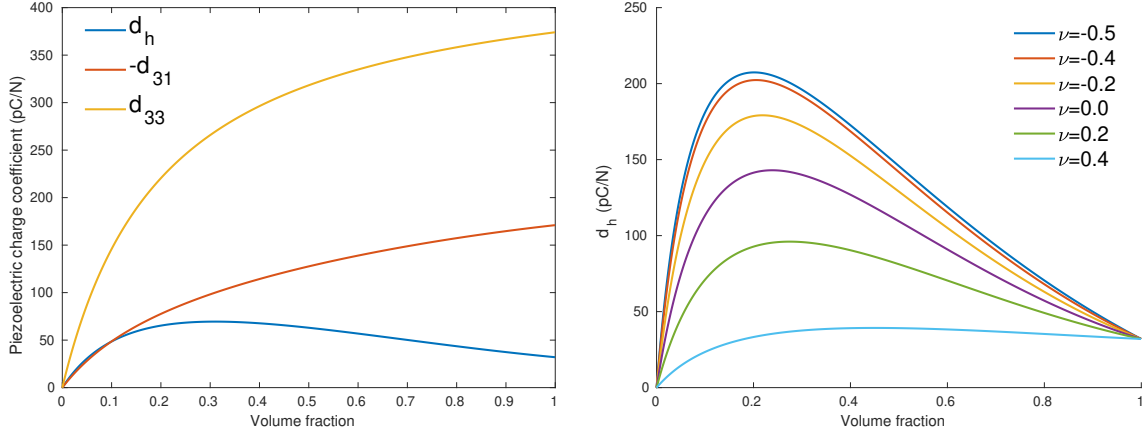


Figure 3.3: Effective hydrostatic charge coefficient of the 1-3 piezocomposite (a). Enhancement of d_h due to Poisson's ratio (b).

Material	PZT5A	Stycast
c_{11}^E ($10^9 N/m^2$)	120.34	12.3
c_{12}^E ($10^9 N/m^2$)	75.17	5.2
c_{13}^E ($10^9 N/m^2$)	75.09	5.2
c_{33}^E ($10^9 N/m^2$)	110.86	12.3
e_{31} (C/m^2)	-5.35	0
e_{33} (C/m^2)	15.7835	0
$\epsilon_{33}^S/\epsilon_0$	826.6	4

Table 3.1: Material parameters.

additional constraint for the isotropy in the x_1 - x_2 plane is added to the optimization problem (3.31).

$$\frac{(c_{11}^m - c_{22}^m)^2 + (c_{31}^m - c_{32}^m)^2}{(\kappa^m)^2} \leq tol. \quad (3.34)$$

Optimized microstructures are shown Table 3.2 with corresponding elastic properties. The elastic properties show negative Poisson's ratio in the planes x_3 - x_1 and x_3 - x_2 as predicted. As the unit cells are cubic domains, we only obtain microstructures which meet the transverse isotropy constraint with an acceptable tolerance. Since the size of microstructures is smaller than the rod diameter, the transverse isotropic condition in the matrix phase is preserved and the calculation method (3.2) for effective moduli of the 1-3 piezocomposite is applicable.

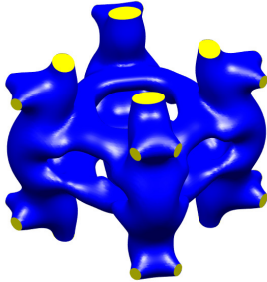
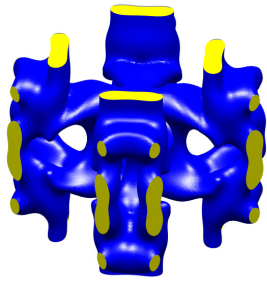
Optimized unit cells	Effective elastic properties (GPa)
<p>(a)</p> 	$\mathbf{C}^m = \begin{bmatrix} 0.304 & 0.065 & -0.166 & 0 & 0 & 0 \\ 0.065 & 0.295 & -0.170 & 0 & 0 & 0 \\ -0.166 & -0.170 & 0.653 & 0 & 0 & 0 \\ 0 & 0 & 0 & 0.06 & 0 & 0 \\ 0 & 0 & 0 & 0 & 0.06 & 0 \\ 0 & 0 & 0 & 0 & 0 & 0.07 \end{bmatrix}$ <p>$V_f = 0.3$</p>
<p>(b)</p> 	$\mathbf{C}^m = \begin{bmatrix} 0.29 & 0.20 & -0.09 & 0 & 0 & 0 \\ 0.02 & 0.30 & -0.08 & 0 & 0 & 0 \\ -0.09 & -0.08 & 0.73 & 0 & 0 & 0 \\ 0 & 0 & 0 & 0.06 & 0 & 0 \\ 0 & 0 & 0 & 0 & 0.06 & 0 \\ 0 & 0 & 0 & 0 & 0 & 0.17 \end{bmatrix}$ <p>$V_f = 0.3$</p>

Table 3.2: Designs of microstructures of the polymer matrix.

Fig. 3.4 plots the enhancement of d_h for the 3D microstructures. Positive values d_{31} occur when the volume fraction $f \leq 0.2$, and the improvements are observed with larger magnitudes of d_h at the volume fraction $f \approx 0.1$. The figures of merit $d_h g_h$ are also possibly improved with the designs. These are in contrast to conventional material with positive Poisson's ratio (Stycast, Fig. 3.3 (a)).

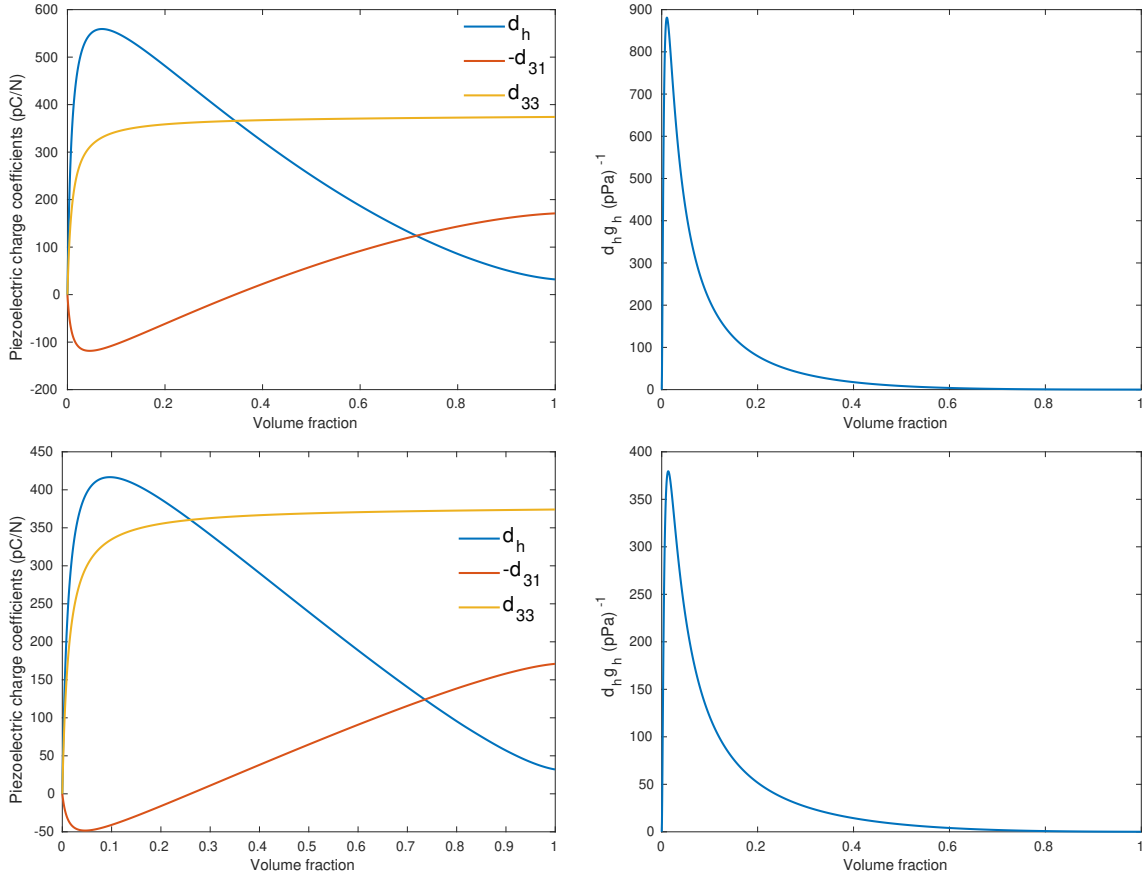


Figure 3.4: Effective hydrostatic charge and electrical voltage coefficients of the 1-3 piezocomposite. Top and bottom with the designs (a) and (b) in Table 3.2, respectively.

3.6 Conclusion

We used topology optimization with the level set method to optimize microstructures of the polymer matrix such that the performance of the 1-3 piezoelectric composite is enhanced. The optimized microstructures exhibit negative Poisson's ratio which allows the electric charge coefficient d_{31} to be positive when compared to the conventional polymer material, and an enhancement is obtained on the effective hydrostatic charge coefficients d_h .

The unit cell configuration was represented by the level set function which enables to distinguish boundaries between void and solid domain. This way, there is no checker board problem occurring and the prototype can be printed directly with a 3D printer. We used unit cells defined in a cubic domain, and an additional isotropic constraint in the x_1 - x_2 plane was added to the optimization problem. These constraint can influence the optimized results due to the limitation of design spaces. Unit cells with hexagonal cross-section could be an alternative approach in some future works.

Chapter 4

Inverse Design of Topological Phononic Plates

4.1 Introduction

Quantum Spin Hall effect (QSHE) [79, 80] is a topological state widely mimicked to get backscattering immune interface propagation of acoustic and elastic waves. Quantum Hall effect (QHE) [81] requires breaking of time reversal symmetry by an external magnetic field to restrict the electrons along the boundary of a semi-conductor. Though QHE based phononic Topological Insulators (TIs) with active components are proposed [82, 83], passive phononic periodic structures with lossless localized interface propagation are robust. In an electronic system, QSHE circumvents the necessity of an external magnetic field by utilizing Spin orbit coupling (SOC) common among heavy elements like Hg and Te [84]. The experiments [85] that demonstrated SOC in quantum wells showed the role of band inversion between valence and conduction bands in designing TIs. QSHE based TIs have helical edge states in which each edge has electrons in spin up or spin down state travelling in opposite directions. The backscattering is thereby suppressed as the electron has to change spin in order to backscatter.

Breaking T -symmetry in the QH system, by introducing the external magnetic field, lifts the degeneracy and offers conducting edge states at the boundary due to change in topological invariants. The chiral edge state enables spin-up electrons to propagate in only one direction and the anti-chiral edge state allows spin-down electrons to propagate in only the direction opposite to spin-up electrons. Mechanism of quantum spin hall effect can be described by two copies of quantum hall systems (Fig. 4.1a), the helical edge state possesses two spins propagating in opposite directions. The time reversal symmetry (TRS) in QSHE is preserved in the system. The intrinsic spin-orbit coupling (SOC) replaces external magnetic field in QSHE.

In spin 1/2 system, time-reversal (Θ) symmetry leads to $E_s(\mathbf{k}) = E_{-s}(-\mathbf{k})$, $\mathbf{k} \rightarrow -\mathbf{k}$ and $s \rightarrow -s$, where s denotes spin up (\uparrow) or down (\downarrow). Considering \mathcal{H} as the system Hamiltonian and $H(\mathbf{k}) = e^{-i\mathbf{k}\cdot\mathbf{x}}\mathcal{H}e^{i\mathbf{k}\cdot\mathbf{x}}$ as the canonical Bloch Hamiltonian, the time-reversal operator for spin 1/2 system is $\Theta = i\sigma_y\kappa$, where σ_y is a Pauli matrix, κ is complex conjugate operator. The system possesses time-reversal symmetry if $[\Theta, \mathcal{H}] = 0$, and $\Theta H(\mathbf{k})\Theta^{-1} = H(-\mathbf{k})$. Therefore, the eigenstates at \mathbf{k} and $-\mathbf{k}$ must have equal eigen energy. On the other hand, for crystals with space inversion symmetry (SIS), $E_s(\mathbf{k}) = E_s(-\mathbf{k})$ since SIS results only in $\mathbf{k} \rightarrow -\mathbf{k}$. Therefore, band structure due to both time-reversal and space inversion symmetry

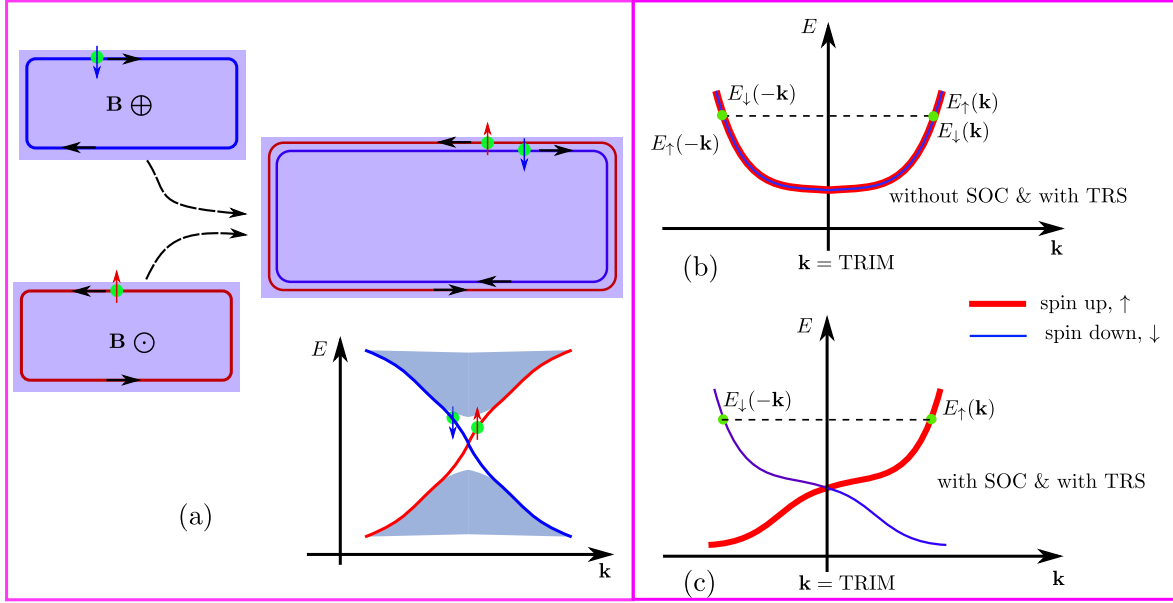


Figure 4.1: Illustration of spin dependent edge states in a quantum spin Hall system.

has global double degeneracy $E_s(\mathbf{k}) = E_{-s}(\mathbf{k})$ (Fig. 4.1b). The presence of spin-orbit coupling, equivalent to breaking inversion symmetry, results in spin-splitting effect. However, there is a degeneracy at the time-reversal invariant momenta (TRIM), where \mathbf{k} is equivalent to $-\mathbf{k}$ due to periodicity of the Brillouin zone (Fig. 4.1c). The edge states in such half-integer spin systems are protected by T -symmetry and the two states form a pair with the same energy but opposite spins, i.e, Kramers' pairs.

Half-integer spin particles (fermions) with time-reversal operator $\Theta_f^2 = -1$, guarantees existence of Kramers' degeneracy and the gapless helical edge state with opposite spins. Meanwhile, elastic waves do not possess the attribute of intrinsic spin, and are bosonic with $\Theta_b^2 = +1$. In order to emulate QSHE in a classical wave system without intrinsic spin, the concept of pseudo TR operator (Θ_p) with attributes similar to fermions, $\Theta_p^2 = -1$ is adopted. The pseudo TR is constructed with pseudo-spins, from two-dimensional irreducible representation of the C_6 symmetry group [86] E' and E'' with corresponding basis (x, y) and $(x^2 - y^2, xy)$ respectively. The basis functions have symmetries similar to (p_x, p_y) and $(d_{x^2-y^2}, d_{xy})$ orbitals.

Several elastic/acoustic wave analogues to QSHE based TIs are proposed in literature [87–91]. While most of the elastic wave analogues are restricted to scalar wave propagation, Mousavi et al. [16] and Yu et al. [92] designed phononic plate TIs. In case of Mousavi's work [16], the Dirac cone in anti-symmetric mode band structure is matched with the Dirac cone in symmetric mode band structure to form a double Dirac cone, and hybridization of symmetric and anti-symmetric Lamb modes in the elastic plate is used as the basis to construct pseudospins. By changing the material distribution along the thickness direction the topological band gap is opened with degenerate bands being mixed modes. While in Yu et al. [92], the pseudospin pair is constructed by mixing the p - and d -like modes at the double Dirac cone. The in-plane symmetric modes are not considered as the periodic plate structure

has in-plane dimension several orders higher than its thickness. The out-of-plane excitation though causes in-plane displacements, they are several orders of magnitude lesser compared to anti-symmetric mode displacements and do not affect the topologically protected wave propagation along the interface. Consequently, the symmetry breaking is done in Yu et al. [92] just by modifying the in-plane topology while the through thickness material remains unaltered.

The unit cell topologies are designed in the above discussed works either by trial and error or by intuition. Several papers later proposed systematic design procedure to obtain topologically distinct unit cell topologies. In Nanthakumar et al. [93], the unit cell is designed such that a double Dirac cone emerges due to zone folding. The topology with double Dirac cone is engineered such that topology A and B are obtained. The disadvantage in this method is that due to different volume fractions of topologies A and B, the bulk band gap of the topologies do not match though there exists an overlap. In Christiansen et al. [94] a top down approach is adopted to design unit cell topologies. The objective function is formulated based on the propagation through two intersecting interfaces in a periodic structure, which is relatively time consuming. The existence of QSHE is later proved by plotting the supercell band structure. In Dong et al. [95], the LDOS based optimization scheme is adopted to design acoustic crystals for spin dependent propagation. The topology can have disconnected components as it is for an acoustic wave propagation. In Lu and Park [96], SIMP is adopted to design square unit cells for scalar wave propagation, the objective function is based on the modal assurance criterion.

Hereby, we developed two different methods to inverse design phononic plate TIs. We directly obtain two opposite unit cells with mode inversion, which means that, spin-orbit coupling is directly introduced to the overall system. Although the global double degeneracy opens into a gap, the TRIM has intersecting bands. In Method I, the objective function is formulated based on dispersion equation. In Method II, the objective function is formulated based on equilibrium equation with periodic displacement boundary conditions. Genetic algorithm is the optimization method adopted. In addition to designing phononic plate TIs, we also have stepped forward to realise a possible application of the elastic wave TI. A phononic crystal with bulk band gap can stop an incoming wave over a range of frequency and may be useful in protecting damaged parts of a structure. While, in case of applications where the wave needs to be transmitted around a defect, elastic wave TIs are handy as proved in this manuscript.

4.2 Lattice Symmetry, Brillouin Zones and Band Structures

Phononic crystals consist of periodically distributed motifs, i.e., identical unit cells, in spatial directions. Unit cell positions are determined by vectors

$$\mathbf{R}_m = n_1 \mathbf{a}_1 + n_2 \mathbf{a}_2 + n_3 \mathbf{a}_3, \quad m, n_i \in \mathbb{Z}, \quad (4.1)$$

where \mathbf{a}_i are the primitive vectors and n_i are integers indicating the location within the lattice structure. For any position-dependent function $f(\mathbf{r})$ is periodic on the lattice, e.g, density or elastic modulus, it can be written as Fourier series

$$f(\mathbf{r}) = \sum_m f_m e^{i\mathbf{G}_m \cdot \mathbf{r}}, \quad (4.2)$$

where the index $m = (n_1, n_2, n_3)$ and \mathbf{G}_m are translation vectors in the reciprocal space. Due to periodicity, the function values are identical for any translation:

$$f(\mathbf{r}) = f(\mathbf{r} + \mathbf{R}_n), \quad (4.3)$$

or expressed in terms of Fourier series

$$\sum_m f_m e^{i\mathbf{G}_m \cdot \mathbf{r}} = \sum_m f_m e^{i\mathbf{G}_m \cdot (\mathbf{r} + \mathbf{R}_n)} = \sum_m f_m e^{i\mathbf{G}_m \cdot \mathbf{R}_n} e^{i\mathbf{G}_m \cdot \mathbf{r}}. \quad (4.4)$$

In other words, lattices in the reciprocal space can be described by a set of vectors \mathbf{G}_m that satisfy

$$e^{i\mathbf{G}_m \cdot \mathbf{R}_n} = 1, \quad (4.5)$$

and corresponding primitive vectors \mathbf{b}_j in the reciprocal space are defined from the relations

$$\mathbf{b}_j \cdot \mathbf{a}_i = 2\pi\delta_{ji}, \quad (4.6)$$

which is used to define translation vectors in the reciprocal space:

$$\mathbf{G}_m = n_1\mathbf{b}_1 + n_2\mathbf{b}_2 + n_3\mathbf{b}_3, \quad m, n_i \in \mathbb{Z}. \quad (4.7)$$

The reciprocity of unit cell in its reciprocal space is also called the first Brillouin zone, and the reciprocal space is also periodic. Thus, the analysis of band structure in the 1st Brillouin zone is enough. Furthermore, phononic crystals are characterized by their primitive vectors \mathbf{a}_i and possess symmetric properties such as translation, rotation and reflection, the band structure calculation obtained from wave vectors in the irreducible Brillouin zone are sufficient to understand wave behaviors. Figure 4.2 illustrates an example of hexagonal primitive cell in 2D with its primitive vectors and the corresponding Brillouin zone. For a symmetry type C_{6v} as shown in Fig. 4.2c, band structures are calculated along Γ - K - M , and for C_6 rotation symmetry (Fig. 4.2d), the analysis need to perform along Γ - K - K' - Γ - M .

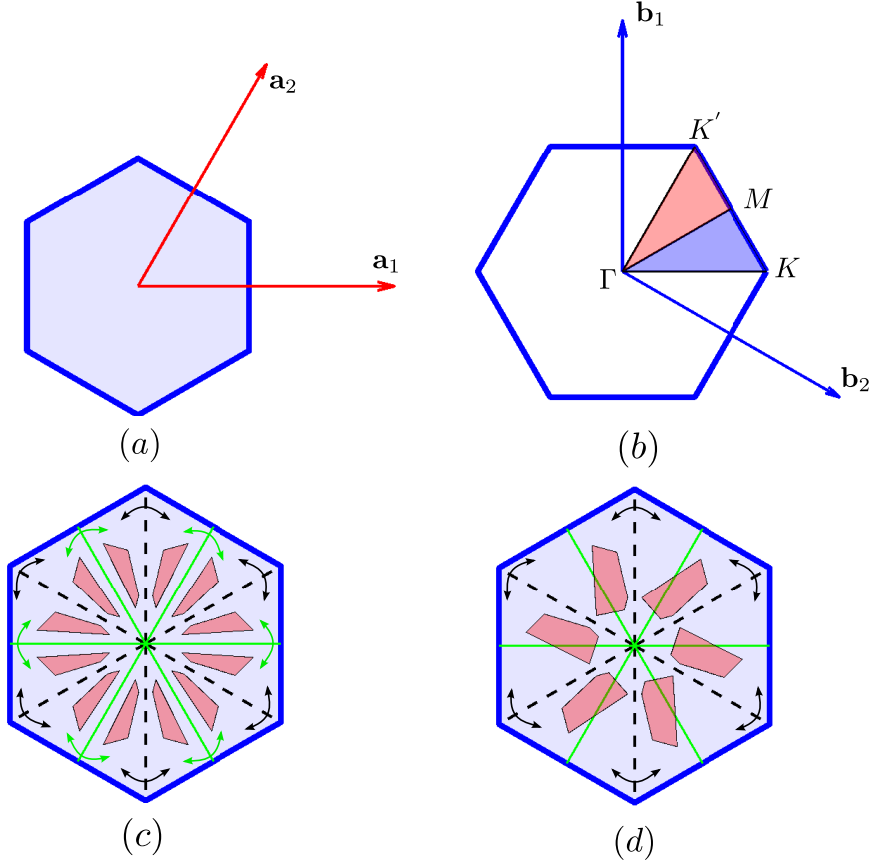


Figure 4.2: Hexagonal primitive unit cell (a) and its Brillouin zone (b). Examples of unit cell with C_{6v} -symmetry (c) and C_6 -rotational symmetry (d).

Band structure calculation can help to realize and predict elastic wave behaviors in phononic crystals. The most important information shown in the band structure is the band gap. The band gap describes frequency ranges in which waves can not propagate. Waves traveling in phononic crystals may reflect off of boundaries and interfaces destructively, and result on waves decay in space. In following, we present finite element procedure for calculating band structures of phononic crystals. For an elastic medium, the governing equation without external force

$$\sigma_{ij,i} = \rho \ddot{u}_j, \quad (4.8)$$

where ρ is the density, and the stress component σ_{ij} is calculated by

$$\sigma_{ij} = C_{ijkl} \varepsilon_{kl} = \frac{1}{2} C_{ijkl} (u_{kl} + u_{lk}). \quad (4.9)$$

The strong form is converted to the weak formulation by using the variational principles:

$$\int_{\Omega} C_{ijkl} \varepsilon_{ij}(\mathbf{u}) \varepsilon_{kl}(\delta \mathbf{u}) d\Omega = - \int_{\Omega} \rho \frac{\partial^2 u_i}{\partial t^2} \delta u_i d\Omega. \quad (4.10)$$

For the periodic phononic crystals, the displacement field u_j have the form:

$$u_j(\mathbf{x}, \mathbf{k}, t) = \tilde{u}_j(\mathbf{x}, t) e^{i\mathbf{k} \cdot \mathbf{x}}, \quad (4.11)$$

and

$$u_{i,j}(\mathbf{x}, \mathbf{k}, t) = (\tilde{u}_i(\mathbf{x}, t) ik_j + \tilde{u}_{i,j}(\mathbf{x}, t)) e^{i\mathbf{k}\cdot\mathbf{x}}. \quad (4.12)$$

The finite element method is implemented by discretizing the continuum variable \tilde{u}_j with

$$\tilde{u}_j(\mathbf{x}, t) = \sum_I R^I(\mathbf{x}) \bar{u}_j^I(t), \quad (4.13)$$

where $R^I(\mathbf{x})$ are finite element shape functions and \bar{u}_j^I are nodal values. Substituting the Bloch solution (4.13) in to the weak formulation (4.10), we obtain a system of equations:

$$\delta \bar{\mathbf{u}}^T \underbrace{\left(\int_{\Omega} (\mathcal{L} \mathbf{R})^T \mathbf{C} (\mathcal{L} \mathbf{R}) d\Omega \right)}_{\mathbf{K}(\mathbf{k})} \bar{\mathbf{u}} = -\delta \bar{\mathbf{u}}^T \underbrace{\left(\int_{\Omega} \rho \mathbf{R}^T \mathbf{R} d\Omega \right)}_{\mathbf{M}} \ddot{\bar{\mathbf{u}}}, \quad (4.14)$$

where \mathcal{L} is a gradient operator in matrix form:

$$\mathcal{L} = \begin{bmatrix} \frac{\partial}{\partial x} + ik_x & 0 & 0 \\ 0 & \frac{\partial}{\partial y} + ik_y & 0 \\ 0 & 0 & \frac{\partial}{\partial z} + ik_z \\ 0 & \frac{\partial}{\partial z} + ik_z & \frac{\partial}{\partial y} + ik_y \\ \frac{\partial}{\partial z} + ik_z & 0 & \frac{\partial}{\partial x} + ik_x \\ \frac{\partial}{\partial y} + ik_y & \frac{\partial}{\partial x} + ik_x & 0 \end{bmatrix}, \quad \mathbf{R} = \begin{bmatrix} R^1 & 0 & 0 & \cdots & R^N & 0 & 0 \\ 0 & R^1 & 0 & \cdots & 0 & R^N & 0 \\ 0 & 0 & R^1 & \cdots & 0 & 0 & R^N \end{bmatrix} \quad (4.15)$$

The final discrete system of equations is

$$\mathbf{K}(\mathbf{k}) \bar{\mathbf{u}} + \mathbf{M} \ddot{\bar{\mathbf{u}}} = \mathbf{0}. \quad (4.16)$$

If a time-harmonic solution $\bar{\mathbf{u}} = \hat{\mathbf{u}} e^{-i\omega t}$ is assumed, we can obtain the characteristic equation

$$\left(\mathbf{K}(\mathbf{k}) - \omega^2 \mathbf{M} \right) \mathbf{u} = \mathbf{0}, \quad (4.17)$$

where the over hat in $\hat{\mathbf{u}}$ is eliminated for simplicity. For each value of wave vector \mathbf{k} , we can obtain eigenfrequencies and associated eigenvectors by solving the eigenequation (4.17), which is the first order eigenproblem with respect to ω^2 . The scheme consider frequency as a function of wave vector, i.e, $\omega(\mathbf{k})$ method.

Alternatively, we can also consider wave vectors as a function of frequency, i.e, $\mathbf{k}(\omega)$, then for each value of frequency ω the wave vector can be determined by re-writing the wave vector as:

$$\mathbf{k} = k\boldsymbol{\alpha} + \mathbf{d}_0 = k \begin{bmatrix} \alpha_x \\ \alpha_y \\ \alpha_z \end{bmatrix} + \mathbf{d}_0, \quad \text{and} \quad \sqrt{\alpha_x^2 + \alpha_y^2 + \alpha_z^2} = 1. \quad (4.18)$$

The offset wave vector \mathbf{d}_0 is non-zero if the symmetry line do not connect to the center of Brillouin zone Γ , for example the M - K line. The stiffness matrix is decomposed in to three parts

$$\mathbf{K}(\mathbf{k}) = \mathbf{K}_0 + k\mathbf{K}_1(\boldsymbol{\alpha}, \mathbf{d}_0) + k^2\mathbf{K}_2(\boldsymbol{\alpha}, \mathbf{d}_0). \quad (4.19)$$

Finally, we obtain a second order eigenproblem with respect to k :

$$\left(k^2\mathbf{K}_2(\boldsymbol{\alpha}) + k\mathbf{K}_1(\boldsymbol{\alpha}) + \mathbf{K}_0 - \omega^2\mathbf{M} \right) \mathbf{u} = \mathbf{0}. \quad (4.20)$$

To solve the second order eigenproblem, we can covert to a first order system with double size:

$$\left(\begin{bmatrix} \mathbf{K}_0 - \omega^2\mathbf{M} & \mathbf{0} \\ \mathbf{0} & \mathbf{J} \end{bmatrix} - k \begin{bmatrix} -\mathbf{K}_1 & -\mathbf{K}_2 \\ \mathbf{J} & \mathbf{0} \end{bmatrix} \right) \begin{bmatrix} \mathbf{u} \\ k\mathbf{u} \end{bmatrix} = \begin{bmatrix} \mathbf{0} \\ \mathbf{0} \end{bmatrix}, \quad (4.21)$$

where the matrix $\mathbf{J} = \epsilon\mathbf{I}$, ϵ is average of diagonal stiffness matrix.

Since the phononic plate is symmetric to its neutral plane, the flexural modes (antisymmetric modes) can be decoupled from in-plane modes (symmetric modes), and to calculate only the band structures and associated flexural modes, we use a half of thickness and enforce boundary conditions at lower face ($z = 0$):

$$u_x|_{z=0} = u_y|_{z=0} = 0, \quad (4.22)$$

while the in-plane modes are computed with boundary conditions:

$$u_z|_{z=0} = 0. \quad (4.23)$$

4.3 Topological Phononics

In the theory of topological band insulators, topology is used to feature topological phases of matter, i.e, the topologically invariant property. To detect localized states at interfaces of two materials, one can examine topological phase transition at the interfaces. In Chern insulators, the Berry phase [97, 98] can properly describe a quantum state that is slowly changing with respect to a set of time-dependent parameters $\mathbf{R}(t)$, and is used to characterize the topological invariant. Description of the system evolution is an adiabatic approximation and is reviewed in this section.

4.3.1 Adiabatic evolution

We introduce the time-dependent Schrödinger equation which is used to describe a quantum-mechanical system:

$$i\hbar \frac{\partial \Psi(t)}{\partial t} = H(t)\Psi(t), \quad (4.24)$$

and the associated instantaneous eigenproblem

$$H(t)\psi_n(t) = E_n(t)\psi_n(t). \quad (4.25)$$

Equation (4.25) is similar to the eigenvalue problems in classical mechanics (4.17) where time-dependent parameters are the wave vectors \mathbf{k} . We suppose the Hamiltonian adiabatically varies with time so that the stationary state eigenfunctions and eigenvalues also vary with time but remain orthonormal. The solutions of time-dependent Schrödinger equation (4.24) are written as

$$\Psi(t) = \sum_n c_n(t)\psi_n(t), \quad (4.26)$$

in which $c_n(t)$ are coefficients to be determined. Replacing the ansatz to the time-dependent Schrödinger equation, we obtain

$$i\hbar \sum_n (\dot{c}_n \psi_n + c_n \dot{\psi}_n) = \sum_n c_n E_n \psi_n. \quad (4.27)$$

Multiplying by $\langle \psi_k |$ gives

$$\begin{aligned} i\hbar \dot{c}_k &= c_k E_k - i\hbar \sum_n c_n \langle \psi_k | \dot{\psi}_n \rangle \\ &= \left(E_k - i\hbar \langle \psi_k | \dot{\psi}_k \rangle \right) c_k - i\hbar \sum_{n \neq k} c_n \langle \psi_k | \dot{\psi}_n \rangle. \end{aligned} \quad (4.28)$$

We can determine the term $\langle \psi_k | \dot{\psi}_n \rangle$ by time derivative Eq. (4.25)

$$\dot{H}(t)\psi_n + H(t)\dot{\psi}_n = \dot{E}_n(t)\psi_n(t) + E_n(t)\dot{\psi}_n(t), \quad (4.29)$$

and multiply by $\langle \psi_k |$ with $k \neq n$ gives

$$\langle \psi_k | \dot{H}(t) | \psi_n \rangle + \langle \psi_k | H(t) | \dot{\psi}_n \rangle = E_n(t) \langle \psi_k | \dot{\psi}_n \rangle, \quad (4.30)$$

or

$$\langle \psi_k | \dot{\psi}_n \rangle = \frac{\langle \psi_k | \dot{H}(t) | \psi_n \rangle}{E_n(t) - E_k(t)} = \frac{\dot{H}_{kn}}{E_n(t) - E_k(t)}. \quad (4.31)$$

Therefore, if we are considering the adiabatic evolution with variation of the Hamiltonian is small with respect to time, and there are no degeneracy among eigenstates, i.e., $E_n \neq E_k$, then we can neglect the sum term in (4.28) and

$$i\hbar \dot{c}_k = \left(E_k - i\hbar \langle \psi_k | \dot{\psi}_k \rangle \right) c_k, \quad (4.32)$$

or

$$\frac{\dot{c}_k}{c_k} = \frac{1}{i\hbar} \left(E_k - i\hbar \langle \psi_k | \dot{\psi}_k \rangle \right). \quad (4.33)$$

Solving by integrating along time interval gives

$$\ln c_k = \frac{1}{i\hbar} \int_0^t \left(E_k(\tau) - i\hbar \langle \psi_k(\tau) | \frac{\partial \psi_k}{\partial \tau} \rangle \right) d\tau + \text{Const.} \quad (4.34)$$

$$\begin{aligned} c_k(t) &= c_k(0) \exp \left(\frac{1}{i\hbar} \int_0^t E_k(\tau) d\tau \right) \exp \left(i \int_0^t \langle \psi_k(\tau) | \frac{\partial \psi_k}{\partial \tau} \rangle d\tau \right) \\ &= c_k(0) e^{i\theta_k(t)} e^{i\gamma_k(t)}. \end{aligned} \quad (4.35)$$

Here, we define two distinct phases, namely, dynamical phase:

$$\theta_k(t) = -\frac{1}{\hbar} \int_0^t E_k(\tau) d\tau, \quad (4.36)$$

and geometric phase:

$$\gamma_k(t) = \int_0^t i \langle \psi_k(\tau) | \frac{\partial \psi_k}{\partial \tau} \rangle d\tau. \quad (4.37)$$

The dynamical phase depend on energy state of the system and the elapsed time, while the geometric phase depend on eigenstates.

4.3.2 Berry phase and Chern number

Assume the Hamiltonian H depends on a set of time-dependent parameters $\mathbf{R}(t) = \{R_1(t), \dots, R_N(t)\}$. Then the instantaneous eigenproblem become

$$H(\mathbf{R})\psi_n(\mathbf{R}) = E_n(\mathbf{R})\psi_n(\mathbf{R}). \quad (4.38)$$

The geometric phase is written as

$$\gamma_k(t) = \int_0^t i \langle \psi_k(\tau) | \frac{\partial \psi_k}{\partial \tau} \rangle d\tau = \int_0^t i \langle \psi_k(\mathbf{R}(\tau)) | \nabla_{\mathbf{R}} \psi_k(\mathbf{R}(\tau)) \rangle \cdot \frac{d\mathbf{R}}{d\tau} d\tau. \quad (4.39)$$

The Berry phase are defined as

$$\gamma_k(t_f) = \int_{\mathbf{R}_i}^{\mathbf{R}_f} i \langle \psi_k(\mathbf{R}) | \nabla_{\mathbf{R}} \psi_k(\mathbf{R}) \rangle \cdot d\mathbf{R}, \quad (4.40)$$

where \mathbf{R}_i and \mathbf{R}_f are initial and final values of $\mathbf{R}(t)$ at time t_i and t_f , respectively. The integrand is called Berry connection $\mathbf{A}_n = i \langle \psi_k(\mathbf{R}) | \nabla_{\mathbf{R}} \psi_k(\mathbf{R}) \rangle$. For a close path in 3D, the Berry phase become

$$\gamma_k[C] = \oint_C \mathbf{A}_n \cdot d\mathbf{R} = \int_S \nabla_{\mathbf{R}} \times \mathbf{A}_n \cdot d\mathbf{S} = \int_S \mathbf{B} \cdot d\mathbf{S}, \quad (4.41)$$

where integrand \mathbf{B} is Berry curvature.

Specific to two-dimensional lattice, the Brillouin zone swept by the momentum vectors (k_x, k_y) , $(k_x + 2\pi, k_y)$ and $(k_x, k_y + 2\pi)$ are equivalent due to periodic boundary conditions. Then the parameter space has a topology of a torus (Fig. 4.3). The Berry connection of n -th band and the Berry curvature are

$$\begin{aligned} A_{k_j}^{(n)} &= i \langle \psi_n(\mathbf{k}) | \nabla_{k_j} \psi_n(\mathbf{k}) \rangle, \quad k_j = \{k_x, k_y\}, \\ B^{(n)} &= \frac{\partial A_{k_y}^{(n)}}{\partial k_x} - \frac{\partial A_{k_x}^{(n)}}{\partial k_y}. \end{aligned} \quad (4.42)$$

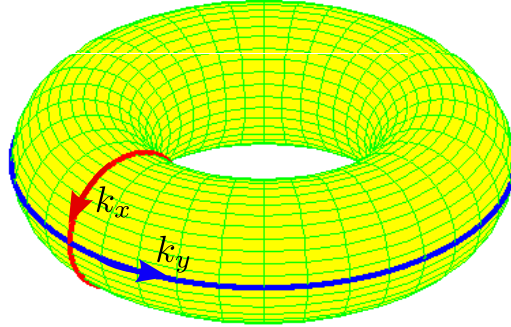


Figure 4.3: Periodic of momentum vectors in two-dimensional lattice.

The Chern number of each eigenstate is surface integral of the Berry curvature over the entire first Brillouin zone

$$C^{(n)} = \frac{1}{2\pi} \int_{BZ} B^{(n)} dk_x dk_y. \quad (4.43)$$

Thus, if two materials with different Chern numbers, a topological phase transition occurs at their interfaces with the emergence of topologically protected edge states.

4.4 Designing C^6 Unit Cell Exhibiting Dipole (p_x, p_y) and Quadrupole $(d_{x^2-y^2}, d_{xy})$ Modes

Designing a C^{6v} symmetry hexagonal plate unit cell with double Dirac cone by zone folding is followed by breaking translational symmetry to get two opposite topologies A and B [93]

by topology optimization. Rather hereby we propose to directly design two topologically distinct hexagonal plate unit cells with C^6 symmetry, the double Dirac cone topology design is circumvented.

We stick to considering only anti-symmetric plate modes [92], that can be separated from the full plate band structure by applying zero in-plane displacements at the mid-surface (see Eq. (4.22)).

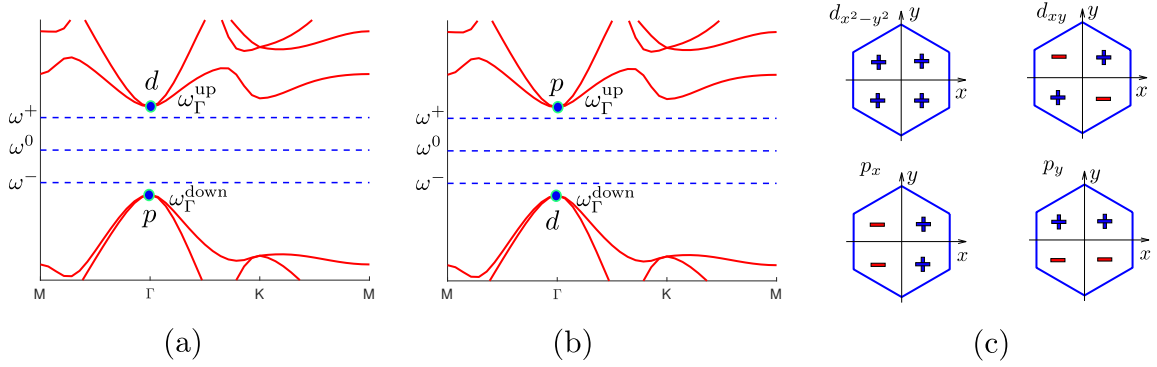


Figure 4.4: Illustration of target band structure for (a) Topology A, (b) Topology B. (c) Nature of dipole (p_x, p_y) and quadrupole ($d_{x^2-y^2}, d_{xy}$) modes.

Plate unit cell topologies A and B , need to be inverse designed with band gaps at a common frequency range of (ω^-, ω^+) . In addition, two-fold degeneracy has to exist between the upper modes at or above ω^+ and between the lower modes at or below ω^- . Figure 4.4 shows the target band structure for unit cell A and B . For unit cell A , the associated eigen displacements of the two lower and upper degenerate modes should be dipole (p_x, p_y) and quadrupole ($d_{x^2-y^2}, d_{xy}$) respectively. For unit cell B to be topologically opposite to unit cell A , the two lower and upper degenerate modes should be quadrupole ($d_{x^2-y^2}, d_{xy}$) and dipole (p_x, p_y), respectively.

In following, we briefly show the objective functions and constraint for the two approaches based on dispersion equation and equilibrium equation in design C^6 unit cell exhibiting modes with symmetries like quadrupole ($d_{x^2-y^2}, d_{xy}$) and dipole (p_x, p_y) orbitals.

4.4.1 I. Dispersion equation approach

The objective function has two parts, (a) to minimize the frequency gap between any two arbitrary bands and ω^- to a tolerance value at Γ point, (b) to minimize the frequency gap between any two arbitrary bands and ω^+ to a tolerance value at Γ point. The minimization of the objective function results in two degenerate lower bands (near ω^-) and two degenerate upper bands (near ω^+) as illustrated in Fig. 4.4a,b.

The objective function and constraints to design the unit cell type A are as follows:

$$\min : J^A = \sum_{i=1}^2 |\omega_{\Gamma}^{\text{down},i} - \omega^{-}| + \sum_{i=1}^2 |\omega_{\Gamma}^{\text{up},i} - \omega^{+}| \quad (4.44a)$$

$$\text{s.t.} : |\omega_{\Gamma}^{\text{down},1} - \omega_{\Gamma}^{\text{down},2}| < \epsilon \ \& \ |\omega_{\Gamma}^{\text{up},1} - \omega_{\Gamma}^{\text{up},2}| < \epsilon, \quad (4.44b)$$

$$\text{Gap exists between } (\omega_{\Gamma}^{\text{down},2}, \omega_{\Gamma}^{\text{up},1}), \quad (4.44c)$$

$$|u_z(-x) + u_z(x)| < \epsilon \ \& \ |u_z(-y) - u_z(y)| < \epsilon \ (\text{dipole } p_x \text{ at } \omega_{\Gamma}^{\text{down},1}), \quad (4.44d)$$

$$|u_z(-x) - u_z(x)| < \epsilon \ \& \ |u_z(-y) + u_z(y)| < \epsilon \ (\text{dipole } p_y \text{ at } \omega_{\Gamma}^{\text{down},2}), \quad (4.44e)$$

$$|u_z(-x) + u_z(x)| < \epsilon \ \& \ |u_z(-y) + u_z(y)| < \epsilon \ (\text{quadrupole } d_{xy} \text{ at } \omega_{\Gamma}^{\text{up},1}), \quad (4.44f)$$

$$|u_z(-x) - u_z(x)| < \epsilon \ \& \ |u_z(-y) - u_z(y)| < \epsilon \ (\text{quadrupole } d_{x^2-y^2} \text{ at } \omega_{\Gamma}^{\text{up},2}). \quad (4.44g)$$

We start the optimization algorithm by seeking two lower frequencies ($\omega_{\Gamma}^{\text{down},1}, \omega_{\Gamma}^{\text{down},2}$) and two higher frequencies ($\omega_{\Gamma}^{\text{up},1}, \omega_{\Gamma}^{\text{up},2}$) at point Γ such that: $\omega_{\Gamma}^{\text{down},1} \leq \omega_{\Gamma}^{\text{down},2} < \omega^0 < \omega_{\Gamma}^{\text{up},1} \leq \omega_{\Gamma}^{\text{up},2}$. This can be accomplished by searching for 4 eigenvalues near $\omega^0 = (\omega^{-} + \omega^{+})/2$ with the knowledge of eigenvalue orders and without calculating the whole band structure. The objective function (4.44a) keeps the lower and upper bands close to frequencies ω^{-} and ω^{+} respectively.

To ensure the two upper and lower bands to coalesce into two-fold degeneracy, we enforce the difference between the eigenfrequencies to be less than a positive small number ϵ by the constraint shown in (4.44b). In order to verify the existence of a complete gap between ($\omega_{\Gamma}^{\text{down},2}, \omega_{\Gamma}^{\text{up},1}$) as mentioned in the constraint (4.44c), we use the k - ω method to check whether there are any band at frequency $\omega \in [\omega_{\Gamma}^{\text{down},2}, \omega_{\Gamma}^{\text{up},1}]$ along the boundary of irreducible Brillouin zone, M - Γ and Γ - K . Finally, the constraint (4.44d-e) and (4.44f-g) ensure the lower and upper eigen displacements (u_z) having similar symmetries as p - and d -modes, respectively (see also Fig. 4.4c).

The objective function and constraints are the same for unit cell B , except that the constraints (4.44d-e) and (4.44f-g) are switched between upper and lower modes respectively, to obtain mode inversions.

4.4.2 II. Equilibrium equations approach

In the equilibrium equation approach, we design the unit cell topology by solving the differential equation of equilibrium. Resonance occurs when the excitation frequency matches with the natural frequency at the wave vector point. This can be achieved by applying loads on the unit cell that can emulate the dipole and quadrupole modes. Maximising the displacement at the load locations ensure that resonance occurs.

As shown in Fig. 4.5, p_x mode is made to occur at the target frequency by applying loads along $+Z$ at the centroids of the 1st and 2nd quadrant and along $-Z$ at the centroids of the 3rd and 4th quadrant. p_y mode is enforced at the target frequency by applying loads along $+Z$ at the centroids of the 1st and 4th quadrant and along $-Z$ at the centroids

of the 2nd and 3rd quadrant. d_{xy} mode is made to occur at the target frequency by applying loads along $+Z$ at the centroids of the 1st and 3rd quadrant and along $-Z$ at the centroids of the 2nd and 4th quadrant. $d_{x^2-y^2}$ mode is made to occur at the target frequency by applying loads along $+Z$ at the centroids of all the four quadrants. Two topologically distinct plate unit cell topologies are obtained by minimizing the work done ($\mathbf{U} \cdot \mathbf{F}$) by external force, \mathbf{F} applied onto the unit cell at certain frequencies (ω^+, ω^-) under periodic boundary conditions. The objective function for the optimization problem is as follows :

$$\min : J_d^A = 1 / \left(\mathbf{U}_{d_{x^2-y^2}}^+ \cdot \mathbf{F}_{d_{x^2-y^2}} + \mathbf{U}_{d_{xy}}^+ \cdot \mathbf{F}_{d_{xy}} \right), \quad (4.45a)$$

$$J_p^A = 1 / \left(\mathbf{U}_{p_x}^- \cdot \mathbf{F}_{p_x} + \mathbf{U}_{p_y}^- \cdot \mathbf{F}_{p_y} \right) \quad (4.45b)$$

$$J_d^B = 1 / \left(\mathbf{U}_{d_{x^2-y^2}}^- \cdot \mathbf{F}_{d_{x^2-y^2}} + \mathbf{U}_{d_{xy}}^- \cdot \mathbf{F}_{d_{xy}} \right) \quad (4.45c)$$

$$J_p^B = 1 / \left(\mathbf{U}_{p_x}^+ \cdot \mathbf{F}_{p_x} + \mathbf{U}_{p_y}^+ \cdot \mathbf{F}_{p_y} \right) \quad (4.45d)$$

$$\text{s.t : } \mathbf{D}_A^+ \mathbf{U}_{d_{x^2-y^2}}^+ = \mathbf{F}_{d_{x^2-y^2}} \quad (\text{for unitcell A}), \quad (4.45e)$$

$$\mathbf{D}_A^+ \mathbf{U}_{d_{xy}}^+ = \mathbf{F}_{d_{xy}}, \quad (4.45f)$$

$$\mathbf{D}_A^- \mathbf{U}_{p_x}^- = \mathbf{F}_{p_x}, \quad (4.45g)$$

$$\mathbf{D}_A^- \mathbf{U}_{p_y}^- = \mathbf{F}_{p_y}, \quad (4.45h)$$

$$\mathbf{D}_A^{+/-} = \mathbf{K}(\mathbf{k}) - (\omega^{+/-})^2 \mathbf{M}, \quad (4.45i)$$

$$\mathbf{D}_B^- \mathbf{U}_{d_{x^2-y^2}}^- = \mathbf{F}_{d_{x^2-y^2}} \quad (\text{for unitcell B}), \quad (4.45j)$$

$$\mathbf{D}_B^- \mathbf{U}_{d_{xy}}^- = \mathbf{F}_{d_{xy}}, \quad (4.45k)$$

$$\mathbf{D}_B^+ \mathbf{U}_{p_x}^+ = \mathbf{F}_{p_x}, \quad (4.45l)$$

$$\mathbf{D}_B^+ \mathbf{U}_{p_y}^+ = \mathbf{F}_{p_y}, \quad (4.45m)$$

$$\mathbf{D}_B^{+/-} = \mathbf{K}(\mathbf{k}) - (\omega^{+/-})^2 \mathbf{M}, \quad (4.45n)$$

$$(4.45o)$$

where \mathbf{K} and \mathbf{M} are stiffness and mass matrices, respectively. $\mathbf{U}^{+/-}$ denote displacement solutions at frequencies $\omega^{+/-}$ respectively. The wave vector \mathbf{k} is taken to be the one at Γ point. The frequency of the lower and upper degeneracies are ω^- and ω^+ respectively. It is evident from the Equations (4.45) that the d modes are enforced at ω^+ for topology A and at ω^- for topology B . The p modes are enforced at ω^- for topology A and at ω^+ for topology B .

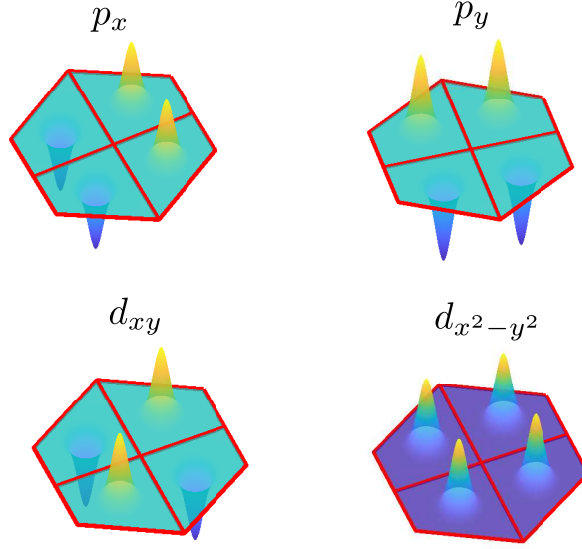


Figure 4.5: Force profiles.

4.4.3 Fine tuning the topologies based on Supercell band structure

Unit cells A and B obtained by both the methods, exhibit gap opening and mode inversion, consequently inducing a topological phase transition, hence, emulate strong spin-orbit coupling in the elastic wave analogue of QSHE. An interface comprising the two unit cell types are expected to offer topologically protected transport, indicated by two localized, counter-propagating modes intersecting each other (see also schematic in Fig. 4.6 and deformation plot in Fig. 4.11, Fig. 4.13). However, in spite of the unit cell topologies satisfying the requirements of SOC, there are cases of gaps existing at Γ point in the supercell band structure due to sudden jump in unit cell topology across the interface and this leads to absence of topological modes in the gap. The work by Chaunsali et al. [99] suggested gradual changes in geometries from one to the other domain to eliminate the gap between interface modes. The remedy is feasible for design topologies with tunable geometric parameters, while impractical for multivariate topology optimization problems.

In order to achieve gapless edge states, we solve an additional optimization problem on supercell to fine tune the obtained topologies. The cost function (4.46a-c) defined on the supercell domain to be minimized is,

$$\min : J_1^S = |\omega_0^{s,+} - \omega_0^{s,-}|, \quad (4.46a)$$

$$J_2^S = \frac{|u_z(\mathbf{x})|}{|u_z(\mathbf{x} \in \Omega)|} \quad \text{at } \omega_0^{s,-}, \quad (4.46b)$$

$$J_3^S = \frac{|u_z(\mathbf{x})|}{|u_z(\mathbf{x} \in \Omega)|} \quad \text{at } \omega_0^{s,+}. \quad (4.46c)$$

$$\text{s.t : No band interfere the line } \omega^s, \text{ except at } k_x = 0 (\Gamma \text{ point}). \quad (4.46d)$$

The objective function (4.46a) forces upper and lower frequencies ($\omega_0^{s,+}, \omega_0^{s,-}$) shown in

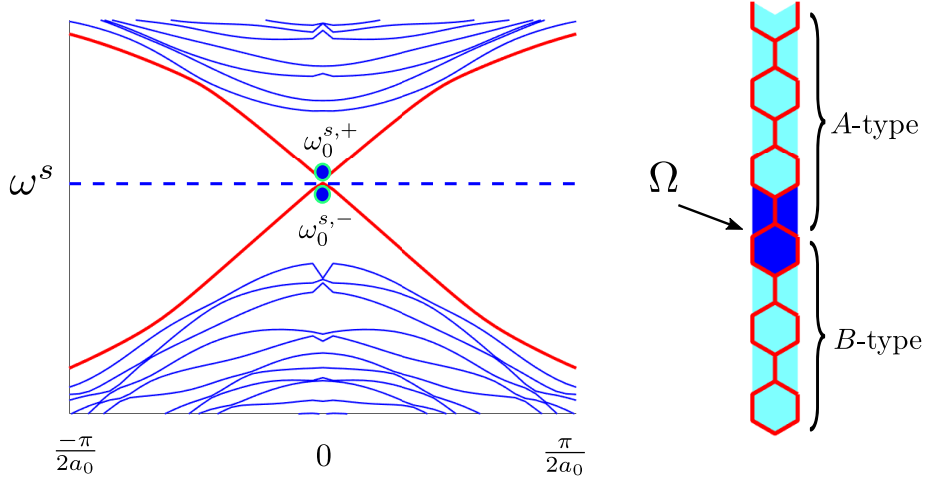


Figure 4.6: Optimization problem on supercell. Illustration of edge bands intersecting at Γ point (left). Schematic of the interface comprising unit cell A and B (right).

Fig. 4.6, to intersect at ω^s which is determined by:

$$\omega^s = \frac{\omega^- + \omega^+}{2}. \quad (4.47)$$

We search for two eigenfrequencies ($\omega_0^{s,-}$, $\omega_0^{s,+}$) at the Γ point such that $\omega_0^{s,-} \leq \omega^s \leq \omega_0^{s,+}$, then, the objective functions (4.46b-c) ensure the eigen displacements to localize at the interface domain Ω and the constraint (4.46d) guarantee that there are no other bands crossing at the horizontal line $\omega = \omega^s$ except for the degeneracy at Γ point. Consequently, this additional optimization problem yields a supercell band structure with gapless two counter propagating topological edge states.

4.5 Numerical Results

In the numerical examples shown in this Section, genetic algorithm based optimization method described in Appendix 4.A is adopted. The target lower and upper degeneracies are assigned as $[\omega^-, \omega^+] = [50, 60]$ kHz. Material properties of the plate of 4 mm thick are $\rho = 7850 \text{ kg/m}^3$, $E = 200 \text{ GPa}$, $\nu = 0.3$, and the side length of hexagon $a_0 = 20 \text{ mm}$.

The objective function shown in Equation (4.44) is minimized for the dispersion approach. The optimal topology A_I obtained and its corresponding band structure and eigen modes are shown in Fig. 4.7. The d and p modes emerge at ω^+ and ω^- respectively. The existence of a complete gap at all k -points is imposed by the k - ω method. Topologically opposite topology B_I , its band structure and eigen modes at degeneracies are shown in Fig. 4.8. The optimization procedure ensures band flip in topology B_I , the d and p modes exist at ω^- and ω^+ respectively.

Two topologically distinct plate unit cell topologies are obtained by minimizing Equation (4.45) with constraints shown in Equation (4.45e-o) for the equilibrium equation approach. The designed unit cell topology A_{II} with quadrupole modes at ω^+ and dipole modes at ω^-

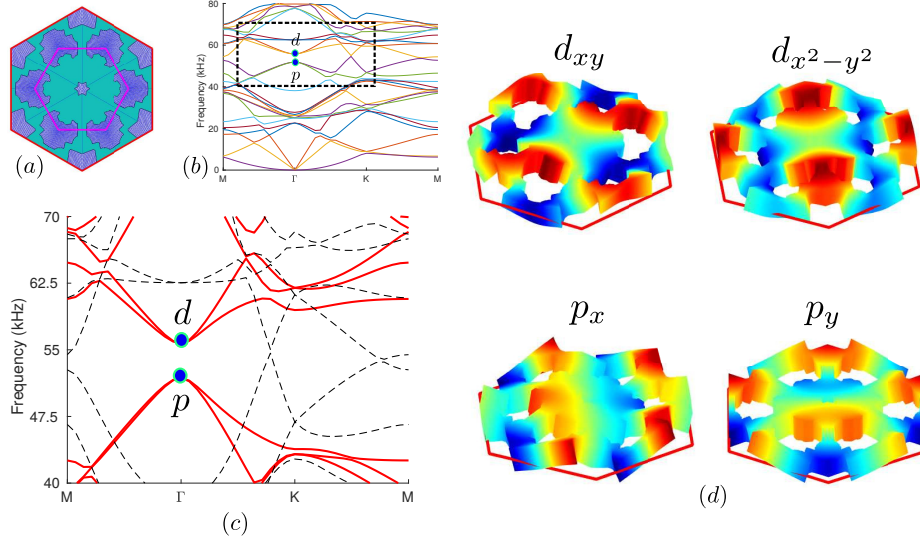


Figure 4.7: (a) Optimized unit cell topology A_I . (b) Band structure without mode separation. (c) Inset from (b), where red solid lines denote asymmetric modes and black dashed lines denote symmetric modes. (d) Deformation modes p and d at two-fold degenerate points, the color indicates magnitude of u_z displacement component.

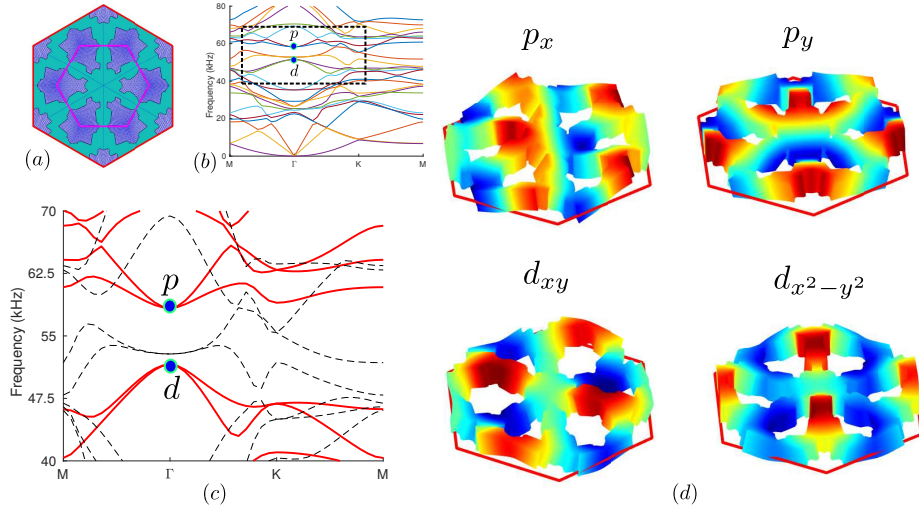


Figure 4.8: (a) Optimized unit cell topology B_I . (b) Band structure without mode separation. (c) Inset from (b), where red solid lines denote asymmetric modes and black dashed lines denote symmetric modes. (d) Deformation modes p and d at two-fold degeneracy points, the color indicates magnitude of u_z displacement component.

is shown in Fig. 4.9. The topology B_{II} with dipole modes at ω^+ and quadrupole modes at ω^- is shown in Fig. 4.10. Appropriate force profiles are chosen in order to exert a flip in the eigenmodes of the unit cells A_{II} and B_{II} .

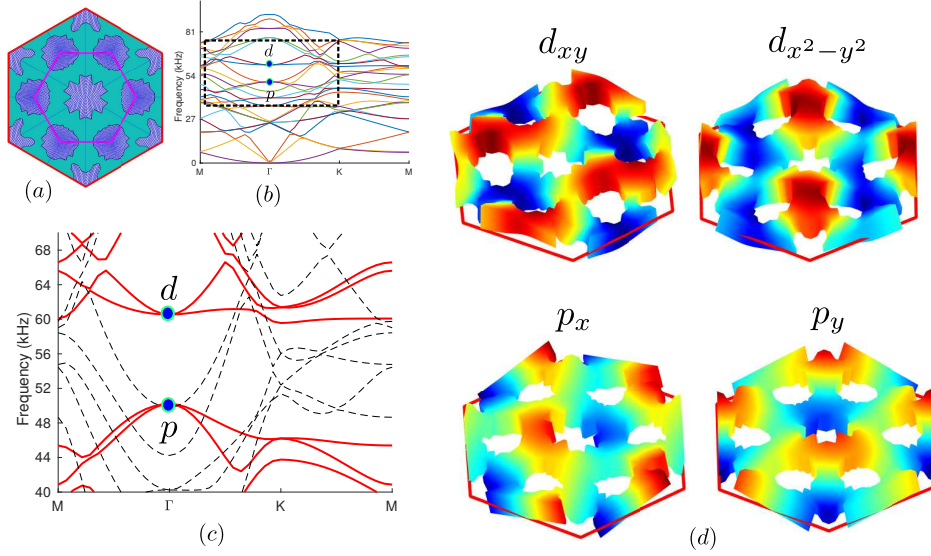


Figure 4.9: (a) Optimized unit cell type A_{II} . (b) Band structure without mode separation. (c) Inset from (b), where red solid lines denote asymmetric modes and black dashed lines denote symmetric modes. (d) Deformation modes p and d at two-fold degeneracy points, the colors indicate magnitude of u_z displacement component.

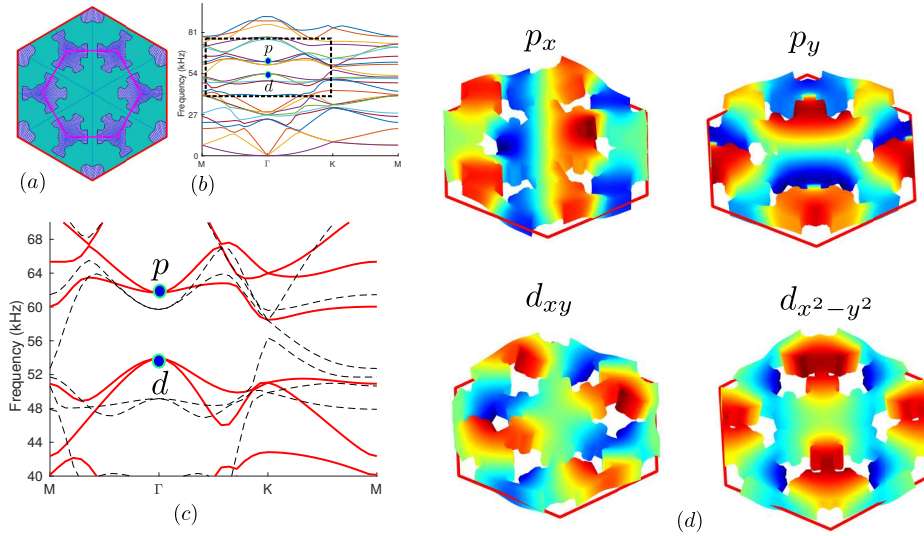


Figure 4.10: (a) Optimized unit cell type B_{II} . (b) Band structure without mode separation. (c) Inset from (b), where red solid lines denote asymmetric modes and black dashed lines denote symmetric modes. (d) Deformation modes p and d at twofold degeneracy points, the color indicate magnitude of u_z displacement component.

4.5.1 Elastic Pseudospin Wave Propagation at TI Interface

The topologies obtained by both the methods are corrected in order to ensure that the interface modes intersect. The supercell band structure obtained with corrected topologies by Method *I* and Method *II* are shown in Fig. 4.11 and Fig. 4.13 respectively.

In order to prove that the topologies inverse designed are topologically opposite and the behaviour is analogous to QSHE, the topologies A and B are assembled in a periodic structure with intersecting interfaces (plus interface). Topology B is periodic in first and third quadrant, topology A is periodic in second and fourth quadrant.

Figure 4.12 shows the periodic structure with plus interface comprising topologies designed by Method I. Time domain analysis is performed at a frequency of $f = 54.0$ kHz with a time step $\Delta t = 6 \times 10^{-3} \mu\text{s}$. Newmark- α time integration scheme is adopted. The simulation stops at time $t = 0.9 \mu\text{s}$. The structure is excited at the interface in the negative X-axis. The elastic wave with anti-clockwise spin propagates to the right and the elastic wave with clockwise spin propagates to the left of the excitation point. The anti-clockwise spin wave can propagate only through those interfaces which has topology A_I to its left and topology B_I at its right side. So the elastic wave bifurcates and reaches the top and bottom ends of the periodic structure. The anti-clockwise spin wave could not travel along the positive X-axis interface as for a wave travelling along positive X-axis, topology B_I lies to its left and topology A_I lies to its right. The incoming wave has to change its spin from anticlockwise to clockwise for it to travel along positive X-axis. As the wave cannot change spin the incoming anti-clockwise spin wave can seldom travel through the positive X-axis interface. This wave propagation behaviour in plus interface confirms the existence of two opposite spins and thereby the inverse designed topologies to be the components of an elastic wave analogue to QSHE based TI.

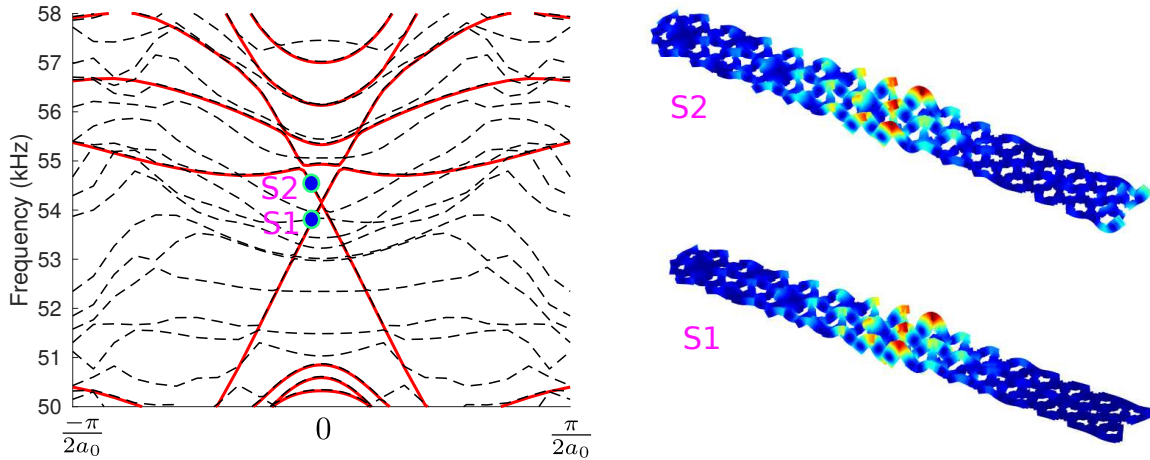


Figure 4.11: Band structure of supercell constructed from two unit cells A_I and B_I (left). Plot of eigenmodes at the points S1 & S2 in the band structure (right).

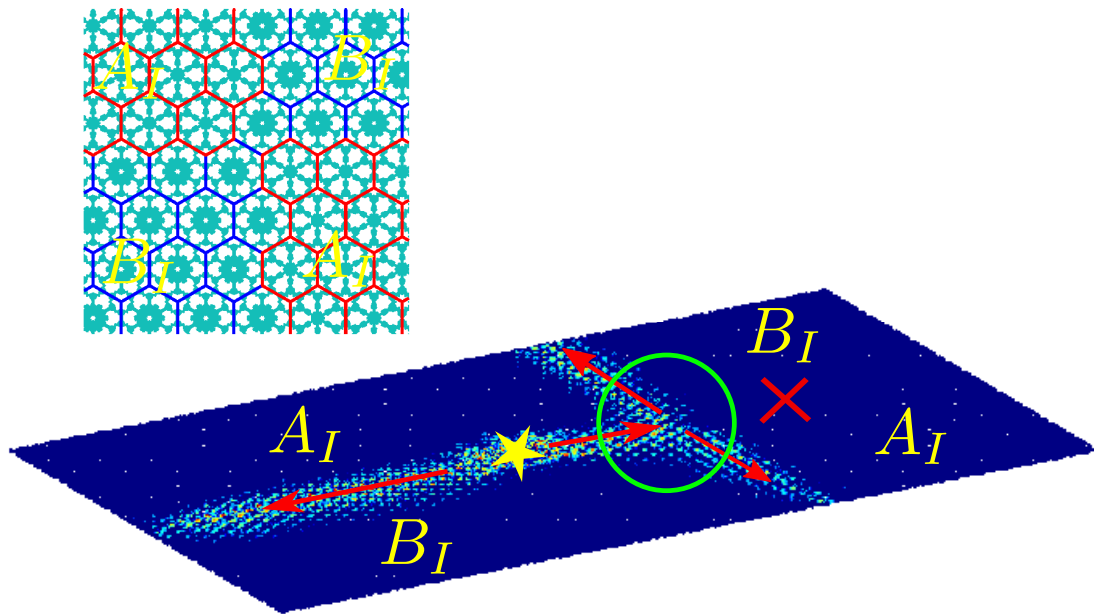


Figure 4.12: Elastic wave propagating in full plate model with plus interface constructed from two unit cell A_I and B_I .

The topologies designed using the Method II also show spin dependent propagation as shown in Figure 4.14.

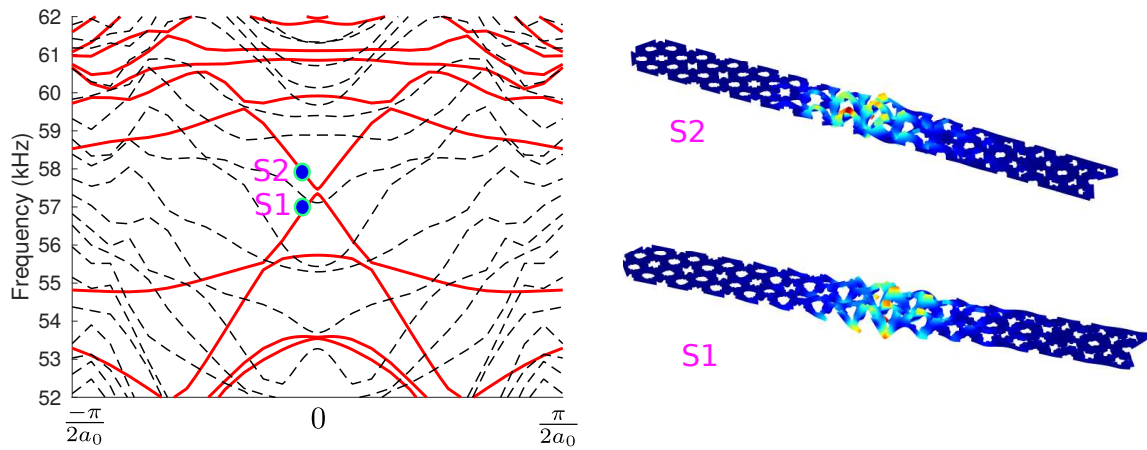


Figure 4.13: Band structures of supercell constructed from two unit cells A_{II} and B_{II} (left). Plot of eigenmodes at the points S1 & S2 in the band structure (right).

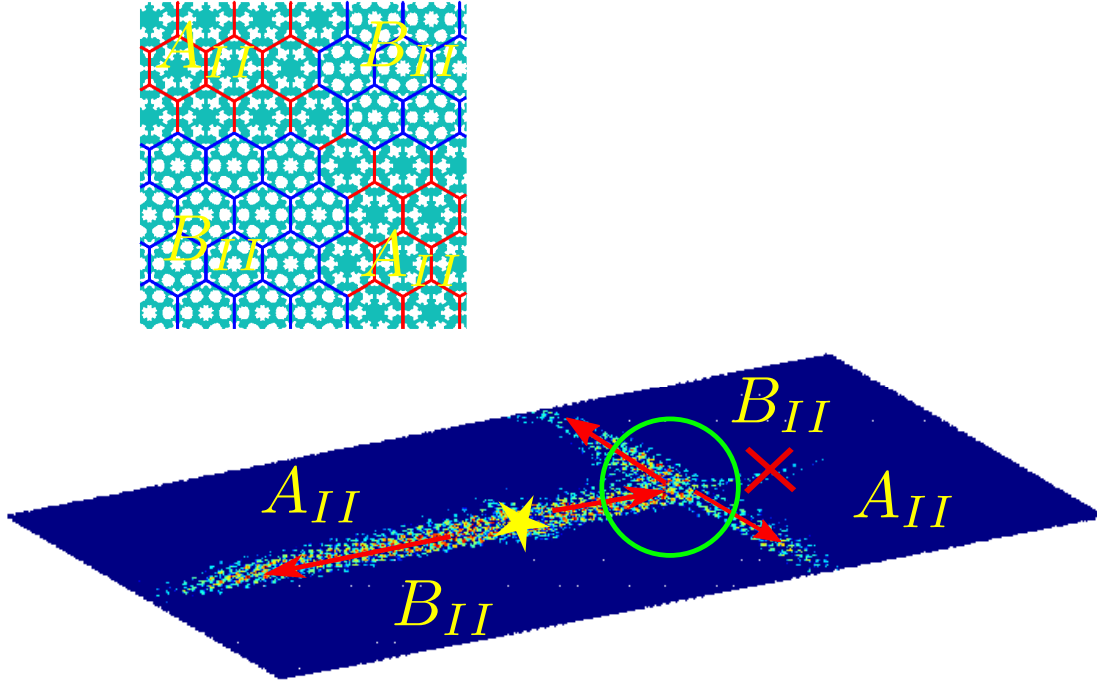


Figure 4.14: Elastic wave propagating in full plate model with plus interface constructed from two unit cell A_{II} and B_{II} .

4.5.2 Waveguide to circumvent damages

In case of a structure with defects, some steps need to be taken in order to prevent aggravation of the damage and eventual failure. Hereby, we consider a structure with an elliptical void subjected to an incoming excitation wave at a frequency of 57.5 kHz. The incoming out-of-plane wave may lead to emergence of crack in the vicinity of the sharp corners of the elliptical void. We propose to imprint the inverse designed topologies A_{II} and B_{II} onto the plate structure such that the incoming wave can circumvent the void and at the same time can continue to reach the right end of the plate. The defect plate without and with topology A-B interface, subjected to external excitation at the left end are shown in Figure 4.15. The comparison between the stress distribution in the vicinity of the corner of the elliptical void is shown in the figure. It can be seen that the stress is several orders of magnitude lower and negligible for the plate with A-B interface showing the potential of elastic wave TIs in damage control of vulnerable structures.

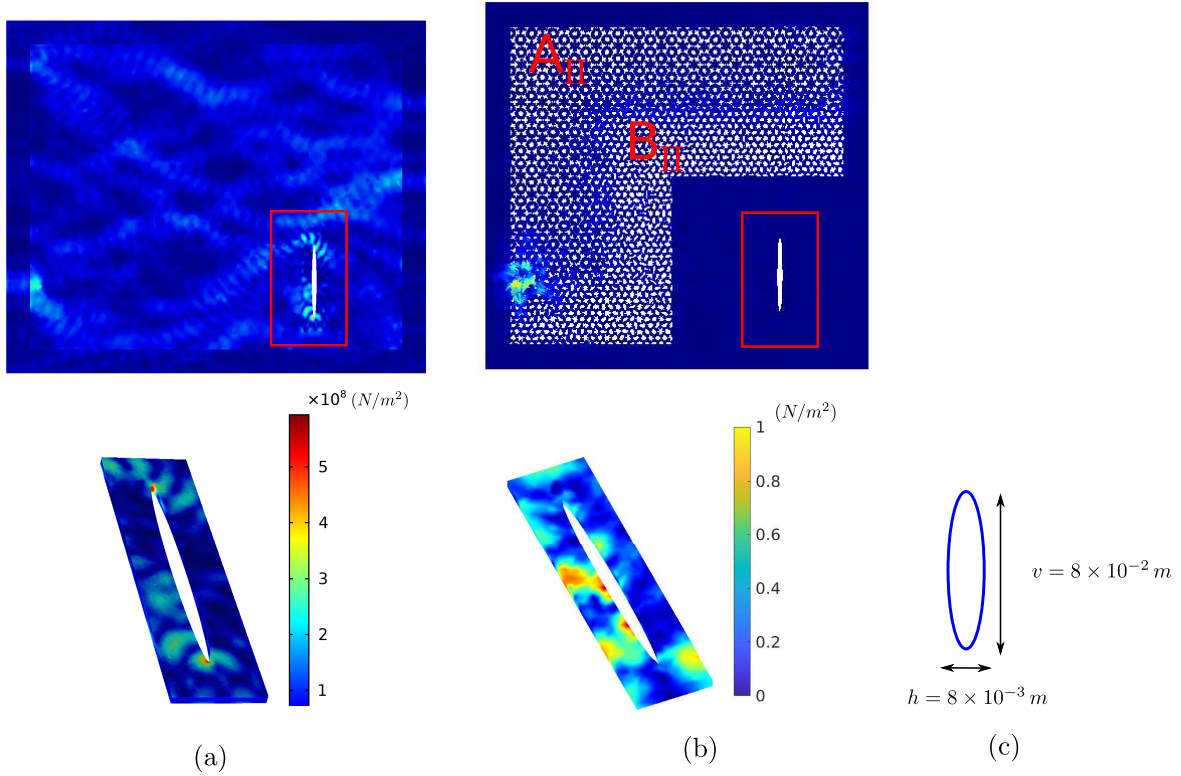


Figure 4.15: (a) and (b) Damaged domain with and without designed periodic phononic plate respectively. Top row: magnitude displacement plot. Bottom row: von Mises stress. Frequency domain simulation at $f = 57.5$ kHz. (c) Geometry of the elliptical void.

4.6 Discussion

This work demonstrates the potential of topological phononic plate unit cell topologies in damage protection. The proposed inverse design method using genetic algorithms and the objective functions formulated negate the trial and error process of obtaining topologically distinct C^6 topologies. Though the phononic plate unit cells can be inverse designed over desired frequency range, the plate thickness can also be scaled up or down to the frequency of interest. The incoming excitations towards cracks or flaws in a structure can be diverted by an add on or embedded topological interface. Broadband wave guiding can be accomplished by introducing jumps or non-uniformities in the phononic plate thickness. The applicability of helical edge states in phononic plates to damage prevention opens up wider possibilities as the designed topology can be scaled up to meters (for instance, to arrest cracks in a dam) or scaled down to nanometers (for instance, to guard an impurity in a nanomechanical system).

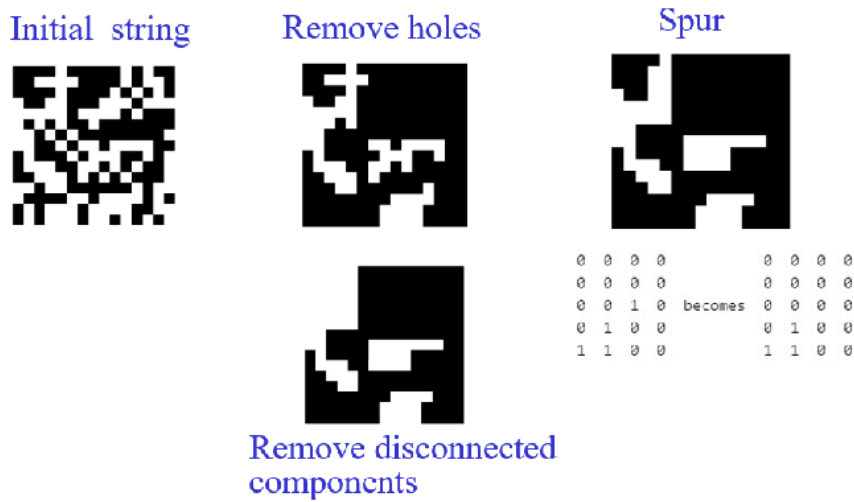


Figure 4.A.1: The crude initial topology from the randomly generated binary string is refined to obtain a meaningful topology.

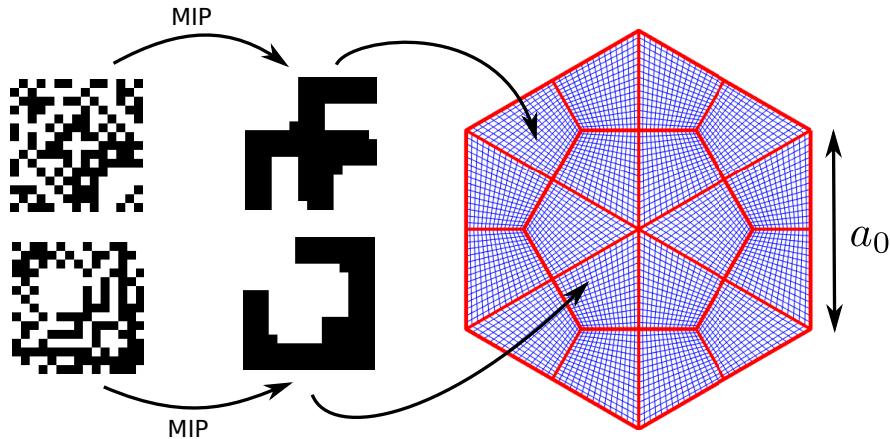


Figure 4.A.2: Mapping square topologies onto quadrilateral building blocks of C_{6v} symmetry hexagonal unit cell.

Appendix 4.A Genetic Algorithm Based Topology Optimization method

Genetic algorithm (GA) is adopted to design the unit cell topologies A and B . The design variables in GA are in the form of binary strings. The binary strings comprise 1s and 0s. For instance, topology of a square domain with 15×15 quadrilateral elements can be obtained by a binary string of length 225. Each binary digit is assigned to an element, the elements with 1s are considered to be solids and the ones with 0s assigned to them are considered as voids. The resulting topology is usually poor with disconnected components and checkerboard patterns. This topology cannot be directly utilized and need to refined as shown in Figure 4.A.1. The GA topology is checked for 1 pixel holes and they are removed.

Then the bits causing checkerboard patterns are identified and removed. The resulting topology is checked for disconnected components and the component with largest volume fraction is retained while the rest are removed.

This refined topology in a square domain is mapped onto the quadrilateral building blocks of a hexagonal unit cell as shown in Figure 4.A.2. Then the 3D unit cell is constructed by extruding the C^6 symmetry topology in thickness (z) direction.

Chapter 5

Inverse Design of Reconfigurable Piezoelectric Topological Phononic Plates

5.1 Introduction

Inspired by electronic topological insulators (TI), a class of materials that is conductive in its surface while insulating in the interior [11, 100], many analogues in mechanical systems have been developed [14, 87, 101]. The extension of the concept of TIs to phononic metamaterials has led to achieving topologically protected transport of elastic waves along predefined paths without backscattering even in the presence of defects.

Analogous to quantum Hall effect (QHE), topologically protected transport by breaking time-reversal (T) symmetry is possible in photonic crystals [102]. Wang et al. [82] and Nash et al. [15] introduced gyroscopic inertial effects in phononic lattices to break the T-symmetry, and realized phononic edge states that are chiral, unidirectional waveguide, and are not affected by disorders. Breaking T-symmetry in phononic crystals generally requires an input of external energy and so there are practical challenges in realizing an analogue to QHE in elastic metamaterials. On the other hand, mechanical topological insulators which are emulating quantum spin Hall effect (QSHE) offer protected helical edge states by spatial symmetry breaking in phononic lattices [16, 92]. The helical edge states enable wave to propagate forward and backward, while the chiral edge states restrict the wave to flow in only one direction. The backscattering immune propagation in case of QSHE based helical edge states is achieved due to the restriction that the wave can change direction only if there is spin flip. In QSHE, time reversal symmetry is preserved, the strong spin-orbit coupling enables band inversion and subsequent topological phase transition. In elastic analogues, phononic crystals have to offer four-fold degeneracy to form a double Dirac cone in its band structure, to ensure the existence of two spin states. Then, by symmetry reduction, topological phase transition occurs and results in a topological band gap. In case of a phononic analogue of quantum valley Hall effect (QVHE) space inversion symmetry (SIS) breaking in lattice structures is required. However, only two-fold degeneracy at the Dirac cone is necessary to open a topological band gap [88, 103].

Several works are available in the literature on designing topological phononic metama-

materials for guiding sound waves in sonic crystals [104–106], or elastic waves in phononic metamaterials [107–112]. The efforts predominantly demonstrate topological protection by engineering geometrical parameters of the phononic lattices. Inverse design methods adopt topology and shape optimization to meet the requirements like larger topological band width and flexible operating frequency ranges. The inverse design approaches are based on achieving intended unit cell band structure [93, 113] or localizing energy in specific paths of the periodic structure [94]. Reconfigurability or tunability by incorporating buckling members in lattices [114], pre-stressing soft phononic crystals [115] or embedding shunted piezoelectric patches [116, 117] overcome the constraint of fixed wave paths in case of passive phononic metamaterials. While the above mentioned works have significantly contributed to the design of tunable mechanical topological insulators, they do not present a general design methodology to obtain a unit cell topology with the intended objective of backscattering protected wave transport with adjustable interface paths.

Piezoelectric phononic plates are in general utilised in designing waveguides. For instance, in Vasseur et al. [118], a piezoelectric phononic plate is designed to have a band gap and defects in the periodic structure are utilised for waveguiding. The possibility of manipulating the band structure of piezoelectric phononic plates by varying the circuit conditions is discussed in Mekrache et al. [119]. Phononic plates analogous to electronic TI can serve as robust wave guides that are immune to backscattering due to defects and sharp bends [120]. Recently there are works on adopting phononic TIs for energy harvesting [121], by placing piezoelectric patches along the interface between topologically opposite unit cells. Nevertheless, there are certain constraints in phononic TIs, such as passive phononic plates offering fixed waveguide path and the interface state frequency range being narrow. The relative topological band gap width is less than or equal to 0.05 [116, 117, 122].

In the present work, we intend to overcome these shortcomings. We propose a methodology to design phononic unit cells of C^{6v} symmetry that are tunable and offer topological protection over a wider frequency range. We directly work with flexural waves in thin plates which brings our research close to practical applications. In a search space of a wide range of unit cell topologies with C^{6v} symmetry, we adopt genetic algorithms (GA) to identify topologies that have a Dirac cone with two-fold degeneracy. Then, topological band gaps and tunable wave propagation paths are achieved by adjusting the piezoelectric patches connected to external circuits.

5.2 Inverse Design Methodology

One possible way to achieve topological phase transitions through band inversion at the unit cell level is by breaking space-inversion symmetry in the unit cell, resulting in lifting the Dirac cone in the band structure into a gap. Firstly we design the phononic thin plate unit cell having a Dirac cone at the high symmetry point K . Then, the periodic phononic plate with repeated unit cells are attached with piezoelectric patches connected to passive external circuits that can generate electromechanical coupling effects to cause significant change in elastic moduli of the plate unit cell. Consequently, the space-inversion symmetry is broken in the phononic plate resulting in a topological band gap.

5.2.1 The first objective function: Forming two-fold degeneracy in piezoelectric phononic plates

In order to create geometries which have a Dirac cone at high-symmetry K point (Fig. 1a) between two consecutive modes, we perform topology optimization based on genetic algorithms [123, 124]. A string of binary digit is randomly generated and is mapped on a mesh of 15×15 , then we apply Morphological Image Processing (MIP) to avoid checkerboard pattern (Fig. 1b) in the resulting topology. The generated topology is projected onto each subdomain of the parallelogram to obtain unit cell topology. The topology of the parallelogram unit cell is extruded along the plate thickness. The resulting plate acts as a substrate (green) to a piezoelectric layer (blue) attached to it as illustrated in Fig. 2a-c. The piezoelectric layer is connected to external shunt circuits via two conductive electrodes (denoted by red/magenta circles). During the numerical calculation of band structure, we use a pair of fixed circular electrodes (with radius $r = 0.15 \times a$) for all topologies, and the center of electrodes are placed at point A and B as shown in Fig. 1b.

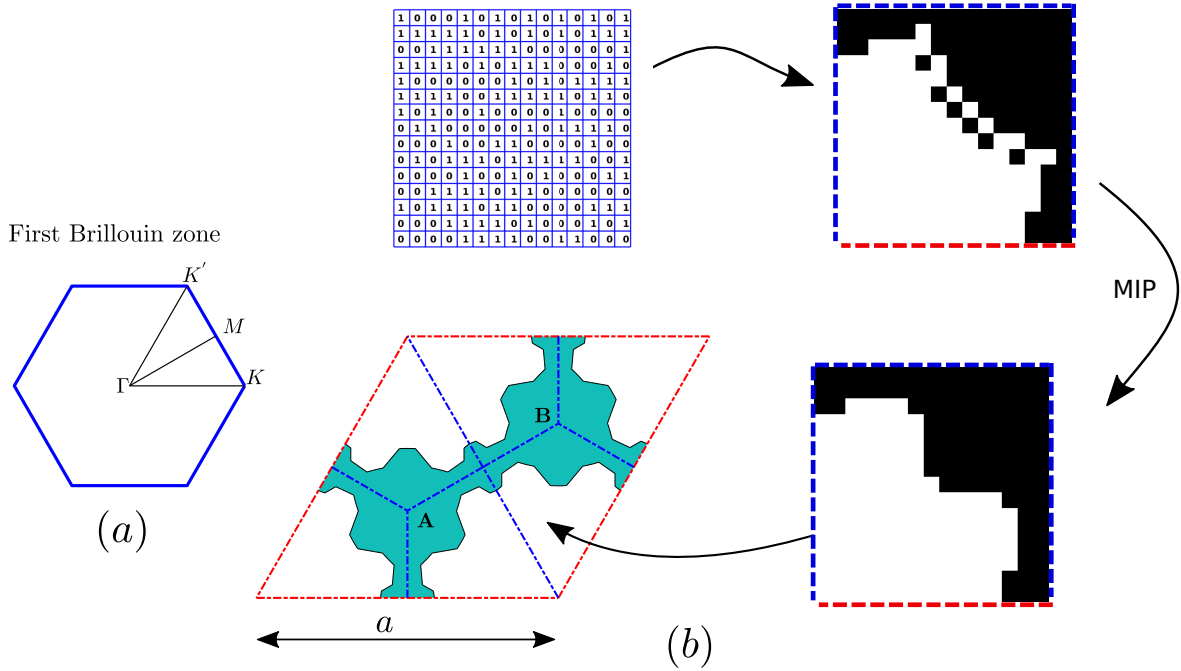


Figure 1: (a) First Brillouin zone in the reciprocal space of parallelogram. (b) Randomly generated binary string is rearranged and improved by Morphological Image Processing (MIP) to obtain a well connected unit cell topology.

The band structure is computed when the two switches are disconnected, i.e., under open-circuit (OC) condition (see Eq. (5.A.18)). The objective function and constraints (1) are formulated to force the frequencies of two modes (lower, L and upper, U) to be equal at K

point, resulting in a degeneracy (see Fig. 2d).

$$\begin{aligned} \min : J_1^{\text{OC}} &= |\omega_K^L - \omega_K^U| \\ \text{subject to: } &\begin{cases} \omega_\Gamma^U > \omega_K^U \ \& \ \omega_M^U > \omega_K^U, \\ \omega_\Gamma^L < \omega_K^L \ \& \ \omega_M^L < \omega_K^L, \end{cases} \end{aligned} \quad (1)$$

in which ω_K , ω_M and ω_Γ are frequencies at the corresponding high-symmetry points K , M and Γ in the reciprocal space.

5.2.2 The second objective function: Maximize the topological band gap by breaking inversion-symmetry

Following the first objective function and the constraints, the second step is to open a topological band gap by breaking space inversion symmetry. In order to do so, one of the electrodes is connected to an external shunted circuit (ZC) and the other is left open. During vibration, piezoelectric patches transfer the mechanical energy to the electric elements of the shunt circuit in order to be dissipated. This breaks the symmetry in stiffness of the unit cell. Subsequently reducing unit cell symmetry from C^{6v} to C^3 . Mathematical formulation describing the relation between voltage and electric charge is given in Eq. (5.A.19), Appendix 5.A.

This modification creates two types of unit cells, namely A and B . In unit cell type A , the left electrode is connected to the shunted circuit and the right electrode is left open as shown in Fig. 2b. In unit cell type B , the right electrode is connected to the shunted circuit and the left electrode is open as shown in Fig. 2c. These two unit cells with broken space inversion symmetry has to exhibit band inversion. A topological phase transition between unit cell types and opening of a topological band gap are expected as shown in Fig. 2e-f. In the second stage of inverse design, the band structure of unit cell types are calculated by numerical approaches described in Eq. (5.A.21), 5.A. This second objective function is added to the multi-objective topology optimization problem such that the topological band gap is complete and maximized.

$$\min : J_2^{\text{ZC}} = \frac{1}{|\omega_K^L - \omega_K^U|} \quad (2)$$

In summary, the multi-objective GA based topology optimization method comprises following steps:

1. A set number of population of random binary strings are generated and are morphed to C^{6v} symmetry plate unit cell topologies.
2. The objective functions and constraints in Equations (1), (2) are evaluated.
3. Ranking of the population based on objective function followed by crossover and mutation are performed to yield fitter off springs with each generation.

4. The GA algorithm is stopped when the tolerance limit for objective function is met and the fittest individual is the optimal plate unit cell topology.

Minimization of the objective function (1) ensures that the band structure of the unit cell with C^{6v} symmetry has a two-fold degeneracy. The second objective function (2) is minimized to enlarge the topological band gap opened by breaking space inversion symmetry.

5.3 Inverse Design Example

In this section, steps involved in the topology optimization problem explained in the previous section are followed to inverse design two topologically distinct plate unit cells. Material properties of the aluminum substrate and piezoelectric patches are listed in Table 1. The lattice length is $a = 0.052 m$, the substrate thickness is $h_{st} = 0.00125 m$ and the piezoelectric patch thickness is $h_{pzt} = 0.0005 m$. The lower and upper modes that has to degenerate and open a topological band gap are chosen as modes 4 and 5 respectively.

Aluminum	$E = 70 \text{ GPa}, \nu = 0.3, \rho = 2700 \text{ kg/m}^3$								
PZT-5A	Elastic constants c_{ij} (GPa) and density ρ (kg/m^3)								
	c_{11}	c_{12}	c_{13}	c_{22}	c_{33}	c_{44}	c_{55}	c_{66}	ρ
	120	75.2	75.1	120	110	210	210	226	7750
	Piezoelectric coefficients e_{ij} (C/m^2), κ_{ij}/κ_0 ($\kappa_0 = 8.85 \times 10^{-12} \text{ F/m}$)								
e_{31}	e_{32}	e_{33}	e_{24}	e_{25}	κ_{11}	κ_{22}	κ_{33}		
-5.35	-5.35	15.8	12.3	12.3	1730	1730	1700		

Table 1: Material properties of substrate (aluminum) and piezoelectric patch (PZT-5A).

We obtain the optimal topology as shown in Fig. 2a. Further details on the genetic algorithm parameters and the selection of the best candidate are described in Appendix 5.C. The band structure shows degeneracy between modes 4 and 5 at a frequency of 8.15 kHz. Two topologically distinct unit cells A and B are obtained by letting one of switches open and the other closed. The unit cells A and B and their corresponding band structures are shown in Fig. 2e and Fig. 2f respectively. It can be seen that the location of the band gap of unit cells A and B remain same with the frequency ranging between 7.6 to 8.7 kHz.

We can observe the inversion of eigenmodes between unit cells A and B in Fig. 3. At the wave vector point K , the eigenmode of 5th band of the unit cell A is similar to the eigenmode of 4th band of unit cell B (Fig. 3b,c). Similarly, the eigenmode of 4th band of unit cell A is similar to the eigenmode of 5th band of unit cell B (Fig. 3a,d). This indicates band inversion and subsequent topological phase transition between the two unit cells. Another indicator that possibly illustrates the mode inversion is energy flux pattern within the unit cells as shown in Fig. 4. The time averaged Poynting vectors (5.A.25) represent the energy flux distribution which is proportional to the magnitude of eigenmodes (Fig. 3) and their spatial derivative. Vortex patterns of the energy flux of the two unit cells are in opposite directions (red and magenta arrows).

Berry curvatures of the upper and lower band of the two unit cell types display localization at the points K and K' with opposite signs (more details Fig. 5.B.1, 5.B). The topological charge across the interface between unit cells A and B, $\Delta C = C_K^{4,A} - C_{K'}^{4,B}$, where the Chern numbers $C_{K/K'}$ are analytically calculated by the $\mathbf{k} \cdot \mathbf{p}$ perturbation method (5.B.3), we

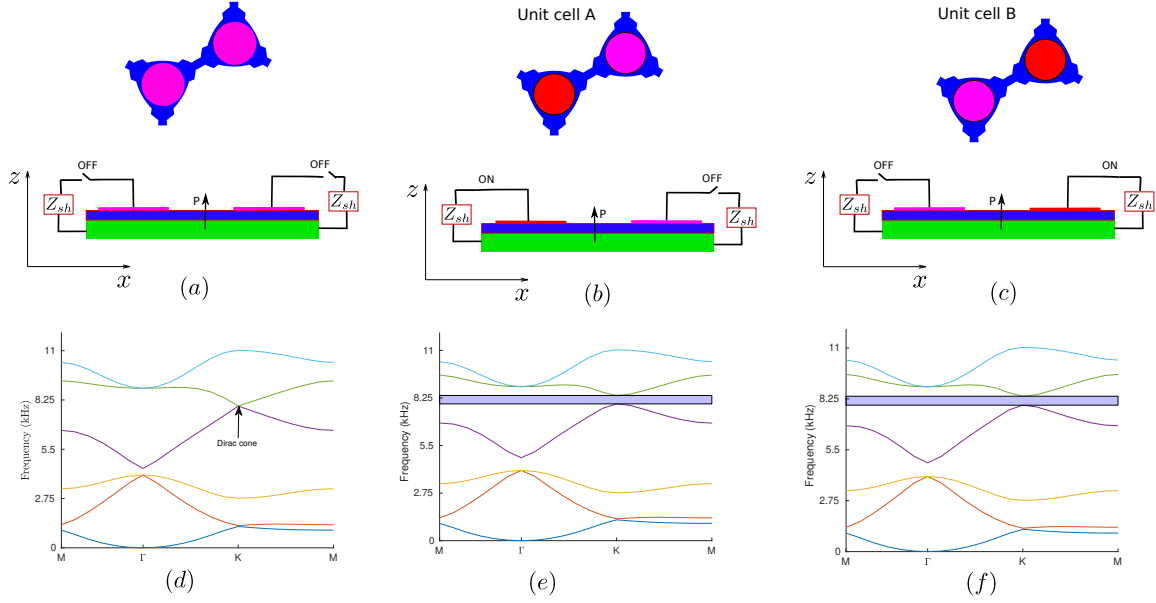


Figure 2: (a-c) Phononic composite plates comprising a piezoelectric patch (blue) attached to a substrate plate (green). Two electrodes (red and magenta denoting ON and OFF state, respectively) are connected to the upper surface of the piezoelectric patch. (d-f) Band structures of the optimized unit cell, when the two switches are open (open-circuit condition, a) and one of the switches is closed (shunted-circuit condition, e & f) and the other is open.

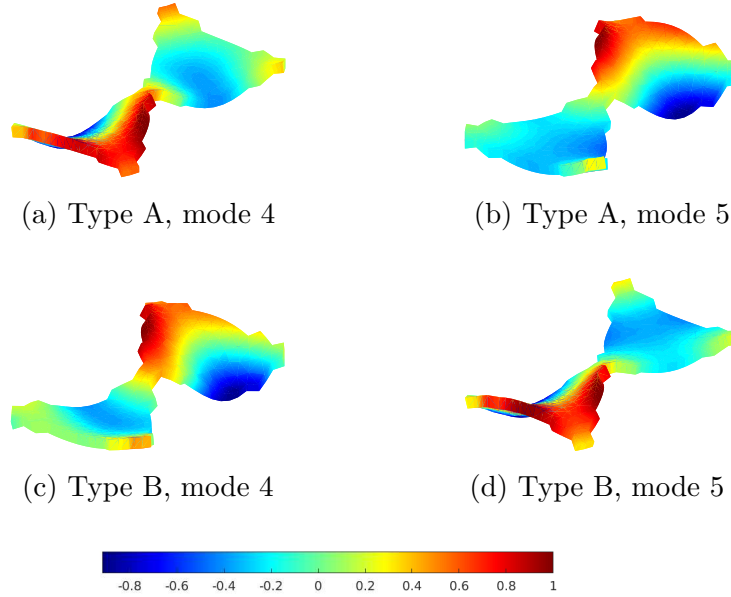


Figure 3: Eigenmodes of unit cells A and B at the K -point.

obtain $\Delta C = \pm 1$ for the lower and upper band respectively for the unit cell A, while Chern numbers are found to be having opposite signs $\Delta C = \mp 1$ for the unit cell B. The distinct valley Chern numbers ensure that the topologically protected edge modes are supported along the interface between unit cells A and B via bulk-boundary correspondence [11, 125].

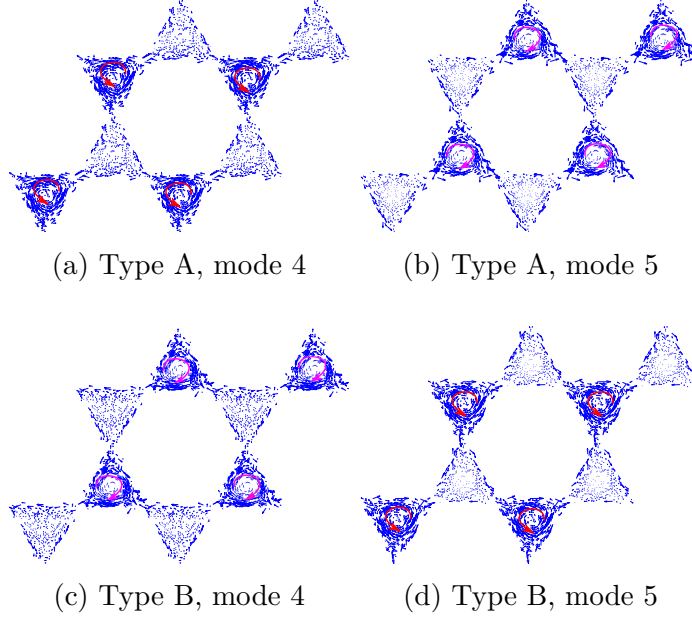


Figure 4: Mechanical energy flux at the K -point represented by Poynting vectors. Red and magenta arrow indicate vortex patterns of the energy flux.

5.4 Topological Edge States in Piezoelectric Phononic Plates

We further study the topologically protected localized modes at the interface by constructing a B-A-B type supercell comprising 12 unit cells such that two domain walls DW1 and DW2 are formed (Fig. 5a, top). The band structure displays two modes within the bandgap over the frequency range 7.6-8.7 kHz. The mode shapes (marked as the green and blue star in the corresponding band structures) further show localization of displacements at the interface between the two unit cell types (Fig. 5b). This clearly confirms that the gap is topologically non-trivial. However, the deformation corresponds to anti symmetric and symmetric modes at DW1 and DW2, respectively. It is due to the fact that valley-protected edge states inherit spatial parities [103, 126, 127].

The total displacement in flexural wave propagation is dominated by the u_z component, and the sign of u_z changes from positive to negative (or negative to positive) across the domain wall that supports antisymmetric modes (DW1). Therefore, the magnitude of u_z component tends to zero at the interface to ensure the antisymmetric condition while there are no such restrictions on u_z along DW2 (which supports symmetric modes). The antisymmetric modes lead to Bloch wave deafness [128] if the phononic periodic structure with domain wall is excited by incident plane waves that are normal to the boundary as illustrated in Fig. 6. For the incident waves, which are normal to the phononic crystal boundary ($x = 0$), modal conversion at the boundary can be quantitatively evaluated by:

$$\langle p_i | p_t \rangle = \int_y e^{i(k_{0x} - k_x)x} \tilde{p}_t(\mathbf{x}) dy = \int_y \tilde{p}_t(\mathbf{x}) dy \quad (\text{at } x=0), \quad (3)$$

where k_{0x} and k_x are wavevectors in the x -direction of the incident and Bloch wave, respectively. Conversion of modes (3) at the boundary is zero if Bloch wave $\tilde{p}_t(\mathbf{x})$ is

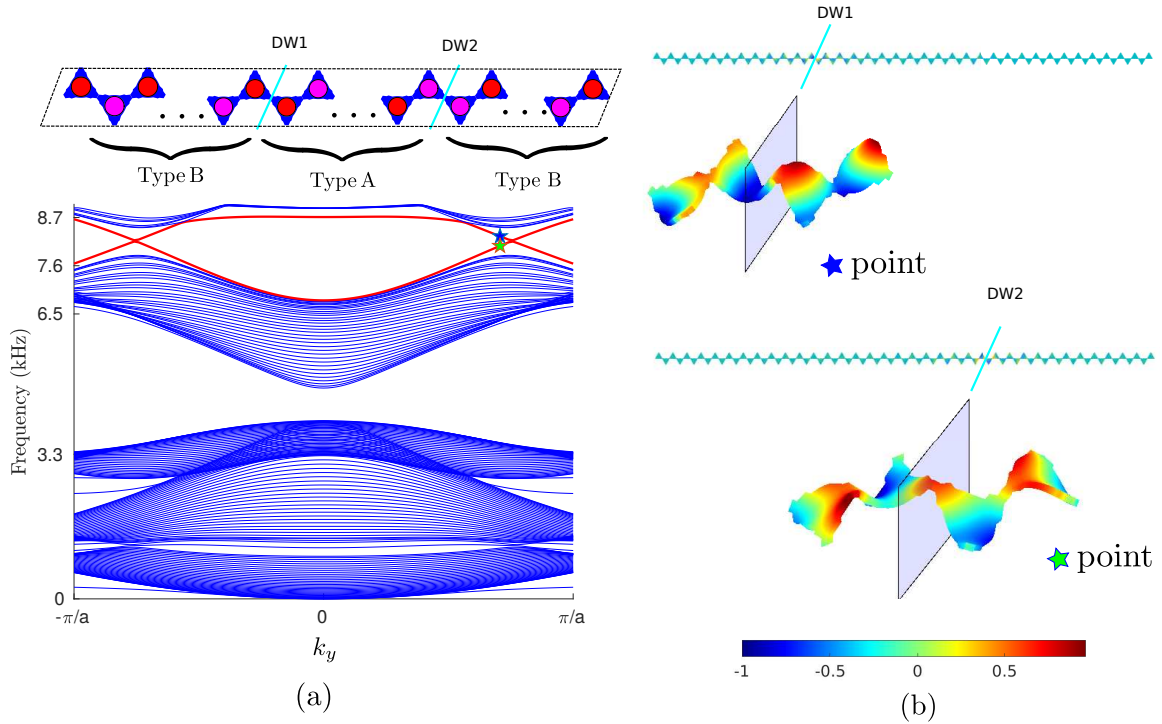


Figure 5: (a) Schematic and band structure of the supercell. (b) Selected eigenmodes at blue and green points show that the deformation is antisymmetric at DW1 and symmetric at DW2. Colorbar indicates the magnitude of out-of-plane displacement.

antisymmetric with respect to the x axis. Though the interface DW1 supports topologically protected edge states, the waves can propagate along the domain wall DW1, either if the incident waves are not normal, i.e., $k_{0y} \neq 0$, or if the excitation is from an antisymmetric source.

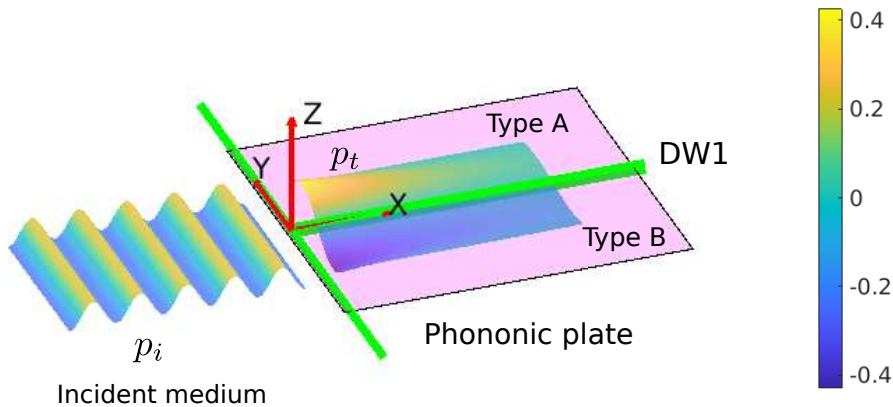


Figure 6: Illustration of the conversion of incident wave p_i to Bloch wave p_t in the phononic plate. Converted Bloch wave is antisymmetric with respect to the interface DW1.

To illustrate the robustness of topologically protected edge modes in being immune to backscattering at sharp edge corners, we construct a periodic plate structure assembled with

20×30 unit cells, forming a Z -interface with either DW1 or DW2 type domain walls. We numerically simulate wave propagation by frequency domain analysis at a frequency of $f = 8.2$ kHz and fixed (zero) displacement is applied along the boundaries. We adopt the approach in Liu and Semperlotti [114] to excite one-way propagating edge states. As shown in Fig. 5, the interface bands intersect at the frequency value of $f = 8.2$ kHz and at the wavevector $k_y \approx \mp \frac{2\pi}{3a}$ corresponding to K - and K' -polarization modes, respectively. Therefore, we use out-of-plane excitation sources with a phase difference of $\pi/3$ to initiate one-way propagation:

$$\begin{aligned} s^0(x_0, y_0) &= \bar{f} \exp(-j\omega t), \\ s^{-a}(x_0 - a, y_0) &= \bar{f} \exp(j\pi/3) \exp(-j\omega t), \\ s^{+a}(x_0 + a, y_0) &= \bar{f} \exp(j\pi/3) \exp(-j\omega t), \end{aligned} \quad (4)$$

where \bar{f} is the excitation magnitude. The single source $s^0(x_0, y_0)$ produces Bloch wave with different phases $-\frac{2\pi}{3}$ and $+\frac{2\pi}{3}$ at the right point $(x_0 + a, y_0)$ and left point $(x_0 - a, y_0)$, respectively. To create waves that propagate only to the left direction, the source s^{+a} is simultaneously excited in addition to s^0 , at the right point $(x_0 + a, y_0)$, which produces Bloch wave that cancels those from the source s^0 due to a phase difference of π .

In Figure 7, the two sources $\{s^0, s^{-a}\}$ are excited simultaneously to initiate the K - polarized edge state while $\{s^0, s^{+a}\}$ are for K' - polarization at the origin (x_0, y_0) indicated by a green point. The selective sources corresponding to K - or K' - polarized edge state trigger waves propagating along DW2 (top panel) in opposite directions and the localized propagation along topologically protected waveguide shows robust immunity to backscattering at the sharp corners of the Z -interface. Contrarily, DW1 (bottom panel) exhibits displacement localizing around the source position and no wave can propagate in the structure for both selective sources. It is due to the fact that the DW1 interface only supports antisymmetric modes in which displacement component u_z is suppressed, and therefore flexural waves cannot propagate.

Figure 8 shows simulation of a transient wave propagating along DW2 in the elastic wave TI. The green points indicate position of the applied source $\{s^0, s^{-a}\}$ such that the waves are expected to propagate from left to right along the Z -interface. In the bottom panel, we create defects by removing one unit cell inside the green circle in order to verify the robustness of the topological interface. Two snapshots of displacements are shown at the time instant $t=0.0049$ s, when the propagating wave bends around the first sharp corner and at $t=0.010$ s, when the wave travels across the defect location. Clearly, the propagating waves localize at the interface, there are no backscattering at the sharp corners or the material defect.

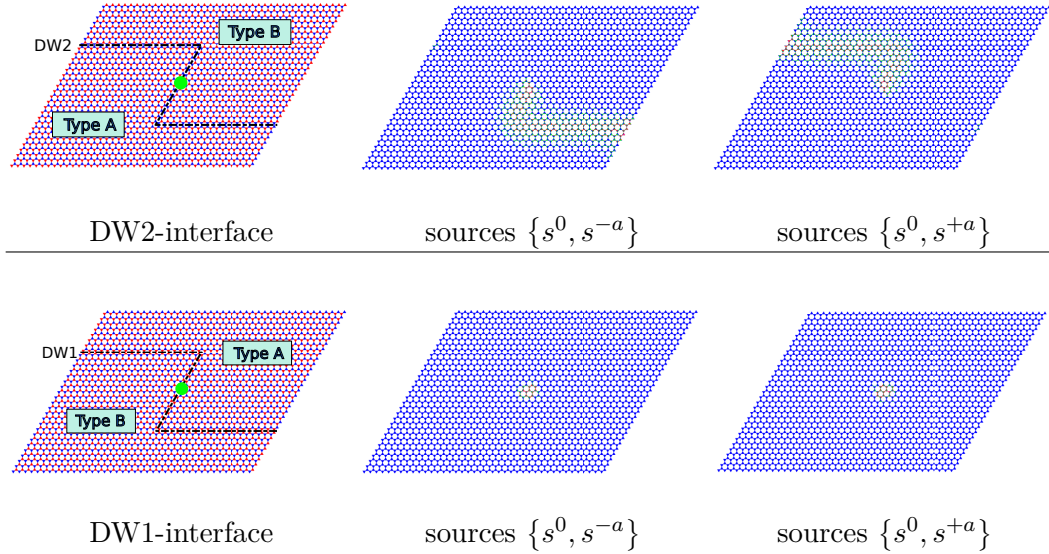


Figure 7: Wave propagation due to the topological edge state. Schematic of the Z -interface and magnitude of displacement showing elastic flexural wave propagation along DW1 (bottom) and DW2 (top) for two different sources $\{s^0, s^{-a}\}$ and $\{s^0, s^{+a}\}$.

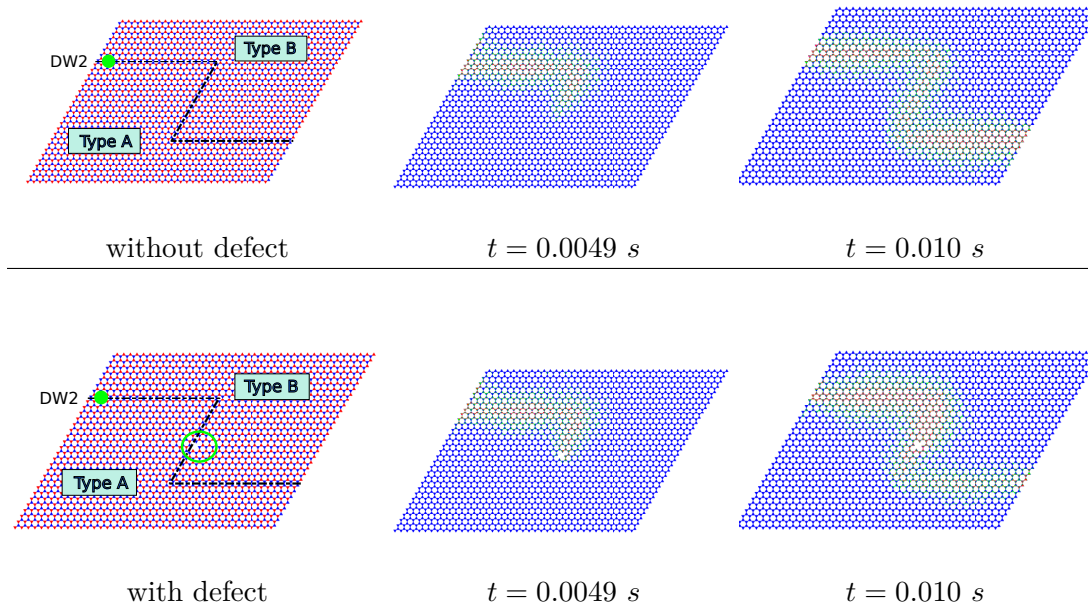


Figure 8: Simulation of transient wave propagating along Z -interface with and without defects. Snapshots of the displacement magnitude at $t = 0.0049 \text{ s}$ and $t = 0.010 \text{ s}$.

5.5 Conclusions

We have proposed and demonstrated a design methodology for the phononic plate with piezoelectric patches possessing topologically protected interface modes. It is possible to reconfigure the topological waveguide path by simply altering the connection status of the appropriate

piezoelectric patches. This shows the robustness of the proposed active phononic plate as it is impossible to alter the propagation path in case of passive phononic plates after their manufacture and assembly. Topology optimization with GA negates the necessary to follow a trial and error design process and also opens up possibilities to design a topology that has a topological band gap over desired frequency range and of desired bandwidth. The relative band gap width achieved by the optimal topology is $\Delta\omega/\omega_{\text{mid-gap}} = (8.7 - 7.6)/0.5/(8.7 + 7.6) = 0.135$, which is higher than the relative band gap width of the topologies available in literature [116, 129]. We are considering to implement this design approach for an elastic wave analogue to QSHE based electronic TIs, that requires a four fold degeneracy in the band structure, however the topological state offers spin-dependent interface propagation.

Appendix 5.A Finite Element Method for Piezoelectric plates

In this section, we present a finite element framework for wave propagation simulation in elastic plates with piezoelectric patches attached. We briefly introduce the governing equations for a linear piezoelectric medium and the weak formulation required for implementation of the finite element method. For structures with bonded thin piezoelectric patches, the electric potential across the composite is denoted by discrete variables defined on each piezoelectric patch [130]. Furthermore, the kinematic assumptions of *Mindlin-Reissner* plate theory are introduced to replace the three-dimensional solid model which in turn reduces the degrees of freedom in the finite element formulation [131, 132].

Consider a piezoelectric domain Ω , the governing equations are

$$\begin{aligned}\sigma_{ij,i} + f_j &= \rho \ddot{u}_j \\ D_{i,i} &= 0.\end{aligned}\tag{5.A.1}$$

Constitutive laws of a piezoelectric medium give the relationship between the elastic stress σ_{ij} and electric displacements D_i to elastic strain ε_{kl} and electric field E_i as follows:

$$\begin{aligned}\sigma_{ij} &= C_{ijkl}^E \varepsilon_{kl} - e_{kij} E_k \\ D_i &= e_{ikl} \varepsilon_{kl} + \kappa_{ik}^S E_k,\end{aligned}\tag{5.A.2}$$

where C_{ijkl}^E is the elastic modulus, e_{ikl} is the piezoelectric coupling coefficient, and κ_{ik}^S is the dielectric permittivity. For a small deformation in an elastic body, the relation between the mechanical strain and the displacement field u_j is:

$$\varepsilon_{ij} = \frac{1}{2} \left(\frac{\partial u_i}{\partial x_j} + \frac{\partial u_j}{\partial x_i} \right),\tag{5.A.3}$$

and the relation between the electric field E_i and the electric potential ϕ is

$$E_i = -\frac{\partial \phi}{\partial x_i}.\tag{5.A.4}$$

The following is the variational formulation, for implementation of the finite element method:

$$\begin{aligned} \int_{\Omega} C_{ijkl}^E \varepsilon_{ij}(\mathbf{u}) \varepsilon_{kl}(\delta \mathbf{u}) d\Omega - \int_{\Omega} e_{kij} E_k(\phi) \varepsilon_{ij}(\delta \mathbf{u}) d\Omega + \int_{\Omega} \rho \frac{\partial^2 u_i}{\partial t^2} \delta u_i d\Omega &= \int_{\Omega} f_i \delta u_i d\Omega + \int_{\Gamma_t} t_i \delta u_i d\Gamma \\ \int_{\Omega} e_{ikl} \varepsilon_{kl}(\mathbf{u}) E_i(\delta \phi) d\Omega + \int_{\Omega} \kappa_{ik}^S E_k(\phi) E_i(\delta \phi) d\Omega &= \int_{\Gamma_q} q^d \delta \phi d\Gamma + \int_{\Gamma_\phi} q^r \delta \phi d\Gamma, \end{aligned} \quad (5.A.5)$$

where q^d and q^r are the surface free electric charge and the reaction electric charge density, respectively.

The piezoelectric patches are polarized along the thickness direction and the electric field E_z across the piezoelectric patch is considered a constant (see Thomas et al. [130], Toftekær et al. [133]),

$$E_z^p = -\frac{\phi_+^p - \phi_-^p}{h^p} = -\frac{V^p}{h^p}, \quad \text{and } E_x^p = E_y^p = 0, \quad (5.A.6)$$

where the electric potentials ϕ_+^p and ϕ_-^p are uniform along the upper and lower electrode surface (we set $\phi_-^p = 0$), and V^p is the voltage applied on the electrode p . The free electric charge q^d is assumed to be zero. The reaction electric charges q^r in the upper and lower electrode of the patch p have equal magnitudes but opposite signs, so that the last integral term in (5.A.5) is

$$\int_{\Gamma_\phi} q^r \delta \phi d\Gamma = Q_+^p \delta \phi_+^p + Q_-^p \delta \phi_-^p = Q^p \delta V^p. \quad (5.A.7)$$

In plate structures, the out-of-plane stress component σ_{zz} is assumed to be zero, and the displacements are approximated as :

$$u(\mathbf{x}, t) = z\theta_x(x, y, t), \quad v(\mathbf{x}, t) = z\theta_y(x, y, t), \quad w(\mathbf{x}, t) = w_0(x, y, t), \quad (5.A.8)$$

where u , v , w are displacement components, and θ_x , θ_y are rotations about the x and y axes respectively. In phononic plates, the Bloch wave solution requires the displacement and rotations to have the following forms:

$$\begin{bmatrix} w_0(x, y, \mathbf{k}, t) \\ \theta_x(x, y, \mathbf{k}, t) \\ \theta_y(x, y, \mathbf{k}, t) \end{bmatrix} = \begin{bmatrix} \tilde{w}_0(x, y) \\ \tilde{\theta}_x(x, y) \\ \tilde{\theta}_y(x, y) \end{bmatrix} e^{j(k_x x + k_y y - \omega t)}, \quad (5.A.9)$$

where k_x , k_y are the components of reciprocal wave vectors, and ω is the temporal frequency. For the plate model, the displacements and strain vectors are re-written as [134]

$$\begin{bmatrix} u \\ v \\ w \end{bmatrix} = \underbrace{\begin{bmatrix} 0 & z & 0 \\ 0 & 0 & z \\ 1 & 0 & 0 \end{bmatrix}}_{\mathbf{Z}_u} \begin{bmatrix} \tilde{w}_0 \\ \tilde{\theta}_x \\ \tilde{\theta}_y \end{bmatrix} e^{j(k_x x + k_y y - \omega t)}, \quad (5.A.10)$$

and

$$\begin{bmatrix} \varepsilon_x \\ \varepsilon_y \\ 2\varepsilon_{yz} \\ 2\varepsilon_{xz} \\ 2\varepsilon_{xy} \end{bmatrix} = \underbrace{\begin{bmatrix} z & 0 & 0 & 0 & 0 \\ 0 & z & 0 & 0 & 0 \\ 0 & 0 & 1 & 0 & 0 \\ 0 & 0 & 0 & 1 & 0 \\ 0 & 0 & 0 & 0 & z \end{bmatrix}}_{\mathbf{Z}_\varepsilon} \underbrace{\begin{bmatrix} 0 & \frac{\partial}{\partial x} + jk_x & 0 \\ 0 & 0 & \frac{\partial}{\partial y} + jk_y \\ \frac{\partial}{\partial y} + jk_y & 0 & 1 \\ \frac{\partial}{\partial x} + jk_x & 1 & 0 \\ 0 & \frac{\partial}{\partial y} + jk_y & \frac{\partial}{\partial x} + jk_x \end{bmatrix}}_{\mathbf{L}_\varepsilon} \begin{bmatrix} \tilde{w}_0 \\ \tilde{\theta}_x \\ \tilde{\theta}_y \end{bmatrix} e^{j(k_x x + k_y y - \omega t)} \quad (5.A.11)$$

The material matrices are modified for the piezoelectric plate as :

$$\mathbf{C} = \begin{bmatrix} c_{11}^* & c_{12}^* & 0 & 0 & 0 \\ c_{12}^* & c_{22}^* & 0 & 0 & 0 \\ 0 & 0 & c_{44}^* & 0 & 0 \\ 0 & 0 & 0 & c_{55}^* & 0 \\ 0 & 0 & 0 & 0 & c_{66}^* \end{bmatrix}, \mathbf{e}^T = \begin{bmatrix} 0 & 0 & e_{31}^* \\ 0 & 0 & e_{32}^* \\ 0 & e_{24}^* & 0 \\ e_{15}^* & 0 & 0 \\ 0 & 0 & 0 \end{bmatrix}, \boldsymbol{\kappa} = \begin{bmatrix} \kappa_{11}^* & 0 & 0 \\ 0 & \kappa_{22}^* & 0 \\ 0 & 0 & \kappa_{33}^* \end{bmatrix}, \quad (5.A.12)$$

where the coefficients related to those of 3D solid are [135]

$$\begin{aligned} c_{11}^* &= c_{11} - \frac{(c_{13})^2}{c_{33}}, \quad c_{12}^* = c_{12} - \frac{c_{13}c_{23}}{c_{33}}, \quad c_{22}^* = c_{22} - \frac{(c_{23})^2}{c_{33}} \\ e_{31}^* &= e_{31} - \frac{c_{13}e_{33}}{c_{33}}, \quad e_{32}^* = e_{32} - \frac{c_{23}e_{33}}{c_{33}}, \quad \text{and } \kappa_{33}^* = \kappa_{33} + \frac{(e_{33})^2}{c_{33}}. \end{aligned} \quad (5.A.13)$$

In finite element implementation, the mid-plane displacement and rotations are discretized as

$$\begin{bmatrix} \tilde{w}_0(x, y) \\ \tilde{\theta}_x(x, y) \\ \tilde{\theta}_y(x, y) \end{bmatrix} = \sum_{i=1}^n \begin{bmatrix} \tilde{w}_0^i \\ \tilde{\theta}_x^i \\ \tilde{\theta}_y^i \end{bmatrix} N^i(x, y) = \mathbf{N}\mathbf{U}^e, \quad (5.A.14)$$

where

$$\mathbf{N} = \begin{bmatrix} N_1 & 0 & 0 & \dots & N_n & 0 & 0 \\ 0 & N_1 & 0 & \dots & 0 & N_n & 0 \\ 0 & 0 & N_1 & \dots & 0 & 0 & N_n \end{bmatrix} \quad (5.A.15)$$

$$\mathbf{U}^e = \left[\tilde{w}_0^1 \quad \tilde{\theta}_x^1 \quad \tilde{\theta}_y^1 \quad \dots \quad \tilde{w}_0^n \quad \tilde{\theta}_x^n \quad \tilde{\theta}_y^n \right]^T$$

are the matrix of finite element shape functions and nodal values. By substituting (5.A.6-5.A.7) and (5.A.10-5.A.11) to the weak formulation (5.A.5), we obtain the general discrete

equations of motion for phononic substrate plates with piezoelectric patches bonded on it (Fig. 2).

$$\begin{bmatrix} \mathbf{M}_{uu} & \mathbf{0} \\ \mathbf{0} & \mathbf{0} \end{bmatrix} \begin{bmatrix} \ddot{\mathbf{U}} \\ \ddot{\mathbf{V}} \end{bmatrix} + \begin{bmatrix} \mathbf{K}_{uu} & -\mathbf{K}_{uv} \\ \mathbf{K}_{vu} & \mathbf{K}_{vv} \end{bmatrix} \begin{bmatrix} \mathbf{U} \\ \mathbf{V} \end{bmatrix} = \begin{bmatrix} \mathbf{f} \\ \mathbf{Q} \end{bmatrix} \quad (5.A.16)$$

where

$$\begin{aligned} \mathbf{V} &= [V^1 \quad \dots \quad V^p \quad \dots \quad V^{N_p}]^T, \quad \mathbf{Q} = [Q^1 \quad \dots \quad Q^p \quad \dots \quad Q^{N_p}]^T \\ \mathbf{K}_{uu} &= \int_x \int_y \mathbf{B}_u^T \left(\int_z \mathbf{Z}_\varepsilon^T \mathbf{C} \mathbf{Z}_\varepsilon dz \right) \mathbf{B}_u dx dy, \quad \mathbf{M}_{uu} = \int_x \int_y \mathbf{N}^T \left(\int_z \rho \mathbf{Z}_u^T \mathbf{Z}_u dz \right) \mathbf{N} dx dy \\ \mathbf{K}_{uv} &= \int_x \int_y \mathbf{B}_u^T \left(\int_z \mathbf{Z}_\varepsilon^T \mathbf{e}^T dz \right) \mathbf{B}_v dx dy, \quad \mathbf{K}_{vv} = \int_x \int_y \mathbf{B}_v^T \left(\int_z \boldsymbol{\kappa} dz \right) \mathbf{B}_v dx dy \\ \mathbf{B}_u &= \mathbf{L}_\varepsilon \mathbf{N}, \quad \text{and } \mathbf{B}_v = \frac{1}{h} \begin{bmatrix} 0 \\ 0 \\ -1 \end{bmatrix}. \end{aligned} \quad (5.A.17)$$

Under open-circuit condition, the reaction electric charge Q^p is zero in the piezoelectric patch, and if the displacement and voltage are time harmonic, $(\circ) = (\bar{\circ}) \exp(j\omega t)$, Bloch wave solutions of the phononic plate are obtained from the following eigenvalue problem:

$$\left(-\omega^2 \begin{bmatrix} \mathbf{M}_{uu} & \mathbf{0} \\ \mathbf{0} & \mathbf{0} \end{bmatrix} + \begin{bmatrix} \mathbf{K}_{uu} & -\mathbf{K}_{uv} \\ \mathbf{K}_{vu} & \mathbf{K}_{vv} \end{bmatrix} \right) \begin{bmatrix} \bar{\mathbf{U}} \\ \bar{\mathbf{V}} \end{bmatrix} = \begin{bmatrix} \mathbf{0} \\ \mathbf{0} \end{bmatrix}, \quad (5.A.18)$$

where the nodal displacements are enforced to be periodic over boundaries of the unit cell. For the sake of simplicity, we consider the shunt circuit to have a negative capacitance only; various studies on the passive electrical networks can be found in Toftækær et al. [133], Berardengo et al. [136] and Gardonio and Casagrande [137]. If an electrode is connected to the external negative capacitance, the relation between the reaction electric charge $Q^{\tilde{p}}$ and the voltage is given as

$$\dot{Q}^{\tilde{p}} = -C_n \dot{V}^{\tilde{p}} \quad (5.A.19)$$

or

$$\bar{Q}^{\tilde{p}} = -C_n \bar{V}^{\tilde{p}} \quad (5.A.20)$$

if the voltage and the electric charge are considered harmonic in time. Therefore, the eigenvalue problem (5.A.18) is modified as

$$\left(-\omega^2 \begin{bmatrix} \mathbf{M}_{uu} & \mathbf{0} & \mathbf{0} \\ \mathbf{0} & \mathbf{0} & \mathbf{0} \\ \mathbf{0} & \mathbf{0} & \mathbf{0} \end{bmatrix} + \begin{bmatrix} \mathbf{K}_{uu} & -\mathbf{K}_{uv}^p & \mathbf{K}_{uv}^{\tilde{p}}/C_n \\ \mathbf{K}_{vu}^p & \mathbf{K}_{vv}^p & \mathbf{0} \\ \mathbf{K}_{vu}^{\tilde{p}} & \mathbf{0} & (-\mathbf{I} - \mathbf{K}_{vv}^{\tilde{p}}/C_n) \end{bmatrix} \right) \begin{bmatrix} \bar{\mathbf{U}} \\ \bar{\mathbf{V}}^p \\ \bar{\mathbf{Q}}^{\tilde{p}} \end{bmatrix} = \begin{bmatrix} \mathbf{0} \\ \mathbf{0} \\ \mathbf{0} \end{bmatrix}, \quad (5.A.21)$$

where \tilde{p} denotes the patches connected to the shunt circuit, p the patches with open circuit, C_n is the capacitance value, and \mathbf{I} is the identity matrix.

For transient simulation, we take time derivative of the second equation in (5.A.16)

$$\mathbf{K}_{vu}\dot{\mathbf{U}} + \mathbf{K}_{vv}\dot{\mathbf{V}} = \dot{\mathbf{Q}}, \quad (5.A.22)$$

and together with (5.A.19), the dynamic equations of the coupled electromechanical system connected to the external shunt circuits are as follows :

$$\begin{aligned} \begin{bmatrix} \mathbf{M}_{uu} & \mathbf{0} & \mathbf{0} \\ \mathbf{0} & \mathbf{0} & \mathbf{0} \\ \mathbf{0} & \mathbf{0} & \mathbf{0} \end{bmatrix} \begin{bmatrix} \ddot{\mathbf{U}} \\ \ddot{\mathbf{V}}^p \\ \ddot{\mathbf{V}}^{\tilde{p}} \end{bmatrix} + \begin{bmatrix} \mathbf{0} & \mathbf{0} & \mathbf{0} \\ \mathbf{0} & \mathbf{0} & \mathbf{0} \\ \mathbf{K}_{vu}^{\tilde{p}} & \mathbf{0} & \mathbf{K}_{vv}^{\tilde{p}} + C_n \mathbf{I} \end{bmatrix} \begin{bmatrix} \dot{\mathbf{U}} \\ \dot{\mathbf{V}}^p \\ \dot{\mathbf{V}}^{\tilde{p}} \end{bmatrix} \\ + \begin{bmatrix} \mathbf{K}_{uu} & -\mathbf{K}_{uv}^p & -\mathbf{K}_{uv}^{\tilde{p}} \\ \mathbf{K}_{vu}^p & \mathbf{K}_{vv}^p & \mathbf{0} \\ \mathbf{0} & \mathbf{0} & \mathbf{0} \end{bmatrix} \begin{bmatrix} \mathbf{U} \\ \mathbf{V}^p \\ \mathbf{V}^{\tilde{p}} \end{bmatrix} = \begin{bmatrix} \mathbf{f} \\ \mathbf{0} \\ \mathbf{0} \end{bmatrix}. \end{aligned} \quad (5.A.23)$$

In this work, the transient solutions are obtained by using the generalized- α time integration scheme. To avoid instability in transient analysis, we use a negative capacitance $C_n = -0.9 \times K_{vv}$ in the simulation.

The Poynting vectors, which represent the instantaneous power flow at a specific time, are defined as

$$P_i = -\sigma_{ij}\dot{u}_j. \quad (5.A.24)$$

For harmonic vibration systems, the time-averaged Poynting vectors are determined by integrating over $T = 2\pi/\omega$

$$\langle P_i \rangle = \frac{1}{T} \int_0^T -\text{Re}(\sigma_{ij}\dot{u}_j) dt = \frac{\omega}{2\pi} \int_0^T -\frac{1}{2} \text{Re}(j\omega\bar{\sigma}_{ij}\dot{u}_j^*) dt = -\frac{\omega}{2} \text{Im}(\bar{\sigma}_{ij}\dot{u}_j^*), \quad (5.A.25)$$

where (\star) denotes complex conjugate, and the stress components $\tilde{\sigma}_{ij}$ are calculated from displacements \tilde{u}_j , which are obtained from the eigenvalue problem (5.A.21).

Appendix 5.B Berry Curvature and Chern Number

The Berry curvature at the reciprocal wave vector $\mathbf{k} = (k_x, k_y)$ is numerically calculated by [125, 138]

$$B(\mathbf{k}) = -2 \text{Im} \left(\frac{\partial \mathbf{u}^*}{\partial k_x} \mathbf{M}_{uu} \frac{\partial \mathbf{u}}{\partial k_y} \right) \quad (5.B.1)$$

in which the derivative of eigenvectors is numerically computed by using first 30 eigenvectors [139].

As shown in Fig. 5.B.1, the Berry curvature has peaks at the high symmetry points K and K' . Following the $\mathbf{k} \cdot \mathbf{p}$ theory [16, 103], the Berry curvature is theoretically written as

$$\Omega(\mathbf{k}) = \frac{1}{2} m v_g^2 \left(|\mathbf{k} - \mathbf{k}_0|^2 + m^2 \right)^{-3/2} \quad (5.B.2)$$

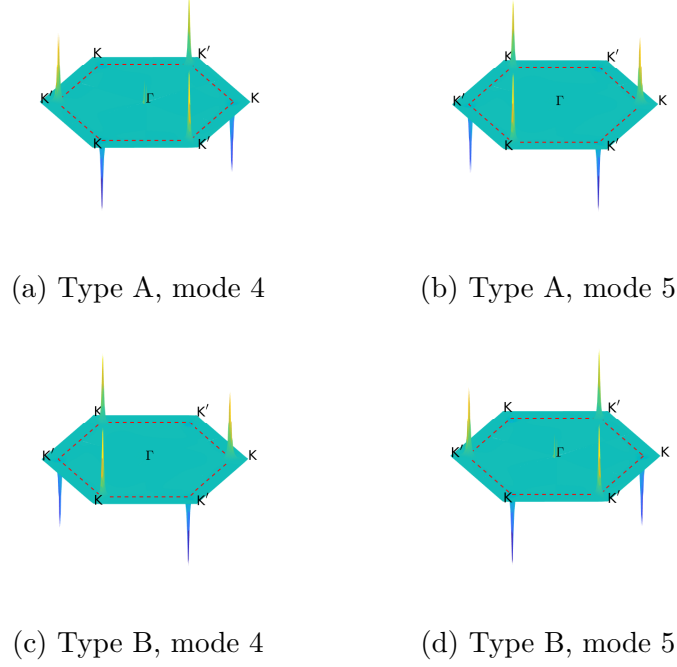


Figure 5.B.1: Berry curvature over the first Brillouin zone.

for a small perturbation of the wave vectors \mathbf{k} around the point \mathbf{k}_0 , i.e., K or K' in the reciprocal space, and the group velocity $v_g = |\partial\omega/\partial\mathbf{k}|$ is calculated at the Dirac point. The effective mass m has the magnitude equal to the frequency gap between the two considered modes 4 and 5. The Chern number is obtained by integrating the Berry curvature over a small area around the valley points K (or K')

$$C_v = \frac{1}{2\pi} \int \Omega(\mathbf{k}) d\mathbf{k} = \frac{1}{2} \text{sgn}(m). \quad (5.B.3)$$

Appendix 5.C Parameter Setting for The Genetic Algorithm

A population of 500×225 binary strings are randomly generated, in which each candidate is a string of binary digits with length of 225 and can form a square of binary digits 15×15 as shown in Fig. 1 in the main text. To generate well connected geometries, we proceed morphological image processing (MIP) before evaluating the objective functions and constraints. After function evaluation, the individual strings are ranked based on their fitness. A crossover rate of 0.6 and a mutation rate of 0.1 are adopted to improve the fitness of the individuals with each passing generation. When a new generation are produced from the crossover and mutation, each candidate is also modified by the MIP. The fittest individual which gives a function value below the tolerance, on morphing yields the optimal topology shown in Fig. 2a. We choose the best candidate with a maximized band gap (minimized J_2^{ZC}) as listed on the Pareto front in Fig. 5.C.1, while the first objective function J_1^{OC} is below the tolerance value.

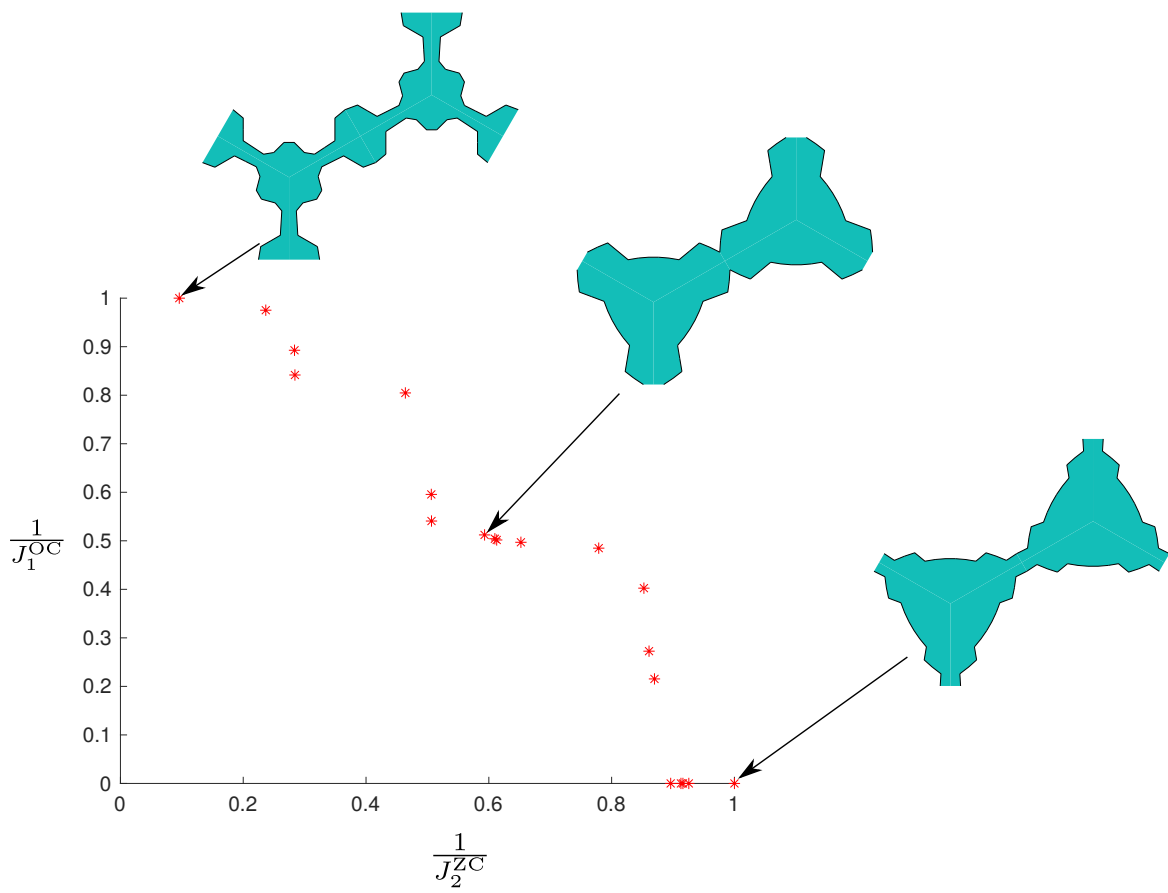


Figure 5.C.1: Pareto front of two normalized objective functions J_1^{OC} and J_2^{ZC} at the 89th generation.

Chapter 6

Discussion and Outlook

Topology optimization is a power tool for inversely designing structures, all the objectives are attained under a set of constraints during the optimization procedure. The subsequent step is to transform mathematical function, i.e., level sets, to counterparts like Computer-Aided Design (CAD) models and then physical fabricated prototypes. There are constraints in converting the level set objects to CAD models at an *ad hoc* manner, particularly, from the implicit functions to explicit geometric descriptions, including automatically fine-tuning surfaces and smoothing surfaces with sharp corners. Such corrections can help the analysis of optimal topologies to be more accurate with direct implementation of the finite element method and the CAD data is available as input for additive manufacturing.

Additive manufacturing process, for example 3D printing, allows manufacturing of complex geometries which are impossible to fabricate in traditional manufacturing methods. However, various factors such as characteristics of ingredient materials including material anisotropy, thermo-mechanical properties, and technical issues such as supports in printing or print directions can enormously affect the performance of the additively manufactured structures. Therefore, these factors should be considered during optimization.

The above mentioned existing problems aside, inverse design techniques presented in this thesis can provide solutions for designing novel metamaterials with intriguing physical phenomenon and can be adopted for novel functionalities in future. For instance, wave phenomenon appearing in subwavelength regimes such as acoustic and elastic cloaking effect [140], or double-negative elastic materials for elastic wave lenses in waveguide applications.

The presence of topologically protected edge modes enhances elastic energy efficiency in wave transport between two locations. Recently, second order topological phononic crystals, that offer corner modes in which elastic wave localizes at particular locations in the domain, are studied. This wave behaviour has potential in energy harvesting applications. Ideally, the elastic waves are trapped at desired locations and we can place piezoelectric patches at such locations to harvest the elastic energy.

Bibliography

- [1] A. Srivastava. Elastic metamaterials and dynamic homogenization: A review. *Int. J. Smart Nano Mater.*, 6(1):41–60, 2015. ISSN 1947542X.
- [2] A. Bensoussan, J.-L. Lions, and G. Papanicolaou. *Asymptotic Analysis for Periodic Structures*. Elsevier, 2011. ISBN 0080875262.
- [3] E. Sánchez-Palencia. Non-Homogeneous Media and Vibration Theory. *Lect. notes Phys.*, 127, 1980.
- [4] M. P. Bendsøe and O. Sigmund. *Topology Optimization*. Springer Science & Business Media, 2004. ISBN 3540429921.
- [5] J. A. Sethian. *Level Set Methods and Fast Marching Methods: Evolving Interfaces in Computational Geometry, Fluid Mechanics, Computer Vision, and Materials Science*. Cambridge Monographs on Applied and Computational Mathematics. Cambridge University Press, 1999. ISBN 9780521645577.
- [6] S. Osher and R. Fedkiw. *Level Set Methods and Dynamic Implicit Surfaces*, volume 153. Springer, 2003. ISBN 978-1-4684-9251-4.
- [7] G. Allaire, F. Jouve, and A. M. Toader. A level-set method for shape optimization. *Comptes Rendus Math.*, 334(12):1125–1130, 2002. ISSN 1631073X.
- [8] R. Lakes. Advances in negative poisson’s ratio materials. *Adv. Mater.*, 5(4):293–296, 1993. ISSN 09359648.
- [9] K. E. Evans and A. Alderson. Auxetic materials: Functional materials and structures from lateral thinking!. *Adv. Mater.*, 12(9):617–628, 2000. ISSN 09359648.
- [10] W. A. Smith. Optimizing electromechanical coupling in piezocomposites using polymers with negative Poisson’s ratio. In *IEEE 1991 Ultrason. Symp.*, pages 661–666, dec 1991.
- [11] M. Z. Hasan and C. L. Kane. Colloquium: Topological insulators. *Rev. Mod. Phys.*, 82(4):3045–3067, 2010. ISSN 00346861.
- [12] L. Müchler, B. Yan, F. Casper, S. Chadov, and C. Felser. *Topological Insulators*, volume 182. 2013. ISBN 9780444633149.
- [13] X. L. Qi and S. C. Zhang. Topological insulators and superconductors. *Rev. Mod. Phys.*, 83(4):1057, 2011. ISSN 00346861.

- [14] R. Süssstrunk and S. D. Huber. Classification of topological phonons in linear mechanical metamaterials. *Proc. Natl. Acad. Sci. U. S. A.*, 113(33):E4767–E4775, 2016. ISSN 10916490.
- [15] L. M. Nash, D. Kleckner, A. Read, V. Vitelli, A. M. Turner, and W. T. M. Irvine. Topological mechanics of gyroscopic metamaterials. *Proc. Natl. Acad. Sci. U. S. A.*, 112(47):14495–14500, 2015. ISSN 10916490.
- [16] S. H. Mousavi, A. B. Khanikaev, and Z. Wang. Topologically protected elastic waves in phononic metamaterials. *Nat. Commun.*, 6:1–7, 2015. ISSN 20411723.
- [17] Y. M. Xie and G. P. Steven. A simple evolutionary procedure for structural optimization. *Comput. Struct.*, 49(5):885–896, 1993. ISSN 00457949.
- [18] Y. M. Xie and G. P. Steven. Basic Evolutionary Structural Optimization. In *Evol. Struct. Optim.*, pages 12–29. Springer London, London, 1997. ISBN 978-1-4471-1250-1.
- [19] M. P. Bendsøe and O. Sigmund. Material interpolation schemes in topology optimization. *Arch. Appl. Mech.*, 69(9-10):635–654, 1999. ISSN 09391533.
- [20] O. Sigmund. Materials with prescribed constitutive parameters: An inverse homogenization problem. *Int. J. Solids Struct.*, 31(17):2313–2329, 1994. ISSN 00207683.
- [21] U. D. Larsen, O. Sigmund, and S. Bouwstra. Design and fabrication of compliant micromechanisms and structures with negative Poisson’s ratio. *J. Microelectromechanical Syst.*, 6(2):99–106, 1997. ISSN 10577157.
- [22] G. Allaire, F. Jouve, and G. Michailidis. Thickness control in structural optimization via a level set method. *Struct. Multidiscip. Optim.*, 53(6):1349–1382, 2016. ISSN 16151488.
- [23] G. Allaire and G. Michailidis. Modal basis approaches in shape and topology optimization of frequency response problems. *Int. J. Numer. Methods Eng.*, 113(8):1258–1299, 2017. ISSN 1097-0207.
- [24] P. Vogiatzis, S. Chen, X. Wang, T. Li, and L. Wang. Topology optimization of multi-material negative Poisson’s ratio metamaterials using a reconciled level set method. *Comput. Des.*, 83:15–32, 2017. ISSN 0010-4485.
- [25] M. Y. Wang and X. Wang. “Color” level sets: a multi-phase method for structural topology optimization with multiple materials. *Comput. Methods Appl. Mech. Eng.*, 193(6–8):469–496, 2004. ISSN 0045-7825.
- [26] O. Amir, M. Stolpe, and O. Sigmund. Efficient Reanalysis Procedures in Structural Topology Optimization. *Dep. Math.*, PhD:155, 2011.
- [27] S. Wang, E. de Sturler, and G. H. Paulino. Large-scale topology optimization using preconditioned Krylov subspace methods with recycling. *Int. J. Numer. Methods Eng.*, 69(12):2441–2468, 2007. ISSN 00295981.
- [28] L. Xia and P. Breitkopf. A reduced multiscale model for nonlinear structural topology optimization. *Comput. Methods Appl. Mech. Eng.*, 280:117–134, 2014. ISSN 00457825.

- [29] J. A. Hernández, J. Oliver, A. E. Huespe, M. A. Caicedo, and J. C. Cante. High-performance model reduction techniques in computational multiscale homogenization. *Comput. Methods Appl. Mech. Eng.*, 276:149–189, 2014. ISSN 00457825.
- [30] C. Gogu. Improving the efficiency of large scale topology optimization through on-the-fly reduced order model construction. *Int. J. Numer. Methods Eng.*, 101(4):281–304, 2015. ISSN 1097-0207.
- [31] T. J. R. Hughes, J. A. Cottrell, and Y. Bazilevs. Isogeometric analysis: CAD, finite elements, NURBS, exact geometry and mesh refinement. *Comput. Methods Appl. Mech. Eng.*, 194(39–41):4135–4195, 2005. ISSN 0045-7825.
- [32] J. A. Cottrell, T. J. Hughes, and Y. Bazilevs. *Isogeometric Analysis: Toward Integration of CAD and FEA*. Wiley, 2009. ISBN 9780470748732.
- [33] Y. Wang and D. J. Benson. Isogeometric analysis for parameterized LSM-based structural topology optimization. *Comput. Mech.*, 57(1):19–35, 2016. ISSN 01787675.
- [34] G. Costa, M. Montemurro, and J. Pailhès. Minimum length scale control in a NURBS-based SIMP method. *Comput. Methods Appl. Mech. Eng.*, 2019. ISSN 00457825.
- [35] J. Gao, H. Xue, L. Gao, and Z. Luo. Topology optimization for auxetic metamaterials based on isogeometric analysis. *Comput. Methods Appl. Mech. Eng.*, 352:211–236, 2019. ISSN 00457825.
- [36] A. Manzoni, F. Salmoiraghi, and L. Heltai. Reduced Basis Isogeometric Methods (RB-IGA) for the real-time simulation of potential flows about parametrized NACA airfoils. *Comput. Methods Appl. Mech. Eng.*, 284:1147–1180, 2015. ISSN 00457825.
- [37] S. Zhu, L. Dedè, and A. Quarteroni. Isogeometric analysis and proper orthogonal decomposition for the acoustic wave equation. *ESAIM Math. Model. Numer. Anal.*, 51(4):1197–1221, 2017. ISSN 0764-583X.
- [38] A. Ammar, A. Huerta, F. Chinesta, E. Cueto, and A. Leygue. Parametric solutions involving geometry: A step towards efficient shape optimization. *Comput. Methods Appl. Mech. Eng.*, 268:178–193, 2013. ISSN 00457825.
- [39] L. Chamoin and H. P. Thai. Certified real-time shape optimization using isogeometric analysis, PGD model reduction, and a posteriori error estimation. *Int. J. Numer. Methods Eng.*, (February):151–176, 2019. ISSN 10970207.
- [40] J. D. Eshelby and R. E. Peierls. The determination of the elastic field of an ellipsoidal inclusion, and related problems. *Proc. R. Soc. London. Ser. A. Math. Phys. Sci.*, 241:376–396, 1957.
- [41] T. Mori and K. Tanaka. Average stress in matrix and average elastic energy of materials with misfitting inclusions. *Acta Metall.*, 21(5):571–574, may 1973. ISSN 00016160.
- [42] R. Hill. A self-consistent mechanics of composite materials. *J. Mech. Phys. Solids*, 13(4):213–222, 1965. ISSN 00225096.

- [43] J. Hohe and W. Becker. An energetic homogenisation procedure for the elastic properties of general cellular sandwich cores. *Compos. Part B Engineering*, 32(3):185–197, 2001. ISSN 13598368.
- [44] Q. S. Yang and W. Becker. A comparative investigation of different homogenization methods for prediction of the macroscopic properties of composites. *C. - Comput. Model. Eng. Sci.*, 6(4):319–332, 2004. ISSN 15261492.
- [45] E. Sanchez-Palencia. Homogenization in mechanics, A survey of solved and open problems. *Rend. del Semin. Mat.*, 44(1):1–46, 1986.
- [46] W. Zhang, G. Dai, F. Wang, S. Sun, and H. Bassir. Using strain energy-based prediction of effective elastic properties in topology optimization of material microstructures. *Acta Mech. Sin. Xuebao*, 23(1):77–89, 2007. ISSN 05677718.
- [47] J. Guedes and N. Kikuchi. Preprocessing and postprocessing for materials based on the homogenization method with adaptive finite element methods. *Comput. Methods Appl. Mech. Eng.*, 83(2):143–198, 1990. ISSN 0045-7825.
- [48] X. Zhuang, Q. Wang, and H. Zhu. A 3D computational homogenization model for porous material and parameters identification. *Comput. Mater. Sci.*, 96, Part B:536–548, 2015. ISSN 0927-0256.
- [49] F. Fantoni, A. Bacigalupo, and M. Paggi. Multi-field asymptotic homogenization of thermo-piezoelectric materials with periodic microstructure. *Int. J. Solids Struct.*, 120:31–56, 2017. ISSN 00207683.
- [50] B. Hassani and E. Hinton. *Homogenization and Structural Topology Optimization*. Springer Science & Business Media, 1999.
- [51] M. Y. Wang, X. Wang, and D. Guo. A level set method for structural topology optimization. *Comput. Methods Appl. Mech. Eng.*, 192(1–2):227–246, 2003. ISSN 0045-7825.
- [52] G. Allaire, F. Jouve, and A.-M. Toader. Structural optimization using sensitivity analysis and a level-set method. *J. Comput. Phys.*, 194(1):363–393, 2004. ISSN 0021-9991.
- [53] T. Belytschko, S. P. Xiao, and C. Parimi. Topology optimization with implicit functions and regularization. *Int. J. Numer. Methods Eng.*, 57(8):1177–1196, 2003. ISSN 00295981.
- [54] M. J. Borden, M. A. Scott, J. A. Evans, and T. J. R. Hughes. Isogeometric finite element data structures based on Bézier extraction of NURBS. *Int. J. Numer. Methods Eng.*, 87(1-5):1–47, 2008. ISSN 00295981.
- [55] O. C. Zienkiewicz and R. L. Taylor. *The Finite Element Method: The basis*, volume 1 of *Referex Engineering*. Butterworth-Heinemann, 2000. ISBN 0750650494.
- [56] G. H. Yoon. Structural topology optimization for frequency response problem using model reduction schemes. *Comput. Methods Appl. Mech. Eng.*, 199(25–28):1744–1763, 2010. ISSN 0045-7825.
- [57] A. Chatterjee. An introduction to the proper orthogonal decomposition. *Curr. Sci.*, 78:808–817, 2000.

- [58] K. K. Choi and N. H. Kim. *Structural Sensitivity Analysis and Optimization*. Mechanical Engineering Series. Springer New York, 2006. ISBN 9780387271699.
- [59] K. Svanberg. The method of moving asymptotes - a new method for structural optimization. *Int. J. Numer. Methods Eng.*, 24(2):359–373, feb 1987. ISSN 10970207.
- [60] H. Li, Y. Ma, W. Wen, W. Wu, H. Lei, and D. Fang. In Plane Mechanical Properties of Tetrachiral and Antitetrachiral Hybrid Metastructures. *J. Appl. Mech.*, 84(8), 2017. ISSN 0021-8936.
- [61] I. G. Masters and K. E. Evans. Models for the elastic deformation of honeycombs. *Compos. Struct.*, 35(4):403–422, 1996. ISSN 0263-8223.
- [62] L. Xia and P. Breitkopf. Design of materials using topology optimization and energy-based homogenization approach in Matlab. *Struct. Multidiscip. Optim.*, 52(6):1229–1241, 2015. ISSN 1615-1488.
- [63] K. Svanberg. MMA and GCMMA – two methods for nonlinear optimization. pages 1–15, 2007.
- [64] M. J. Haun, P. Moses, T. R. Gururaja, W. A. Schulze, and R. E. Newnham. Transversely Reinforced 1–3 and 1-3-0 Piezoelectric Composites. *Ferroelectrics*, 49(1):259–264, nov 1983. ISSN 15635112.
- [65] M. J. Haun and R. E. Newnham. An experimental and theoretical study of 1-3 and 1-3-0 piezoelectric PZT-polymer composites for hydrophone applications. *Ferroelectrics*, 68(1):123–139, jan 1986. ISSN 15635112.
- [66] W. A. Smith. Modeling 1–3 Composite Piezoelectrics: Hydrostatic Response. *IEEE Trans. Ultrason. Ferroelectr. Freq. Control*, 40(1):41–49, jan 1993. ISSN 08853010.
- [67] O. Sigmund, S. Torquato, and I. A. Aksay. On the design of 1-3 piezocomposites using topology optimization. *J. Mater. Res.*, 13(4):1038–1048, apr 1998. ISSN 08842914.
- [68] L. V. Gibiansky and S. Torquato. Optimal design of 1-3 composite piezoelectrics. *Struct. Optim.*, 13(1):23–28, feb 1997. ISSN 09344373.
- [69] E. C. N. Silva, J. S. O. Fonseca, and N. Kikuchi. Optimal design of periodic piezocomposites. *Comput. Methods Appl. Mech. Eng.*, 159(1):49–77, 1998. ISSN 0045-7825.
- [70] E. C. N. Silva, J. S. O. Fonseca, F. M. de Espinosa, A. T. Crumm, G. A. Brady, J. W. Halloran, N. Kikuchi, E. C. Nelli Silva, J. S. Ono Fonseca, F. M. de Espinosa, A. T. Crumm, G. A. Brady, J. W. Halloran, and N. Kikuchi. Design of piezocomposite materials and piezoelectric transducers using topology optimization-Part I. *Arch. Comput. Methods Eng.*, 6(2):117–182, 1999. ISSN 1886-1784.
- [71] O. Sigmund. On the design of compliant mechanisms using topology optimization. *Mech. Struct. Mach.*, 25(4):493–524, 1997. ISSN 08905452.
- [72] M. Avellaneda and P. J. Swart. Calculating the performance of 1–3 piezoelectric composites for hydrophone applications: An effective medium approach. *J. Acoust. Soc. Am.*, 103(3):1449–1467, 1998. ISSN 0001-4966.

- [73] W. P. Mason and H. Baerwald. Piezoelectric Crystals and Their Applications to Ultrasonics. *Phys. Today*, 4(5):23–24, may 1951. ISSN 0031-9228.
- [74] R. Lerch. Simulation of Piezoelectric Devices by Two- and Three-Dimensional Finite Elements. *IEEE Trans. Ultrason. Ferroelectr. Freq. Control*, 37(3):233–247, may 1990. ISSN 08853010.
- [75] R. McLaughlin. A study of the differential scheme for composite materials. *Int. J. Eng. Sci.*, 15(4):237–244, jan 1977. ISSN 00207225.
- [76] M. L. Dunn and M. Taya. Micromechanics predictions of the effective electroelastic moduli of piezoelectric composites. *Int. J. Solids Struct.*, 30(2):161–175, 1993. ISSN 00207683.
- [77] A. N. Norris, A. J. Callegari, and P. Sheng. A generalized differential effective medium theory. *J. Mech. Phys. Solids*, 33(6):525–543, jan 1985. ISSN 00225096.
- [78] H. Wendland. Piecewise polynomial, positive definite and compactly supported radial functions of minimal degree. *Adv. Comput. Math.*, 4(1):389–396, dec 1995. ISSN 10197168.
- [79] X.-L. Qi and S.-C. Zhang. The quantum spin Hall effect and topological insulators. *Phys. Today*, 63(1):33–38, 2010.
- [80] C. L. Kane and E. J. Mele. Quantum Spin hall effect in graphene. *Phys. Rev. Lett.*, 95(22):226801, 2005. ISSN 00319007.
- [81] J. E. Moore. The birth of topological insulators. *Nature*, 464(7286):194–198, 2010. ISSN 00280836.
- [82] P. Wang, L. Lu, and K. Bertoldi. Topological Phononic Crystals with One-Way Elastic Edge Waves. *Phys. Rev. Lett.*, 115(10):1–5, 2015. ISSN 10797114.
- [83] Z. G. Chen and Y. Wu. Tunable Topological Phononic Crystals. *Phys. Rev. Appl.*, 5(5):54021, 2016. ISSN 23317019.
- [84] B. A. Bernevig, T. L. Hughes, and S.-C. Zhang. Quantum spin Hall effect and topological phase transition in HgTe quantum wells. *Science (80-.)*, 314(5806):1757–1761, 2006. ISSN 0036-8075.
- [85] M. König, S. Wiedmann, C. Brüne, A. Roth, H. Buhmann, L. W. Molenkamp, X.-L. Qi, and S.-C. Zhang. Quantum spin Hall insulator state in HgTe quantum wells. *Science (80-.)*, 318(5851):766–770, 2007.
- [86] C. He, X. C. Sun, X. P. Liu, M. H. Lu, Y. F. Y. Chen, L. Feng, and Y. F. Y. Chen. Photonic topological insulator with broken time-reversal symmetry. *Proc. Natl. Acad. Sci. U. S. A.*, 113(18):4924–4928, 2016. ISSN 10916490.
- [87] R. Süsstrunk and S. D. Huber. Observation of phononic helical edge states in a mechanical topological insulator. *Science (80-.)*, 349(6243):47–50, jul 2015.
- [88] R. K. Pal, M. Schaeffer, and M. Ruzzene. Helical edge states and topological phase transitions in phononic systems using bi-layered lattices. *J. Appl. Phys.*, 119(8), 2016. ISSN 10897550.

- [89] Y. Deng and Y. Jing. Zone folding induced topological insulators in phononic crystals. In *IEEE Int. Ultrason. Symp. IUS*, pages 1–4. IEEE, 2017. ISBN 9781538633830.
- [90] C. Brendel, V. Peano, O. Painter, and F. Marquardt. Snowflake phononic topological insulator at the nanoscale. *Phys. Rev. B*, 97(2):20102, 2018. ISSN 24699969.
- [91] B. Z. Xia, T. T. Liu, G. L. Huang, H. Q. Dai, J. R. Jiao, X. G. Zang, D. J. Yu, S. J. Zheng, and J. Liu. Topological phononic insulator with robust pseudospin-dependent transport. *Phys. Rev. B*, 96(9):1–7, 2017. ISSN 24699969.
- [92] S. Y. Yu, C. He, Z. Wang, F. K. Liu, X. C. Sun, Z. Li, H. Z. Lu, M. H. Lu, X. P. Liu, and Y. F. Chen. Elastic pseudospin transport for integratable topological phononic circuits. *Nat. Commun.*, 9(1), 2018. ISSN 20411723.
- [93] S. S. Nanthakumar, X. Zhuang, H. S. Park, C. Nguyen, Y. Chen, and T. Rabczuk. Inverse design of quantum spin hall-based phononic topological insulators. *J. Mech. Phys. Solids*, 125:550–571, 2019. ISSN 00225096.
- [94] R. E. Christiansen, F. Wang, and O. Sigmund. Topological Insulators by Topology Optimization. *Phys. Rev. Lett.*, 122(23):234502, 2019. ISSN 10797114.
- [95] H. W. Dong, S. D. Zhao, R. Zhu, Y. S. Wang, L. Cheng, and C. Zhang. Customizing acoustic dirac cones and topological insulators in square lattices by topology optimization. *J. Sound Vib.*, 493:115687, 2021. ISSN 10958568.
- [96] Y. Lu and H. S. Park. Double Dirac cones and topologically nontrivial phonons for continuous square symmetric unit cells. *Phys. Rev. B*, 103(6):64308, 2021. ISSN 0031-899X.
- [97] M. V. Berry. Quantal phase factors accompanying adiabatic changes. *A Half-Century Phys. Asymptotics Other Divers.*, 392(1802):72–84, 2017. ISSN 0080-4630.
- [98] R. Resta. Manifestations of Berry’s phase in molecules and condensed matter. *J. Phys. Condens. Matter*, 12(9):R107, 2000. ISSN 09538984.
- [99] R. Chaunsali, C. W. Chen, and J. Yang. Subwavelength and directional control of flexural waves in zone-folding induced topological plates. *Phys. Rev. B*, 97(5), 2018. ISSN 24699969.
- [100] B. Andrei Bernevig and Taylor L. Hughes. *Topological Insulators and Superconductors*. Princeton University Press, 2003. ISBN 9780691151755.
- [101] S. D. Huber. Topological mechanics. *Nat. Phys.*, 12(7):621–623, 2016. ISSN 17452481.
- [102] S. Raghu and F. D. M. Haldane. Analogs of quantum-Hall-effect edge states in photonic crystals. *Phys. Rev. A - At. Mol. Opt. Phys.*, 78(3):1–21, 2008. ISSN 10502947.
- [103] J. Lu, C. Qiu, L. Ye, X. Fan, M. Ke, F. Zhang, and Z. Liu. Observation of topological valley transport of sound in sonic crystals. *Nat. Phys.*, 13(4):369–374, 2017. ISSN 17452481.
- [104] C. He, X. Ni, H. Ge, X. C. Sun, Y. B. F. Chen, M. H. Lu, X. P. Liu, and Y. B. F. Chen. Acoustic topological insulator and robust one-way sound transport. *Nat. Phys.*, 12(12):1124–1129, 2016. ISSN 17452481.

- [105] X. Ni, C. He, X. C. Sun, X. P. Liu, M. H. Lu, L. Feng, and Y. F. Chen. Topologically protected one-way edge mode in networks of acoustic resonators with circulating air flow. *New J. Phys.*, 17, 2015. ISSN 13672630.
- [106] Z. Zhang, Y. Tian, Y. Wang, S. Gao, Y. Cheng, X. Liu, and J. Christensen. Directional Acoustic Antennas Based on Valley-Hall Topological Insulators. *Adv. Mater.*, 30(36): 1–7, 2018. ISSN 15214095.
- [107] R. K. Pal, J. Vila, and M. Ruzzene. Topologically protected edge states in mechanical metamaterials. In *Adv. Appl. Mech.*, volume 52, pages 147–181. Elsevier, 2019.
- [108] Y. Guo, T. Dekorsy, and M. Hettich. Topological guiding of elastic waves in phononic metamaterials based on 2D pentamode structures. *Sci. Rep.*, 7(1):1–7, 2017. ISSN 20452322.
- [109] L. Yang, K. Yu, Y. Wu, R. Zhao, and S. Liu. Topological spin-Hall edge states of flexural wave in perforated metamaterial plates. *J. Phys. D. Appl. Phys.*, 51(32), 2018. ISSN 13616463.
- [110] J. Vila, R. K. Pal, and M. Ruzzene. Observation of topological valley modes in an elastic hexagonal lattice. *Phys. Rev. B*, 96(13):134307, 2017.
- [111] Y. Jin, Y. Pennec, B. Bonello, H. Honarvar, L. Dobrzynski, B. Djafari-Rouhani, and M. I. Hussein. Physics of surface vibrational resonances: Pillared phononic crystals, metamaterials, and metasurfaces. *Reports Prog. Phys.*, 84(8), 2021. ISSN 13616633.
- [112] L. He, Z. Wen, Y. Jin, D. Torrent, X. Zhuang, and T. Rabczuk. Inverse design of topological metaplates for flexural waves with machine learning. *Mater. Des.*, 199: 109390, 2021. ISSN 18734197.
- [113] Z. Du, H. Chen, and G. Huang. Optimal quantum valley Hall insulators by rationally engineering Berry curvature and band structure. *J. Mech. Phys. Solids*, 135:103784, 2020. ISSN 00225096.
- [114] T. W. Liu and F. Semperlotti. Tunable Acoustic Valley-Hall Edge States in Reconfigurable Phononic Elastic Waveguides. *Phys. Rev. Appl.*, 9(1):14001, 2018. ISSN 23317019.
- [115] B. H. Nguyen, X. Zhuang, H. S. Park, T. Rabczuk, X. Zhuang, T. Rabczuk, H. S. Park, and T. Rabczuk. Tunable topological bandgaps and frequencies in a pre-stressed soft phononic crystal. *J. Appl. Phys.*, 125(9):1–18, 2019. ISSN 10897550.
- [116] A. Darabi, M. Collet, and M. J. Leamy. Experimental realization of a reconfigurable electroacoustic topological insulator. *Proc. Natl. Acad. Sci. U. S. A.*, 117(28):16138–16142, 2020. ISSN 10916490.
- [117] P. Dorin and K. W. Wang. Broadband Frequency and Spatial On-Demand Tailoring of Topological Wave Propagation Harnessing Piezoelectric Metamaterials. *Front. Mater.*, 7:409, 2021. ISSN 2296-8016.
- [118] J. O. Vasseur, A.-C. Hladky-Hennion, B. Djafari-Rouhani, F. Duval, B. Dubus, Y. Pennec, and P. A. Deymier. Waveguiding in two-dimensional piezoelectric phononic crystal plates. *J. Appl. Phys.*, 101(11):114904, 2007. ISSN 0021-8979.

- [119] K. Mekrache, R. Sainidou, P. Rembert, N. Stefanou, and B. Morvan. Tunable multidispersive bands of inductive origin in piezoelectric phononic plates. *J. Appl. Phys.*, **130**(19):195106, 2021. ISSN 10897550.
- [120] Y. Jin, D. Torrent, and B. Djafari-Rouhani. Robustness of conventional and topologically protected edge states in phononic crystal plates. *Phys. Rev. B*, **98**(5):54307, 2018. ISSN 24699969.
- [121] X. Wu, Y. Jin, A. Khelif, X. Zhuang, T. Rabczuk, and B. Djafari-Rouhani. Topological surface wave metamaterials for robust vibration attenuation and energy harvesting. *Mech. Adv. Mater. Struct.*, pages 1–9, 2021. ISSN 15376532.
- [122] A. Darabi and M. J. Leamy. Reconfigurable topological insulator for elastic waves. *J. Acoust. Soc. Am.*, **146**(1):773–781, 2019. ISSN 0001-4966.
- [123] S. Hedayatrasa, K. Abhary, and M. Uddin. Numerical study and topology optimization of 1D periodic bimaterial phononic crystal plates for bandgaps of low order Lamb waves. *Ultrasonics*, **57**(C):104–124, 2015. ISSN 0041624X.
- [124] S. Hedayatrasa, K. Abhary, M. Uddin, and C. T. Ng. Optimum design of phononic crystal perforated plate structures for widest bandgap of fundamental guided wave modes and maximized in-plane stiffness. *J. Mech. Phys. Solids*, **89**:31–58, 2016. ISSN 00225096.
- [125] D. Xiao, W. Yao, and Q. Niu. Valley-contrasting physics in graphene: Magnetic moment and topological transport. *Phys. Rev. Lett.*, **99**(23):1–4, 2007. ISSN 00319007.
- [126] S. Y. Huo, J. J. Chen, H. B. Huang, and G. L. Huang. Simultaneous multi-band valley-protected topological edge states of shear vertical wave in two-dimensional phononic crystals with veins. *Sci. Rep.*, **7**(1):1–8, 2017. ISSN 20452322.
- [127] H. Zhu, T. W. Liu, and F. Semperlotti. Design and experimental observation of valley-Hall edge states in diatomic-graphene-like elastic waveguides. *Phys. Rev. B*, **97**(17):1–9, 2018. ISSN 24699969.
- [128] V. Laude, R. P. Moiseyenko, S. Benchabane, and N. F. Declercq. Bloch wave deafness and modal conversion at a phononic crystal boundary. *AIP Adv.*, **1**(4), 2011. ISSN 21583226.
- [129] P. Dorin and K.-W. Wang. Reconfigurable elastic quantum valley Hall edge states in a piezoelectric topological metamaterial. **1138117:47**, 2020. ISSN 1996756X.
- [130] O. Thomas, J.-F. Deü, and J. Ducarne. Vibrations of an elastic structure with shunted piezoelectric patches: efficient finite element formulation and electromechanical coupling coefficients. *Int. J. Numer. Methods Eng.*, **80**(2):235–268, 2009.
- [131] E. Reissner. The effect of transverse shear deformation on the bending of elastic plates. *J. Appl. Mech.*, **12**:69–77, 1945.
- [132] G. R. Liu and S. S. Quek. *Finite Element Method: A Practical Course*. Elsevier Science, 2003. ISBN 9780080472768.

- [133] J. F. Toftekær, A. Benjeddou, J. Høgsberg, and S. Krenk. Optimal piezoelectric resistive–inductive shunt damping of plates with residual mode correction. *J. Intell. Mater. Syst. Struct.*, 29(16):3346–3370, 2018. ISSN 15308138.
- [134] S. Y. Wang, S. T. Quek, and K. K. Ang. Vibration control of smart piezoelectric composite plates. *Smart Mater. Struct.*, 10(4):637–644, 2001. ISSN 09641726.
- [135] E. Balmes and A. Deraemaeker. Modeling structures with piezoelectric materials. Theory and SDT tutorial. *SDT Tutor.*, page 71, 2014.
- [136] M. Berardengo, O. Thomas, C. Giraud-Audine, and S. Manzoni. Improved resistive shunt by means of negative capacitance: New circuit, performances and multi-mode control. *Smart Mater. Struct.*, 25(7), 2016. ISSN 1361665X.
- [137] P. Gardonio and D. Casagrande. Shunted piezoelectric patch vibration absorber on two-dimensional thin structures: Tuning considerations. *J. Sound Vib.*, 395:26–47, 2017. ISSN 10958568.
- [138] R. K. Pal and M. Ruzzene. Edge waves in plates with resonators: An elastic analogue of the quantum valley Hall effect. *New J. Phys.*, 19(2), 2017. ISSN 13672630.
- [139] S. Adhikari and M. I. Friswell. Eigenderivative analysis of asymmetric non-conservative systems. *Int. J. Numer. Methods Eng.*, 51(6):709–733, 2001. ISSN 00295981.
- [140] A. N. Norris and A. L. Shuvalov. Elastic cloaking theory. *Wave Motion*, 48(6):525–538, 2011. ISSN 01652125.

Curriculum vitae

Chuong T. Nguyen

born July 28, 1986 in Ba Ria - Vung Tau, Viet Nam

Professional Experience and Education

- | | |
|-----------------|---|
| 09.2016-09.2022 | PhD student at Leibniz Universität Hannover,
Germany |
| 09.2018-03.2019 | Visiting researcher at LMT laboratory (Laboratoire
de Mécanique et Technologie) of ENS Paris-Saclay,
France |
| 09.2015-12.2015 | Visiting researcher at Institute of Mechanics and
Dynamics, University of Kassel, Germany |
| 09.2013-09.2015 | Master student at Vietnamese-German University,
Binh Duong, Viet Nam |
| 01.2012-09.2013 | Mechanical Design Engineer at Industrielle
Beteiligung, Saigon, Viet Nam |
| 09.2005-09.2010 | Bachelor at University of Technical Education,
Saigon, Viet Nam |